

Modeling and Testing of Static and Dynamic Behavior of MEMS
Deformable Microstructures with Multiple Electrodes

Yunqiang Li

A thesis
in
The Department
of
Mechanical and Industrial Engineering

Presented in Partial Fulfillment of the Requirements
for the Degree of Master of Applied Science (Mechanical Engineering) at
Concordia University
Montreal, Quebec, Canada

April, 2007

© Yunqiang Li, 2007



Library and
Archives Canada

Bibliothèque et
Archives Canada

Published Heritage
Branch

Direction du
Patrimoine de l'édition

395 Wellington Street
Ottawa ON K1A 0N4
Canada

395, rue Wellington
Ottawa ON K1A 0N4
Canada

Your file *Votre référence*
ISBN: 978-0-494-28940-2
Our file *Notre référence*
ISBN: 978-0-494-28940-2

NOTICE:

The author has granted a non-exclusive license allowing Library and Archives Canada to reproduce, publish, archive, preserve, conserve, communicate to the public by telecommunication or on the Internet, loan, distribute and sell theses worldwide, for commercial or non-commercial purposes, in microform, paper, electronic and/or any other formats.

The author retains copyright ownership and moral rights in this thesis. Neither the thesis nor substantial extracts from it may be printed or otherwise reproduced without the author's permission.

AVIS:

L'auteur a accordé une licence non exclusive permettant à la Bibliothèque et Archives Canada de reproduire, publier, archiver, sauvegarder, conserver, transmettre au public par télécommunication ou par l'Internet, prêter, distribuer et vendre des thèses partout dans le monde, à des fins commerciales ou autres, sur support microforme, papier, électronique et/ou autres formats.

L'auteur conserve la propriété du droit d'auteur et des droits moraux qui protègent cette thèse. Ni la thèse ni des extraits substantiels de celle-ci ne doivent être imprimés ou autrement reproduits sans son autorisation.

In compliance with the Canadian Privacy Act some supporting forms may have been removed from this thesis.

Conformément à la loi canadienne sur la protection de la vie privée, quelques formulaires secondaires ont été enlevés de cette thèse.

While these forms may be included in the document page count, their removal does not represent any loss of content from the thesis.

Bien que ces formulaires aient inclus dans la pagination, il n'y aura aucun contenu manquant.


Canada

ABSTRACT

MODELING AND TESTING OF STATIC AND DYNAMIC BEHAVIOR OF MEMS DEFORMABLE MICROSTRUCTURES WITH MULTIPLE ELECTRODES

Yunqiang Li

The nonlinear nature of electrostatic fields in micromachined structures, such as, cantilevers, bridges or plates, makes it difficult to achieve desired deflection shapes. The objective of this thesis is to develop an efficient analytical approach to predict the static deflection and dynamic behavior of microstructures subjected to electrostatic fields of multiple electrostatic actuators so that the microdevices can be effectively optimized and controlled in real time operation. The non-classical boundary conditions which result from various microfabrication processes are modeled with artificial springs. A classical energy method using boundary characteristic orthogonal polynomials was applied to formulate the equation of motion of the microsystems. Based on this method, influence functions were built and Least Squares Fitting method was used to optimize the applied voltage for each of electrostatic actuators so as to generate desired static deflections. The proposed method is simple and can be easily extended to complicated configurations which are suitable for adaptive optics applications.

Reduced Order Modeling (ROM) method in ANSYS was used to confirm the results obtained using the proposed method. Static and dynamic behaviors were predicted with finite element analysis (FEA) using ROM method. This study found that the static and dynamic behaviors predicted from the proposed method were highly consistent with those calculated from FEA in the region not close to pull-in condition. Softening effect of the electrostatic field, in terms of electrostatic stiffness, is demonstrated in the dynamic

simulation results. However, the proposed method is simpler and more efficient than FEA and can be conveniently used for any structures with non-classical boundary conditions. These features make the proposed method useful to effectively control and optimize the shape of a microstructure under multiple electrostatic actuators.

The proposed modeling method was further verified and validated with the fabricated devices using SOI (silicon on insulator) based Micragem technology. The devices fabricated include different designs of microbridges and microplates with multiple electrodes and support boundary conditions. The out of plane deflections were measured by interference fringe patterns localized near the test surface using a Mirau interferometry method. After the boundary conditions were characterized, the predicted deflections were presented and compared with the experimental results that were post processed by *Fringe ProcessorTM* using Fourier transform method. It is clearly demonstrated that Rayleigh Ritz method is simple and can predict the behavior of microdevices with multiple electrostatic actuators considering both non-classical boundary conditions and electromechanical coupling effect. Both the theoretical and experimental methods proposed in this thesis are very simple and easily implementable.

ACKNOWLEDGEMENT

I would like to take this chance to express my deep thanks and my appreciation to my thesis supervisors Dr. Rama B. Bhat and Dr. Muthukumaran Packirisamy, who supported me greatly and help me during my MS education.

It was Dr. Muthukumaran Packirisamy who provided an opportunity for me to enter MEMS research field. His innovative ideas and enthusiasm on his research field have deeply attracted me. He supported me in every possible way to guide me in the right research direction to advance my academic skills to a high level. At the same time, I would also like to thank my co-supervisor Dr. Rama B. Bhat. His kindness, patience and invaluable and enlightening advice on the physical phenomena, macro or micro, helped me use engineering way to solve the facing problems. Both professors are indeed the distinguished teachers and great people that I was blessed to know. I am greatly thankful to them for having offered me the best of education and being a constant source of inspiration.

I would like to thank the colleagues in “MEMS Group”, whom I was pleased to meet and know. Special thanks to Dr. Gino Rinadi and Dr. Jianliang You, who helped me understand many unclear points in static and dynamic behaviors of microstructures, taught me on how to do measurement in lab and gave lots of helpful ideas on solving problems.

Finally, I would like to express my sincere gratitude and deep appreciation to the endless support from my parents, my sisters and Jennie, for all their love and support.

TABLE OF CONTENTS

LIST OF FIGURES	x
LIST OF TABLES	xv
LIST OF ABBREVIATIONS.....	xvii
1 INTRODUCTION AND LITERATURE REVIEW	1
1.1 Introduction.....	1
1.2 Historical Background of MEMS	2
1.3 Prospect of MEMS.....	4
1.4 Optical MEMS	5
1.4.1 Micromirror Array in Optical MEMS: Case Studies.....	8
1.4.1.1 Optical Cross Connect (OXC).....	8
1.4.1.2 Digital Micromirror Devices (DMD).....	10
1.4.1.3 Segment Mirror and Continuous Surface Deformable Micromirrors...	11
1.4.2 Adaptive Optics	14
1.5 The Suitable Actuation Methods of MEMS Deformable Mirrors.....	16
1.6 MEMS Deformable Mirrors	19
1.6.1 Common Phenomena in Electrostatic Actuation.....	19
1.6.1.1 Highly Nonlinear Electrostatic and Mechanical Coupling	19
1.6.1.2 Pull-In Instability	20
1.6.1.3 Cross Talk in Electrostatic Actuators	21
1.7 Objectives of Thesis Research	22
1.7.1 Thesis Organization	23

2	MODELING OF DEFORMABLE MICROBRIDGE WITH MULTIPLE ELECTRODES	25
2.1	Introduction.....	25
2.2	Electrostatically Actuated Microbeams	28
2.2.1	Model of a Microbridge	28
2.2.2	Static Analysis	29
2.2.3	Static Influence Functions.....	32
2.2.4	Shape Optimization.....	36
2.2.5	Dynamic Analysis.....	39
2.3	Application to a Microbridge with Three Electrostatic Actuators.....	43
2.4	Summary	47
3	MODELING OF DEFORMABLE MICROPLATE WITH MULTIPLE ELECTRODES	49
3.1	Introduction.....	49
3.2	Electrostatically Actuated Microplate.....	52
3.2.1	Model of a Microplate	52
3.2.2	Static Analysis	54
3.2.3	Static Influence Functions and Shape Optimization.....	57
3.2.4	Dynamic Analysis.....	59
3.3	Validation of the Method	61
3.4	Application to a 3x3 -Electrode Microplate.....	64
3.5	Summary	70
4	Modeling Using Finite Element Method	71
4.1	Introduction.....	71

4.2	Modeling Used ANSYS.....	72
4.3	Simulating a Deformable Microbridge with Three Electrostatic Actuators	74
4.4	Simulating a Microplate with 2×2-Electrostatic Actuators	80
4.5	Summary.....	85
5	Design Layout, Microfabrication and Packaging	87
5.1	Introduction.....	87
5.2	PolyMUMPs	88
5.3	Micragem	93
5.4	Wirebonding	99
5.5	Summary.....	101
6	EXPERIMENTAL DESIGN AND VALIDATION.....	103
6.1	Introduction.....	103
6.2	Interference Phenomenon	105
6.2.1	Michelson Interferometer.....	106
6.2.2	Mirau Interference Objective.....	108
6.3	Measurement Techniques	109
6.3.1	Experimental Platform.....	109
6.3.2	Gap Measurement	112
6.3.3	Fourier-Transform Method	114
6.4	Testing Procedure and Validation.....	117
6.4.1	Case 1: Voltage Applied only at the Central Electrode.....	124
6.4.2	Case 2: Same Voltage Applied on Two-Side Electrostatic Actuators....	128
6.4.3	Case 3: Same Voltage Applied at all Three Electrostatic Actuators	131

6.5	Summary.....	135
7	CONCLUSIONS AND RECOMMENDS FOR FUTURE WORK.....	137
7.1	Conclusions.....	137
7.2	Recommendation for Future Work.....	140
	REFERENCE.....	142

LIST OF FIGURES

Fig. 1. 1. Optical MEMS Finding Greater Opportunities in Non-Telecom Products (adapted from In-Stat research, 2003)	6
Fig. 1. 2. (a) Schematic of a free-space MEMS optical switch (b) A MEMS 8×8 OXC micromirror array (adapted from Lin L Y et al., 1999)	8
Fig. 1. 3. (a) Schematic of a 3D OXC (b) Fujitsu Optical Switch Fabric (adapted from www.fujitsu.com).....	9
Fig. 1. 4. Two axis beam steering micromirror array (adapted from Nielson D T et al., 2000)	10
Fig. 1. 5. Schematic of DMD mirrors (a) Two DMD pixels in opposite tilting states;	11
Fig. 1. 6. (a) AFIT segmented multichannel mirror; (b) Delft University continuous mirror (adapted from Miller L M et al., 1993).....	12
Fig. 1. 7. Cross sectional view of deformable mirror architecture of Stanford (adapted from Mansell J D et al., 2000)	13
Fig. 1. 8. Operation of the three-layer deformable mirror of Stanford (adapted from Mansell J D et al., 2002)	13
Fig. 1. 9. Wavefront distortion corrected by deformable mirror (adapted from Tyson R K, 1998)	14
Fig. 1. 10. A simple adaptive-optical imaging system (adapted from Tyson R K, 1998)	15
Fig. 1. 11. Static stability characteristics (adapted from ANSYS Help).....	21
Fig. 2. 1. The schematic of a microbridge	28
Fig. 2. 2. The scheme of a three-electrode microbridge under the electrostatic force.....	32
Fig. 2. 3. Influence functions of the microbridge with three electrostatic actuators.....	33
Fig. 2. 4. Static deflection of three node points when voltage applied only at the central actuator ($V_1=V_3=0, V_2 \neq 0$).....	33
Fig. 2. 5. The influence function having linear relationship between nodal displacement and square of applied voltage on the central actuator ($V_1=V_3=0, V_2 \neq 0$).....	34

Fig. 2. 6. The deflection can be represented by combination of the influence functions .	35
Fig. 2. 7. Deflection estimated with influence function.....	36
Fig. 2. 8. Comparison between the desired deflection and optimized shape.....	43
Fig. 2. 9. Three sets of fixed grid points used as input to optimize the required voltages	44
Fig. 2. 10. Two sets of random points used as input to optimize required voltages.....	44
Fig. 2. 11. The first three mode shapes of the microbridge with different rotational stiffness on left hand side boundary at $V_1=V_2=V_3=0$	46
Fig. 2. 12. The variation of fundamental frequency against the bias voltages	46
Fig. 3. 1. The microplate supported by artificial springs on edges with multiple electrodes underneath.....	53
Fig. 3. 2. 3D Geometry of microplate and configuration of bottom electrodes.....	64
Fig. 3. 3. The static deflection of the microplate at $V_3=V_7=100$ V	65
Fig. 3. 4. The static deflection of the microplate at $V_1=V_3=V_9=100$ V	66
Fig. 3. 5. The static deflection of the microplate at $V_1=100$ V, $V_5=50$ V, $V_7=100$ V	66
Fig. 3. 6. Comparison of the desired deflection and the optimized deflection: (a) The mesh of the desired deflection at nodal points; (b) The deflection generated with the optimized voltages	67
Fig. 4. 1. (a) Flow of Co-Simulation; (b) ROM144 element in ANSYS (adapted from ANSYS Help)	72
Fig. 4. 2. 3D solid model of the microbridge with three electrostatic actuators.....	74
Fig. 4. 3. The static deflection of the microbridge ($V_1=300$ v, $V_2=50$ v, $V_3=150$ v).....	75
Fig. 4. 4. Comparison of node deflections when voltage was only applied at electrode 1	76
Fig. 4. 5. Comparison of node deflections when voltage was only applied at electrode 2	77
Fig. 4. 6. Comparison of deflection shapes under different applied voltages.....	77

Fig. 4. 7. Shift of the resonant frequency of mode 1 under different applied voltages at the central electrostatic actuator	79
Fig. 4. 8. Shift of the resonant frequency of mode 2 under different applied voltages at the central electrostatic actuator	79
Fig. 4. 9. 3D solid model of the microplate with 2x2 electrostatic actuators arrays.....	80
Fig. 4. 10. Electrostatic forces equilibrate with elastic forces of the microplate.....	81
Fig. 4. 11. The static deflection of the microplate ($V_1=400$ V, $V_2=150$ V, $V_3=50$ V, $V_4=200$ V)	82
Fig. 4. 12. Comparison of deflection shapes at different sections along x and y, ($V_1=0$, $V_2=150$ V, $V_3=50$ V, $V_4=200$ V)	83
Fig. 4. 13. Shift of the resonant frequency of mode 1 under different applied voltages at electrostatic actuator 1	85
Fig. 4. 14. Shift of the resonant frequency of mode 2 under different applied voltages at electrostatic actuator 1	85
Fig. 5. 1. Cross-section view of 7-layer of PolyMUMPs process (adapted from MUMPs Process, 2003)	88
Fig. 5. 2. Layout of the PolyMUMPs design	90
Fig. 5. 3. SEM picture of microbridge array.....	92
Fig. 5. 4. The boundary conditions and gap of microbridges fabricated through PolyMUMPs technology.....	93
Fig. 5. 5. Top view of the microplate with 9 electrodes fabricated through PolyMUMPs technology.....	93
Fig. 5. 6. Scheme of Micragem process (adapted from CMC/SCM, 2005)	94
Fig. 5. 7. Layout of Micragem design with microbridges and microplates	95
Fig. 5. 8. Close-up SEM view of the SOI microbridges and microplates designed on Micragem chip	96
Fig. 5. 9. SEM pictures of anchor, bottom electrodes, gap of electrostatic actuators and cutouts of Micragem structures.....	98

Fig. 5. 10. (a) WESTBONG 7400E manual wirebonding machine, (b) PolyMUMPs and Micragem loose dices	99
Fig. 5. 11. (a) Micragem and (b) PolyMUMPs chips after wirebonding.....	99
Fig. 6. 1. Interference fringe formation (adapted from <i>Nikon's MicroscopyU</i>)	105
Fig. 6. 2. Principle of the Michelson interferometer (adapted from Tolansky S, 1996). 106	
Fig. 6. 3. Mirau interference objective (adapted from <i>Nikon's MicroscopyU</i>).....	108
Fig. 6. 4. Experimental set up for measuring the out of plane deflection.....	111
Fig. 6. 5. Schematic of the proposed interferometric system.....	111
Fig. 6. 6. Fixture of the Micragem chip in measurement.....	112
Fig. 6. 7. (a) Micragem chips installation and (b) one result of gap measurement.....	113
Fig. 6. 8. Microruler used for the calibration the measurement results	113
Fig. 6. 9. The microbridge structure used in testing and its 3D model.....	118
Fig. 6. 10. The fringe patterns of the microbridge for different applied voltages only on central electrode	119
Fig. 6. 11. 2D and 3D FFT spectrum when $V_2=260$ V, $V_1=V_3=0$	120
Fig. 6. 12. 2D and 3D wrapped phase map.....	121
Fig. 6. 13. 2D and 3D unwrapped phase map.....	121
Fig. 6. 14. Equivalent structure of the microbridge used for experiment	122
Fig. 6. 15. Maximum deflections vs. Kr^* in the case voltage only applied at central electrode.....	123
Fig. 6. 16. Discrepancies between the experimental and theoretical maximum static deflection when voltage is only applied at central electrode	124
Fig. 6. 17. The comparison of prediction and experimental results, for different voltages applied only at the central electrode	127

Fig. 6. 18. The static deflections of experimental results and prediction under different voltages applied only at the central electrode	127
Fig. 6. 19. The fringe patterns of the microbridge for different applied voltages on two side electrodes	128
Fig. 6. 20. The comparison of prediction and experimental results when different voltages applied at two side electrodes	130
Fig. 6. 21. The static deflections of experimental results and prediction under different voltages applied at two side electrodes	131
Fig. 6. 22. The fringe patterns of the microbridge for different applied voltages on three electrodes together	131
Fig. 6. 23. Comparison between the experimental and theoretical results when same voltage is applied at three bottom electrodes together	132
Fig. 6. 24. The comparison of prediction and experimental results, different voltages applied at three electrodes together	134
Fig. 6. 25. The static deflections of experimental results and prediction under different voltages applied at all electrodes	135

LIST OF TABLES

Table 1. 1. Evolution of MEMS (adapted from Helvajian H, 1999)	2
Table 1. 2. Comparison between actuation and sensing methods (adapted from Kovacs G, 1998)	17
Table 2. 1. Geometry constants for the microbridge model	31
Table 2. 2. The natural frequencies of the clamped-clamped microbridge under the zero applied voltage	42
Table 3. 1. Geometry and parameters of the microplate model	53
Table 3. 2. Boundary configurations for square microplate	62
Table 3. 3. Comparison eigenvalues for SSSS boundary condition	62
Table 3. 4. Comparison eigenvalues for CCCC boundary condition	63
Table 3. 5. Comparison eigenvalues for SFSF boundary condition	63
Table 3. 6. Comparison eigenvalues for CFCF boundary condition	63
Table 3. 7. Frequency parameters for CFFF square plate	64
Table 3. 8. Desired deflection at the nodal points of the microplate (m)	68
Table 3. 9. The optimized voltages for the electrodes	68
Table 3. 10. The error between desired and optimized deflection (%)	68
Table 3. 11. The natural frequencies of the structure for different boundary conditions at optimized voltage configuration	69
Table 4. 1. The parameters of microplate model used in simulation	75
Table 4. 2. Comparison between Rayleigh-Ritz and Ansys (ROM) results	80

Table 4. 3. The parameters of microplate model used in simulation.....	80
Table 4. 4. Comparison the discrepancy of between Rayleigh Ritz and ROM results.....	84
Table 5. 1. Definitions of microstructures on the PolyMUMPs chip	91
Table 5. 2. Definitions of microstructures on the Micragem chip	97
Table 5. 3. The parameters of WESTBOND 7400E bonding machine.....	101
Table 6. 1. Dimensions and material properties of test microbridge.....	118
Table 6. 2. Comparison of the maximum deflection between prediction and experiments when voltage is applied only at central electrode	124
Table 6. 3. Comparison of the maximum deflection between prediction and experiments when same voltage is applied only at two side electrodes.....	128
Table 6. 4. Comparison of the maximum deflection between prediction and experiments when same voltage is applied at three electrodes at the same time	132

LIST OF ABBREVIATIONS

<i>A</i>	Arbitrary coefficients
AFIT	Air Force Institute of Technology
AO	Adaptive optics
BEM	Boundary element method
<i>C</i>	Influence function of microstructures
CCCC	Four edges clamped
CFCF	Two parallel edges clamped and two sides free
CFFF	One end clamped cantilever plate
<i>D</i>	Flexural rigidity of the microplate
DM	Deformable mirror
DMD	Digital micromirror devices
<i>E</i>	Young's modulus of single crystal silicon
<i>ER</i>	Residual error
FT	Fourier transforms
<i>I</i>	moment of inertia of the microbridge
IC	Integrated circuit
K_t	Translational spring stiffness for microbridge
K_T	Translational spring stiffness for microplate
K_r	Rotational spring stiffness for microbridge
K_R	Rotational spring stiffness for microplate
K_e	Electrostatic stiffness for microbridge
K_E	Electrostatic stiffness for microplate

L	Length of the microbridge
LPCVD	Low pressure chemical vapor deposition
M	Number of discrete nodal points
MMDM	Micromachined membrane deformable mirrors
MOEMS	Micro-opto-electro-mechanical systems
MST	Micro-system technology
MUMPs	Multi user MEMS process
N	Total number of electrostatic actuators
OXC	Optical cross connect
PGA	Ceramic pin grid array
PSG	Phospho silicate glass
PZT	Piezoelectric transducer
R	Rayleigh quotient
RIE	Reactive ion etching
ROM	Reduced order modeling
SCSi	Single crystal silicon
SEM	Scanning electron microscope
SFSF	Two parallel edges simply supported and two sides free
SLM	Spatial light modulation
SM	Segment mirror
SSSS	Four edges are simply supported
T_{max}	Maximum kinetic energy of the microstructures
U_{max} , U_{MAX}	Maximum total strain energy of microstructures

U_p, U_P	Strain energy of microstructures due to bending
U_s, U_R, U_T	Potential energy of the boundary springs
U_e, U_E	Strain energy due to the electrostatic field
ULSI	Ultra-large-scale integration
V_n	Applied voltage of the n^{th} electrostatic actuator
V_k	Applied voltage on the k^{th} actuator
W	the flexural deflection
a	Dimension of the microplate in x direction
b	Dimension of the microplate in y direction
d_0, d	Initial gap spacing of electrostatic actuators
t	Thickness of the microstructures
w	Efficient width of the electrode
$\alpha = \frac{a}{b}$	Side ratio of the microplate
ϵ_r	Relative permittivity of the air
ϵ_0	Permittivity in a vacuum
ξ	x coordinates of the microplate
η	y coordinates of the microplate
λ	Eigenvalue
ρ	Mass density of microstructures
$\phi(x)$	Boundary characteristic orthogonal polynomials
$\psi(x)$	Desired shape of the microstructures
ω	Natural frequency

CHAPTER 1

1 INTRODUCTION AND LITERATURE REVIEW

1.1 Introduction

Micro-Electro-Mechanical Systems (MEMS) are made by integrating mechanical elements, sensors, actuators and electronics on a common silicon substrate through microfabrication and micromachining technology. This technology is also called Micro System Technology (MST). The micromechanical components are fabricated using compatible micromachining processes that selectively etch away parts of the silicon wafer or add new structural layers to form the desired structures, such as beams, gears, diaphragms, and springs, while, the electronics components are fabricated using integrated circuit (IC) process sequences.

The integrated technology of MEMS enables the development of smart products, augmenting the computational ability of microelectronics with the perception and adjustable capabilities of microactuators, which greatly help broaden the scope of possible designs and applications of MEMS. Nowadays, the integrated Microsystems can combine optical, mechanical, electronic, thermal, magnetic, fluidic functions on a single small chip. For example, the concept of Lab-on-Chip is unique for the field of biochemistry, RF-MEMS benefited high frequency circuits in communications, and continuous deformable mirror (DM) made adaptive optics (AO) feasible for ophthalmic applications. Ultimately, miniaturization of mechanical systems promises unique opportunities for new directions in the progress of science and technology.

This chapter starts with an overview of MEMS technology, which covers the past and the present trends of MEMS technology and applications. The main emphasis will be applied on the applications of MEMS in optics, especially the new applications of deformable mirrors in adaptive optics.

1.2 Historical Background of MEMS

Table 1. 1. Evolution of MEMS (adapted from Helvajian H, 1999)

Silicon anisotropic etching	pre-1950
Piezoresistive effect in silicon	1953
Semiconductor strain gauges	1957
Silicon pressure sensors	post-1960
Solid state transducers	post-1970
Microactuators	post-1980
Mechanisms and motors	1987–89
Microelectromechanical systems	
Microsystems	post-1988
Micromachines	

The transistor [Shockley W et al., 1948, Bardeen J and Brattain W H, 1948] was invented at Bell Telephone Laboratories on 23 December 1947. This invention initiated a fast-paced microelectronic technology. The IC concept was conceived by several groups including RCA's Monolithic Circuit Technique for hybrid circuits (1955). The first IC was built by Jack Kilby of Texas Instruments in 1958. The complexity of ICs has doubled every 2 to 3 years since 1970 [Helvajian H, 1999]. The minimum dimension of manufactured devices and ICs has decreased from 20 μm to submicron and nano levels today. Currently, ultra-large-scale-integration (ULSI) enables the fabrication of more

than 10 million transistors and capacitors on a typical chip. Low-cost, high-performance electronic systems are now available to the public influencing the quality of life in every possible way. IC technology has provided high-speed, miniaturized and low-cost signal-processing capabilities, while, the conventional sensors and actuators are far behind in performance, size and cost.

Although research in MEMS dates from the 1950's, it is not until the mid-1990's that MEMS appeared in commercial products and applications as seen from Table 1. 1. A significant effort was given into developing silicon processing and characterization tools. The attention was first focused on microsensor development. Silicon microsensors initially addressed the measurement of physical variables, such as strain gauges and accelerometers. The most successful microsensor is the silicon based pressure sensor by Dr. Kulite, Kulite Semiconductor Products, Inc. in 1961. Its history can be representative of the evolution of microsensors. Although the past decade showed a wide variety of remarkable devices, which, however, did not necessarily find practical applications. Some of the successful commercial MEMS devices include: pressure sensors for automotive and medical applications [Chatzandroulis S et al., 2006], accelerometers used in automotive airbags [Hansen S I, 1999], thermal ("bubble") ink jet printer heads [Kamisuki S et al., 2000], MEMS mirror arrays for color projection displays [Douglass M R, 2003; Kim S et al., 2004] and micropositioners in data storage systems [Wu M C, 1995].

Among them, accelerometers and ink jet heads are the dominant contributors. Nonetheless, the inherent multidisciplinary capabilities of silicon, IC and MEMS

technology have shown significant promise in a broad range of areas, which include integrated microsensors, microactuators, microinstruments, micro-optics and microfluidics. The great potential for MEMS is bound to be exploited in new potential applications.

1.3 Prospect of MEMS

One of the main driving forces for the development of MEMS devices came from the excellent mechanical properties of silicon and advances in the IC process technology. Hence MEMS products were initially fabricated from silicon using production methods employed by IC industry. During the last 15 years, silicon microsensor technology has matured significantly and a variety of sensors have been developed for measuring position, velocity, acceleration, pressure, force, torque, flow, magnetic field, temperature, gas composition, humidity, pH, solution/body fluid ionic concentration, and biological gas/liquid/molecular concentrations. Some of these MEMS sensors have been commercialized successfully.

Micromechanical devices and systems are inherently smaller, lighter, faster, and usually more precise than their macroscopic counterparts. However, the development of micromechanical systems requires appropriate fabrication technologies that enable the following features in a general sense: (i) definition of small geometries (ii) precise dimensional control (iii) design flexibility (iv) interfacing with control electronics (v) repeatability, reliability and high yield (vi) low cost per device.

At the same time, new applications are emerging as the existing technology is applied to the miniaturization and integration of conventional devices. MEMS is an application driven technology and has emerged as an interdisciplinary field that involves many areas of science and engineering. On the other hand, the multidisciplinary nature of MEMS technology has resulted in synergies between previously unrelated fields, such as biology and microelectronics. Moreover, MEMS allow the manufacture of products that can not be made by other methods. It encompasses most aspects of micromachining based on photolithography for materials extending beyond single crystal silicon or polysilicon. The work which has been done in recent years in areas outside of traditional silicon-based MEMS is enormous. All of these outstanding advantages make MEMS more attractive than conventionally manufactured methods.

1.4 Optical MEMS

Recently, there has been a rapid progress in optical systems for telecommunications to meet the needs for increased bandwidth, for optical networks with terabit capacities per fiber link, and for local area networks. There are many applications which require precise features for optical alignment or precise movement of small optical parts to achieve final functionality. The accurate, low-loss, low-cost connecting approaches in MEMS are very suitable for different guided wave optical components, including fibers, lasers and waveguides. These new applications for MEMS in optics open up a new field called Micro-Opto-Electro-Mechanical Systems (MOEMS).

Many MOEMS components process miniature free-space optical beams and the performance scaling laws in such micro components are often different from those of

guided wave optical systems. The silicon along with other materials and technologies are used to create MEMS devices for many different applications. Here are a few MOEMS devices: Tunable lasers & filters [Zhou T and Robinson A M, 2002], Variable optical attenuators [Giles C R et al., 1999], Optical switches and crossconnects [Lin L Y et al., 1999; Neilson D T et al., 2000], Wavelength division multiplexers [Yang W et al., 1996] and Dispersion compensators [Ting-Kuang C et al., 1996].

As the new materials are being used in the IC industry, MEMS can potentially benefit from these developments. Examples are (i) silicon-on-insulator (SOI) technology, whereby low stress mirrors and other MEMS components are made with reproducible mechanical properties and excellent control of planarity, and (ii) low stress Si_3N_4 which has a high Young's modulus and has promising applications in packaging. At the same time, the advance in IC manufacturing technologies allows the fabrication of thousands of MEMS devices with increased reliability and reduced cost.

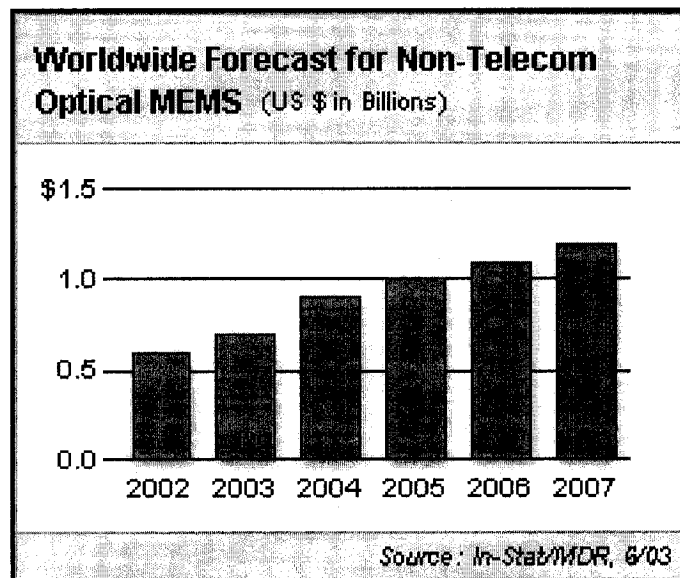


Fig. 1. 1. Optical MEMS Finding Greater Opportunities in Non-Telecom Products (adapted from In-Stat research, 2003)

High-tech market research firm, In-Stat/MDR reports that optical MEMS are extremely well suited to products that demand high-quality imaging and/or utilize lasers, and where their small form factor can open the door to new market opportunities [In-Stat research, 2003]. As a result, the sale of optical MEMS outside of telecom, are forecast to grow at 15.8% over the next 5 years, as shown at Fig. 1. 1. The same prediction can also be found in [CIR, 2003], which claims that most of the future growth of MOEMS will come from other application areas for light control and storage, sensing and in manufacturing technology.

They also found that the biggest application of optical MEMS was a variety of display subsystems, including those that are portable, integrated and wearable. Many other areas are also benefited from these devices. Much of the real movement of optical MEMS into markets beyond telecom occurred only very recently, including free-space micro-optical components and systems, displays and spatial light modulators, micro-optical sensors and actuators, microoptical biosensors, adaptive optics and aberration-control systems. While mirror arrays have made the biggest success to date, deformable mirrors, and micro lens arrays have been quietly advancing into the market.

Despite the fact that the next-generation imaging systems and optical networking both use MEMS mirrors, the architectures required for images are quite different from those used in telecom. In the following sections, the typical micromirror array that is used in optical MEMS will be introduced, especially, the characteristics of the continuously deformable mirror (DM) and its new applications, which just emerged in recent years.

1.4.1 Micromirror Array in Optical MEMS: Case Studies

Among many benefits of MEMS technology that were reviewed as core success factors, the ones that stand out are: (i) Arrayability, the ability to place tiny devices in large-scale arrays (ii) Nano positioning, precision control of position and alignment for microscale devices (iii) Reconfigurability, the ability to reconfigure the optical properties through localized micro actuation and/or deformation. Here, by reviewing a few selected optical MEMS devices, functional requirements of arrayability and importance of reconfigurability in image process are explained.

1.4.1.1 Optical Cross Connect (OXC)

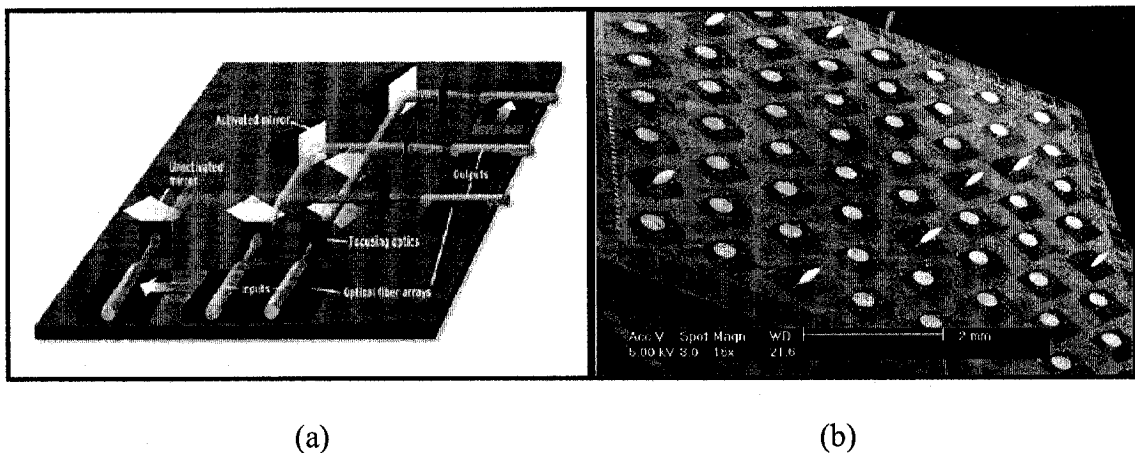
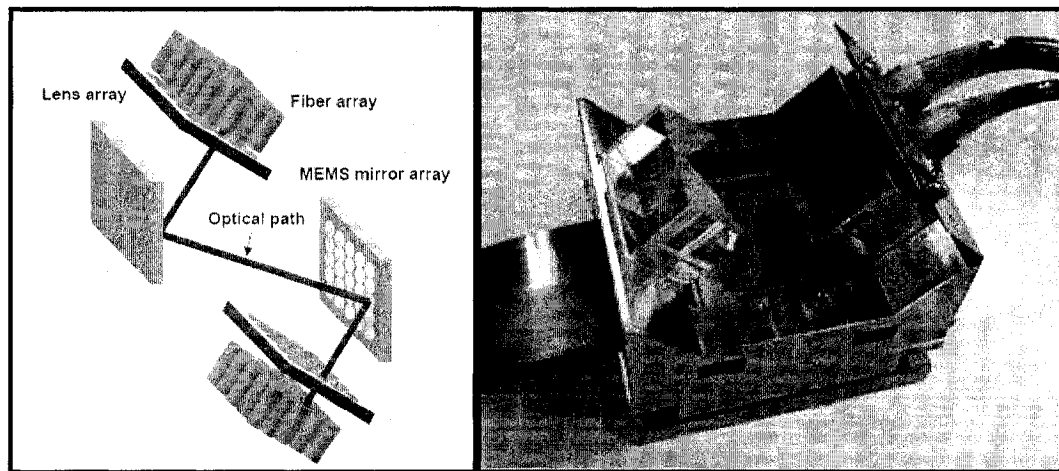


Fig. 1. 2. (a) Schematic of a free-space MEMS optical switch (b) A MEMS 8×8 OXC micromirror array (adapted from Lin L Y et al., 1999)

In practice, OXC fabrics fall into two broad categories based on the manner in which the free-space optical switching is performed. In one embodiment, all the light signals emanate from a linear array of fibers and the switching occurs in a single plane where each optical signal is switched to any of a second linear array of fibers. This approach requires N^2 MEMS mirror elements for a cross-connect with $N \times N$ ports. This approach

was first demonstrated at AT&T Labs [Lin L Y et al., 1999] and is shown in Fig. 1. 2. Due to practical optics considerations, these “2D” fabrics are limited in port count to 32x32[Walker J A, 2001].

The second category of OXC fabrics uses two matrices of gimbals-mounted MEMS mirrors with 2-axis control to provide beam switching in a 3D space between two 2D arrays of collimated fibers. The first demonstration of a MEMS device for this type of OXC was the Texas Instruments/Astarte Fiber Networks’ Beehive switch. Using the 3D approach, it is expected that OXC fabrics can scale in a single stage to 1000×1000 ports and above, although at present the largest demonstrated fabric is 256x256 ports. A scheme shows the switching functionality of a 3D fabric given in Fig. 1. 3(a). A corresponding commercial product manufactured by Fujitsu, Japan is shown in Fig. 1. 3(b). A photograph of a gimbals-mounted mirror intended for use in a 3D architecture is shown in Fig. 1. 4 [Neilson D T et al., 2000; Chu P B et al., 2004].



(a) (b)
Fig. 1. 3. (a) Schematic of a 3D OXC (b) Fujitsu Optical Switch Fabric (adapted from www.fujitsu.com)

It is easy to find that the micromirror arrays in OXC devices own arrayability and nano positioning functions. They are just responsible for translating the input signals to the required output ports.

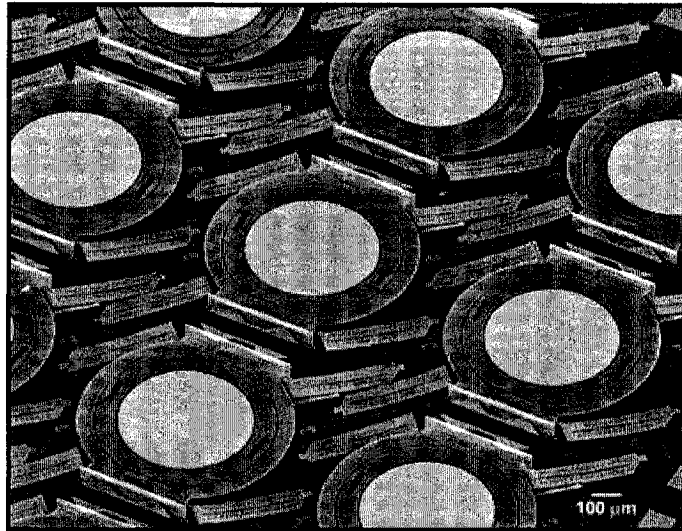


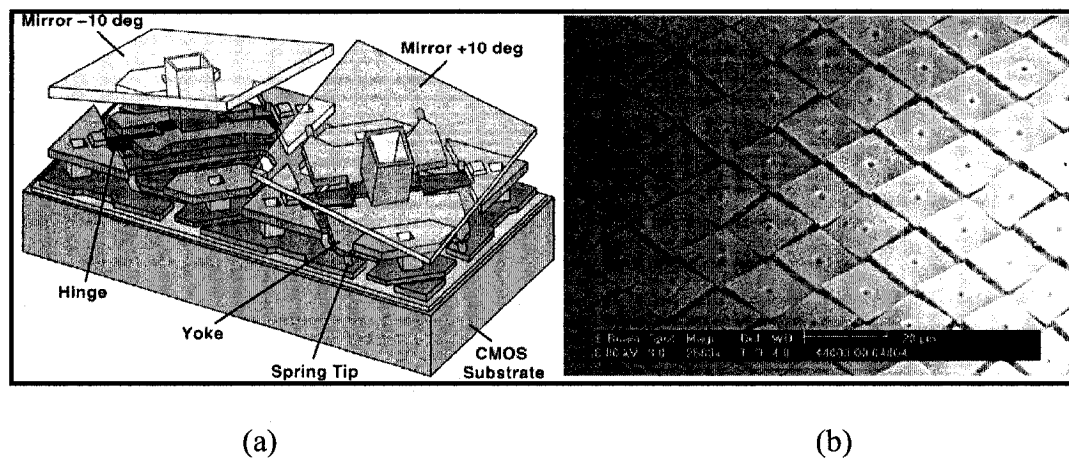
Fig. 1. 4. Two axis beam steering micromirror array (adapted from Nielson D T et al., 2000)

1.4.1.2 Digital Micromirror Devices (DMD)

The key idea of a DMD based display is to provide an array of bistable micromirrors to intercept the light path so that one of the mirror positions directs the light onto a screen, whereas the other position directs the light onto a block where it is absorbed. Therefore, each mirror modulates a different pixel. Color displays can be obtained by standard techniques such as a color wheel or three mirror arrays (for red-green-blue) combined with dichroic optics and projected onto the same screen [Hornbeck L J, 1995].

The application of DMD in image display systems is a MEMS success story because it saw tremendous progress in both performance and reliability [Douglass M R, 2003]. Since each micromirror on a DMD chip operates independently, each micromirror can

reflect light in one of two directions, either toward or away from the screen. That means each micromirror either illuminates a pixel or darkens a pixel. It uses the simplest way to understand the input signals, which is similar to a switch, “on, +10 degree” and “off, -10 degree” [Kim S et al., 2004], as shown in Fig. 1. 5(a). There is no doubt that DMD has become a great success in high-quality projected images, but its “on” and “off” behaviors, which just change the direction of light, are obviously not enough to meet the requirement of adaptive optical compensation.



(a) (b)
Fig. 1. 5. Schematic of DMD mirrors (a) Two DMD pixels in opposite tilting states;
(b) DMD mirror array (adapted from Kim S et al., 2004)

1.4.1.3 Segment Mirror and Continuous Surface Deformable Micromirrors

Deformable mirrors are especially used for spatial light modulation (SLM) and specifically for phase modulation required in adaptive optics systems. Segment mirror (SM) and continuous surface deformable mirrors (DM) are two main kinds of micromirrors used in wavefront compensating the aberrations and thereby improve the image resolution. These kinds of MEMS based deformable mirrors have been investigated by several research groups as an inexpensive and high-performance

alternative technology to the more conventional piezoelectric deformable mirrors. One of these, segmented micromirror devices based on silicon micromachining were pioneered by the Air Force Institute of Technology (AFIT) [Miller L M et al., 1993], as shown in Fig. 1. 6(a). The first commercially available MEMS-based deformable mirror was developed at Delft University. This device was comprised of a silicon nitride membrane suspended over an array of addressable electrodes [Vdovin G V and Sarro P M, 1995; Vdovin G et al., 1997], as shown in Fig. 1. 6(b). Subsequently, two-layer and three-layer MEMS-based deformable mirrors were designed and manufactured at Stanford University [Mansell J D et al., 2000 and 2002], as shown in Fig. 1. 7 and Fig. 1. 8. A similar design as shown in Fig. 1. 8 used two-level silicon surface micromachining approach that was employed by researchers at Boston University [Mali R K, 1999; Bifano T et al., 2002], to produce MEMS deformable mirrors. These devices were manufactured at a commercial MEMS foundry and were later commercialized.

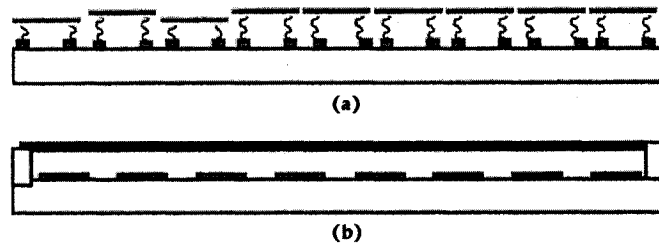


Fig. 1. 6. (a) AFIT segmented multichannel mirror; (b) Delft University continuous mirror (adapted from Miller L M et al., 1993)

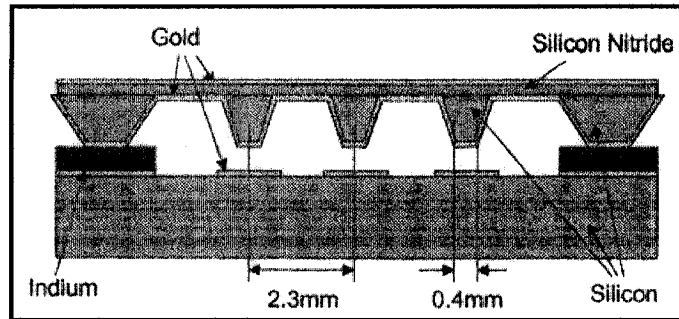


Fig. 1. 7. Cross sectional view of deformable mirror architecture of Stanford (adapted from Mansell J D et al., 2000)

For the wavefront correction, the SM can correct high spatial frequencies (many zones) but is limited in temporal frequency response [Tyson R K, 1998]. The piston/tip/ tilt corrections that can move very fast are restricted to only one mode. In addition, the discontinuities (gaps) between segments have an impact on overall performance. Energy is lost through the gaps, and since the gaps cause the mirror to act like a grating, the energy is diffracted from the central lobe also.

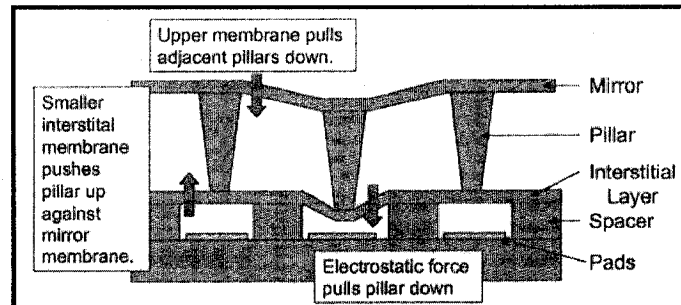


Fig. 1. 8. Operation of the three-layer deformable mirror of Stanford (adapted from Mansell J D et al., 2002)

A multiactuator continuously deformable mirror can correct many zones at high speed and is a candidate for an all purpose device. The three-layer architecture allows the

resonance frequency to be dominated by the stiffness of the interstitial layer and thus allow scaling of the deformable mirror to large apertures. Furthermore, the mechanical force pushing back on the mirror allows for a local deformation to occur, and thus allows the mirror to achieve higher spatial frequency response. Nevertheless, it is a big technical challenge to manufacture the three-layer DM design. Small error in the alignment of flip chip bonding will cause the distortion of top layer. Improper thickness of the interstitial layer will cause the excessive stiffness of the mirror surface.

1.4.2 Adaptive Optics

Adaptive Optics (AO) refers to optical systems which adapt to compensate for optical effects introduced by the medium between the object and its image. This concept was first proposed by [Babcock H W, 1953]. Adaptive optics systems have been traditionally used for atmospheric compensation in ground-based laser communications, in thermal compensation of some machining systems and in medical imaging through nonhomogeneous bodily fluids.

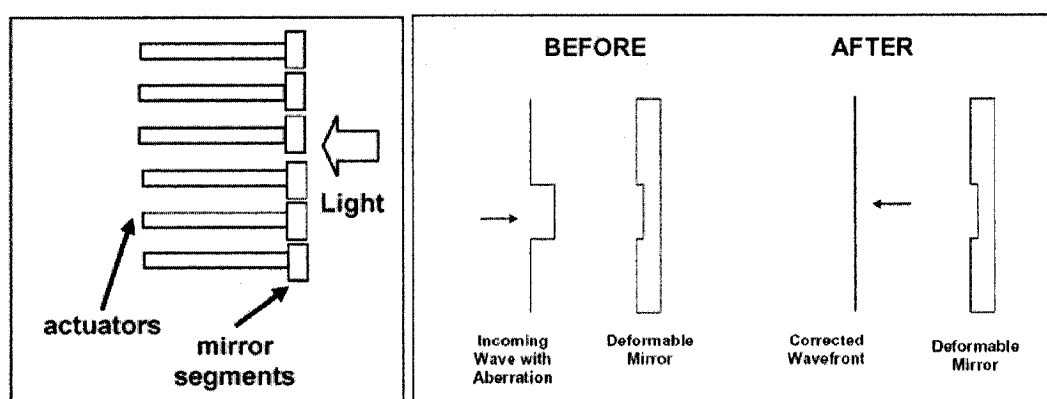


Fig. 1. 9. Wavefront distortion corrected by deformable mirror (adapted from Tyson R K, 1998)

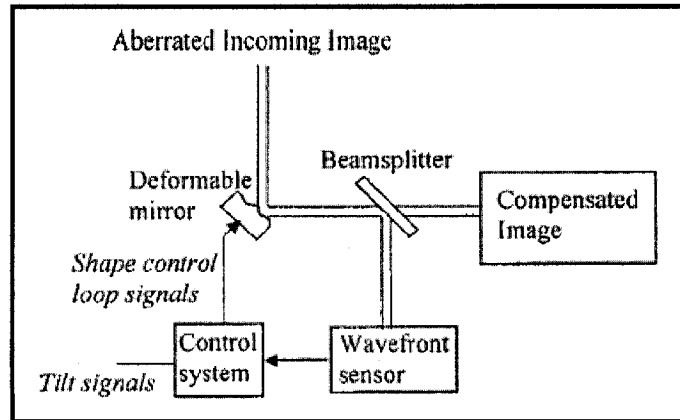


Fig. 1. 10. A simple adaptive-optical imaging system (adapted from Tyson R K, 1998)

The principles of adaptive optics are based on the promise that one can change the effects of an optical system by adding, removing or altering optical systems. When mechanical or thermal defects degrade the image or propagation process beyond the diffraction limit, we can try to alter the optical system to compensate for the defects even though we cannot get rid of them, as shown in Fig. 1. 9. An adaptive optic system shown in Fig. 1. 10 is composed of a wavefront phase sensor, focusing optics, and a spatial light modulator to correct phase errors. Modulation of an optical wavefront can be accomplished with a deformable mirror in combination with a wavefront sensor and a real-time controller.

The simplest form of adaptive optics is tip/tilt correction, which corresponds to the tilts of the wavefront in two dimensions. A significant fraction of the aberration introduced by the atmosphere can be removed by using segment mirrors. While, the continuous surface deformable mirror are needed for high resolution over a large spectral range that requires good corrections of astigmatism, coma, spherical aberration, and higher order aberrations.

The MEMS based deformable mirrors, an inexpensive and high-performance alternative device, are enabling insertion of AO into a greatly expanded set of optical systems. Bulk micromachined membrane mirrors, usually incorporating a tensile silicon nitride membrane, have been fabricated with reasonable success [Gleb V and Lina S, 1994; Kurczynski P et al., 2004]. Their capability are critical for systems in which aberrations affect optical beam quality, including many applications in laser communication [Thompson Charles A et al., 2003], medical imaging [Restaino S R et al., 2005], ophthalmic phoropters [Yuhua Z et al., 2006] and fundus imaging systems [Doble N and Williams D R 2004], which are used by eye doctors to image the retina and detect degenerative eye disease.

1.5 The Suitable Actuation Methods of MEMS Deformable Mirrors

The ability to manufacture the mechanical parts of the micromirrors does not fully solve the problem. The challenge is also to understand and control the physical systems behavior on these scales. In order to understand the behavior of electrostatic, electromagnetic, thermal, and mechanical forces on the micro length scale it is necessary to understand the operation and function of MEMS devices.

The methods of actuation and sensing for these new devices have been critically important these years. It should be kept in mind, however, that there is no perfect method and the decision mainly depends on the actual device and the specification of the system. Types of MEMS actuation and sensing properties were discussed in [Kovacs G, 1998]. Thus, we can easily compare characteristics, advantages and drawbacks of each of them

in Table 1. 2. All of them have their advantages and drawbacks, and they are basically related to the selected fabrication method.

Table 1. 2. Comparison between actuation and sensing methods
(adapted from Kovacs G, 1998)

	Parameter	Local circuits	DC response	Complex	Linearity	Issues
Piezoresistive	strain	No	Yes	+	+++	High temperature dependence; Easy to integrate
Piezoelectric	force	No	No	++	++	High sensitivity; Fabrication complex
Electrostatic	displacement	Yes	Yes	++	poor	Very simple; Low temperature coefficients
Thermal	strain	No	Yes	+	poor	Cooling problems; Interference with electronics
Magnetic	displacement	No	Yes	+++	+	Very complex; Post fabrication
Optical	Displacement	No	Yes	+++	+++	Difficult to implement

Piezoresistive sensing is a common method in engineering to measure strain and displacements. Since doped-silicon or polysilicon that have piezoresistive properties can be easily microfabricated. Piezoresistive sensing is easy to integrate, and many viable applications exist [Chui et al., 1998; Tortonese et al., 1993] based on their sensing techniques. However, its dependence on temperature and fabrication stress calibration greatly limits its application in optics.

Piezoelectric materials are used for actuation and sensing, but the sensing is limited due to their lack of DC response. Their properties are well known in view of their use for decades. Most of the conventional deformable mirrors used piezoelectric actuation, and it is still used nowadays. When using silicon-based sensors, post-processing is needed to deposit the material, such as ZnO or PVDF. However, their high temperature sensitivity, nonlinear working zones and hysteresis prevent their use in sensor applications.

Thermal actuation is easy to implement. The difficulty lies in isolating the temperature zones. The possible interferences with other thermally dependent elements or control electronics limit their applications, especially, in high density mirror array.

Magnetic actuation is a common method in the macroworld. However, it is not easily scaled to MEMS devices. The main problem is that the reduction of the achievable forces is a factor of ten thousand when the sizes are reduced by a factor of ten. This fact, combined with the fabrication difficulties, limits the application of magnetic actuation at microlevel.

Optical actuation and sensing is a desirable method, due to its non-interfering property. The necessity of integrating a light source, building reflecting surfaces and aligning the whole set-up is time demanding and no batch-fabrication based implementation methods exist now.

The comparison shows that electrostatic actuation and sensing are really desirable methods in microlevel. It is straightforward to build a capacitor with the existing microfabrication methods. This simplicity has made electrostatic actuation and sensing

ubiquitous. Nowadays, capacitive effects are used in resonators [Attia P et al., 1998], RF switches [Huang J M et al., 2003; Wong A C et al., 1998], shunt switches [Goldsmith et al. 1996], accelerometers [Kuehnel W, 1995], optical switches [Satoshi I et al., 2003], micro-pumps [Teymoori and Abbaspour-Sani, 2002], gyroscopes [Juneau T N, 1997], pressure sensors, microscopy, etc. At the same time, the inherent drawbacks of electrostatic actuation are also challenging the engineers who want to embed electrostatic actuation in their microdevices.

1.6 MEMS Deformable Mirrors

Although it seems practically and economically attractive, capacitive actuation has its own drawbacks and challenges. Although large forces can be generated by electrostatic actuators, they are generally highly non-linear. Therefore, the good understanding of the phenomena is essential in order to obtain a high performance device with electrostatic actuation and sensing. And this becomes more relevant given the increasing number of new devices that are continuously designed using these methods of actuation and sensing.

1.6.1 Common Phenomena in Electrostatic Actuation

1.6.1.1 Highly Nonlinear Electrostatic and Mechanical Coupling

In the electrostatically actuated system, the electrostatic forces not only cause the structure to deform but also alter its dynamic properties at the same time [Muthukumaran P et al., 1999 and 2002; Rinaldi G et al., 2004]. The electrostatic forces weaken the structure resulting in elastic softening of the structure [Hu Y C et al., 2004]. The electrostatic force which is always attractive and proportional to the square of the applied

voltage, will act to pull the top structure towards the base electrode. With the structure deforming, the electrostatic fields redistribute and modify the mechanical loads. This interaction continues until the suspended structure reaches a new equilibrium position.

In the case of large deformable mirrors with electrostatic actuators, they do not include the effect of small deformation on the actuator gap spacing [Grosso R P and Yellin M, 1967]. However, in the MEMS based deformable mirrors with electrostatic actuators, the micromirror surface deformations are of the same order of magnitude as that of the gap. Thus, it becomes necessary to use nonlinear actuator models [Wang P K C and Hadaegh FY, 1996].

1.6.1.2 Pull-In Instability

Applied voltage on an electrostatic actuator can have both DC and AC components. The electric load acting on a capacitor is composed of a DC polarization voltage for bias and an AC voltage for dynamic excitation. The DC voltage applies electrostatic force on a suspended structure, thereby deflecting it to a new equilibrium position and the AC voltage vibrates the microstructure around this equilibrium position. The combined electric load has an upper limit. Otherwise, the mechanical restoring force of the microstructure cannot resist the opposing electrostatic force. The whole system becomes unstable in this situation. The suspended microstructure will suddenly snap down to the stationary electrode when the electrostatic force exceeds the mechanical restoring force. This structural instability phenomenon is well known as ‘pull-in’ [Senturia S D, 2000] and the corresponding critical applied voltage is called ‘pull-in voltage’, as shown in Fig. 1. 11.

There are many studies on accurately predicting the pull-in voltage and response time of the microstructures, such as [Choi B and Lovell E G, 1997; Pamidighantam S et al., 2002]. On the contrary, a key issue in the design of MEMS deformable mirrors is to tune the electric voltage well away from the pull-in range, which would otherwise lead to collapse of the top mirror and hence a failure in the devices. An accurate prediction of the pull-in voltage will help decide the working range of deformable mirrors. In addition, when the suspended microstructures deflect, the stiffness of the systems will be reduced by the electrostatic softening, which is bound to change the response time and resonance frequencies of the systems.

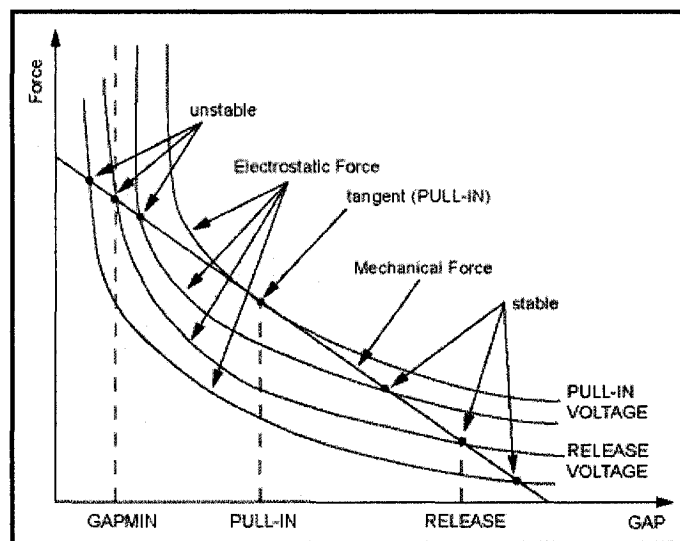


Fig. 1. 11. Static stability characteristics (adapted from ANSYS Help)

1.6.1.3 Cross Talk in Electrostatic Actuators

Although, numerous studies have analyzed the mathematical models of the electrostatic actuation in an attempt to further understand and control the pull-in instability, the complete dynamics of the electrostatically coupled mechanical system is still not totally

explored. Some possible effects are edge effects of one capacitor or cross talk between the electrostatic actuators.

If the aspect ratio (the ratio of the plate separation to the width of capacitor) is very small, the fringe field of the edges can be neglected. However, for MEMS basic devices, whose aspect ratio is not small, the edge effect becomes important. The boundary element method (BEM) was used to calculate the capacitance of a strip capacitor including the edge effect [Nishiyama H and Nakamura M, 1990]. The same technique was applied for parallel plate disk capacitors and those with large separation [Nishiyama H and Nakamura M, 1993 and 1994]. It is obvious that BEM is very suitable for precisely calculating the capacitances for MEMS devices with single electrostatic actuator. However, in high density electrostatic actuator array, there is still no effective method suitable to predict the influence of edge effects.

1.7 Objectives of Thesis Research

Based on the above-described background, the objectives of this dissertation research are established as modelling and simulation of MEMS deformable structures that are actuated by multiple electrostatic actuators. The suspended microstructures are considered as microbridges and micromirror plates for analysis. Although the low-stress micromachined membrane deformable mirrors (MMDM) have shown many advantages in adaptive optics, the microstructures analyzed here are not just limited to such applications. The above objectives are outlined below in more detail:

- a) To build the model that includes the basic structures of deformable microstructures, including suspended microbridges or microplates and the electrode arrays underneath. The nonhomogeneous boundary conditions are modelled simulating the support condition due to micromachining processes. To demonstrate the influence of a support condition for current MEMS technologies.
- b) To develop an ANSYS model and simulate the results for static and dynamic response of microstructures with multiple electrostatic actuators.
- c) To investigate the results from numerical model and ANSYS simulation, understand the limitation in the numerical method so as to efficiently define the safety working range.
- d) To design and install the experimental setup for displacement measurement. To review the experimental results on measuring the static deflections of the microstructures, microbridges, under different applied voltages.
- e) To validate the Rayleigh Ritz method by comparing prediction model against ANSYS and experimental results.

1.7.1 Thesis Organization

This thesis is divided into seven chapters. As described above, the first chapter provides a summary and outlines of the problems associated with multiple electrostatic actuators and objectives of the thesis.

Chapter 2 shows a general model that can be used to analyze the static deflection and dynamic response of the microbridge subjected to multiple electrostatic actuators. The current method is extended for micromirror plates with multiple electrostatic actuators in

Chapter 3. Chapter 4 presents a simulation method that is used for electromechanical coupled problems using ANSYS. The advantages and drawbacks of this mathematical model are also investigated by comparing with ANSYS simulation results. Chapter 5 presents microfabrication methods and technologies to manufacture the devices. Wire bonding post process is also provided in this chapter. Chapter 6 outlines the equipment and the methods used in building the experimentation for measuring the deflection of the microbridge under different set of applied voltages. The selected experimental data are also used for comparison. Chapter 7 provides a summary and conclusions of this thesis along with recommendations for future studies.

Chapter 2

2 MODELING OF DEFORMABLE MICROBRIDGE WITH MULTIPLE ELECTRODES

2.1 Introduction

The electrostatic principle is frequently used in sensing and actuation of MEMS devices. The pull-in phenomenon is widely used in RF applications nowadays. Numerous investigators have analyzed mathematical models of electrostatic actuation in attempts to further understand and control the pull-in instability in the last several years. Some of their studies dealt with various load conditions, pull-in voltages and dynamic behavior of clamped-clamped micromachined beams. For example, stretching effects of doubly clamped microbeams under mechanical and electrostatic loads have been derived and verified by numerical simulation in Ref. [Choi B and Lovell E G, 1997]. A simple lumped spring-mass system was used to analyze the pull-in voltage of clamped-clamped beams and a closed form expression, which included axial stress, nonlinear stiffness, charge distribution and fringe fields, was also derived by [Pamidighantam S et al., 2002]. Rayleigh Ritz method was used by [Tilmans H A C and Legtenberg R, 1994] to approximately estimate the fundamental natural frequency, which was in good agreement with the experimental results. Electrostatic force causing the shifting of natural frequency was studied by electro-mechanical coupling [Lee W S et al., 2001]. Recently, a new finite element approach was proposed to model electro-mechanical coupling based on monolithic formulation [Rochus V et al., 2006]. Although the simple mass-spring model can approximate the basic dynamics, it cannot predict the inherent nonlinearities of the electrostatic force and the beam deformation [Chu P B et al., 1996]. The better

results can be achieved in using partial differential equations and linearizing around the working point, as the static deflections and dynamic response only apply for small deflection zones [Jntema D J and Tilmans H A C, 1992]. Most of the above studies focus on the resonant frequencies of micro devices. Their applications do not require precisely controlling deflection shape of micromachined structures under different applied voltages. What is more, the nonhomogeneous boundary conditions which are inherent in MEMS structures did not get enough emphasis in the previous studies.

Meanwhile, deformable mirrors with multiple actuators are widely used in adaptive optics, as they can compensate for the wave front variations [Tyson R K, 1998]. The influence functions [Claflin E S and Bareket N, 1986; Menikoff A, 1991] are used to describe the shape deformation of the thin elastic plate type mirrors, which are analyzed based on the theory of pure bending [Timoshenko S P and Krieger W, 1959]. In recent years, the micromachined membrane deformable mirrors (MMDM) provide a low-cost and compact solution for the adaptive optical systems [Claflin E S and Bareket N, 1986]. The small displacements of a MMDM are governed by Poisson's equation. In these devices, the gap spacing of electrostatic actuators is of the same order in magnitude as that of mirror surface deformations. Due to the nature of the problem, a nonlinear computation model is generally necessary for the analysis of MMDM surface deflection. However, in this nonlinear computation model, the surface deformation is described by nonlinear partial differential equations [Wang P K C and Hadaegh F Y, 1996]. The required voltages are determined by solving these equations with known boundary conditions. These approaches greatly rely on accurate knowledge of the device

parameters which are usually not available with desired precision in practice [Zhu L J et al., 1999].

This chapter mainly focuses on the numerical analysis of static deflections and dynamic behaviors of microstructures, microbeams and microplates, which are working under multiple electrostatic actuators. The boundary conditioning is modeled by using rotational springs and translational springs, as shown in Fig. 2. 1, so as to simulate the influence of non-classical microfabricated end supports and electrostatic operating environment [Laura P A A et al., 1977 and 1981; Muthukumaran P et al., 1999, 2000, 2002]. The boundary characteristic orthogonal polynomials, proposed by [Bhat R B, 1985] are applied in the Rayleigh Ritz method. The influence function which relates the external force with deflection of the structure can be built by using boundary conditioning in the proposed method. It is possible thus to obtain required voltages for the actuators corresponding to certain deformation using influence functions. Meanwhile, the required voltages can also be used for determining the dynamic response of the microstructure.

The accuracy of this approach depends upon the accuracy of the calculated or measured influence functions [Claflin E S and Bareket N, 1986; Menikoff A, 1991], which are also determined by the boundary conditions. The following sections will present the theoretical modeling and results. Accuracy and limitations of this approach will also be discussed by comparing with ANSYS simulation results in Chapter 3.

2.2 Electrostatically Actuated Microbeams

2.2.1 Model of a Microbridge

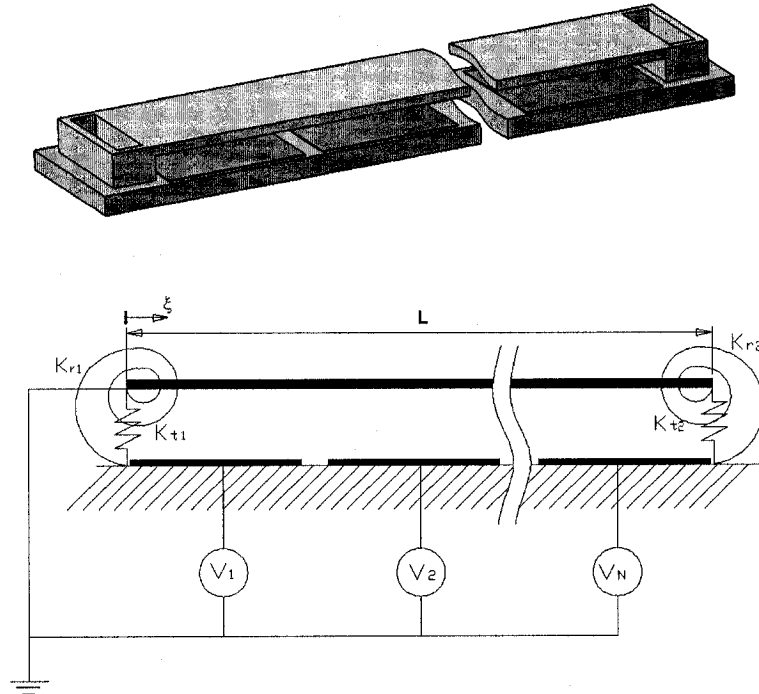


Fig. 2. 1. The schematic of a microbridge

The static and dynamic behaviours of micromachined structures greatly depend on the elastic properties of the system. In practice, the boundary conditions of these kinds of structures are not always homogeneous, such as, clamped or simply supported, and it can be flexible both in translation and rotation [Muthukumaran P et al., 1999 and 2002; Rinaldi G et al., 2004]. In this study, boundary condition is modeled by rotational and translational springs at both fixed ends of a microbridge as shown in Fig. 2. 1, where, K_t represents the spring constant of the translational spring and K_r , is the stiffness of the rotational spring.

Adopting this approach to characterize the nonhomogeneous end conditions that are inherent in MEMS structures and the influence of electrostatic field will help represent the changes in the elastic property of the system due to the boundary conditions and electrostatic field and improve upon the existing methods in order to accurately predict the static and dynamic behaviors of the micro structures with electrodes.

2.2.2 Static Analysis

An assumed deflection that satisfies the geometrical boundary conditions is used in energy method for a continuous system. Here, the flexural deflection of the microbridge is assumed as,

$$W(x) = \sum_{i=1}^J A_i \phi_i(x) \quad (2.1)$$

where, ' $\phi_i(x)$'s, are the boundary characteristic orthogonal polynomials as proposed in [Bhat R B, 1985] which are generated by the Gram-Schmidt orthogonalization process, ' A_i 's are the arbitrary coefficients and J is the total number of orthogonal polynomials used. Here, x is a non-dimensionalized quantity which is equal to ξ/L , where ξ is the longitudinal coordinate, and L is the length of the microbridge.

The total energy (U_{tal}) of the beam includes the strain energy of the beam due to bending (U_p), the potential energy of the boundary springs (U_s), and the energy due to the electrostatic field (U_e).

$$U_{tal} = U_p + U_s + U_e \quad (2.2)$$

$$U_p = \frac{EI}{2L^3} \int_0^1 (W''(x))^2 dx \quad (2.3)$$

$$U_s = \frac{1}{2} K_{t1} (W(0))^2 + \frac{1}{2} \frac{K_{r1}}{L^2} (W'(0))^2 + \frac{1}{2} K_{t2} (W(1))^2 + \frac{1}{2} \frac{K_{r2}}{L^2} (W'(1))^2 \quad (2.4)$$

$$U_e = -\frac{\varepsilon_r \varepsilon_0 w L}{2} \sum_{n=1}^N \int_{x_{2n-1}}^{x_{2n}} \frac{V_n^2 dx}{[d_0 - W(x)]} \quad (2.5)$$

where, K_{ts} is the translational spring stiffness at s^{th} side

K_{rs} is the rotational spring constant at s^{th} side, and $s=1,2$.

w is the efficient width of the electrodes. It is the same as the width of the microbridge in this model.

Expanding the nonlinear electrostatic energy term in Eq. (2. 5) by Taylor series with respect to the initial position,

$$U_e = -\frac{\varepsilon_r \varepsilon_0 w L}{2d_0} \sum_{n=1}^N V_n^2 \int_{x_{2n-1}}^{x_{2n}} \left[1 + \frac{W(x)}{d_0} + \left(\frac{W(x)}{d_0} \right)^2 + \dots \right] dx \quad (2.6)$$

Based on small displacement assumption, the Taylor's series expansion is used to simplify the equation and only up to quadratic terms are considered as follows,

$$U_e = -\frac{\varepsilon_r \varepsilon_0 w L}{2d_0} \sum_{n=1}^N V_n^2 \int_{x_{2n-1}}^{x_{2n}} \left[1 + \frac{W(x)}{d_0} + \left(\frac{W(x)}{d_0} \right)^2 \right] dx \quad (2.7)$$

The static equilibrium deflection of the microbridge can be obtained by minimizing the total potential energy in Eq.(2. 2) with respect to A_j and solving the resulting simultaneous equations given by,

$$\begin{aligned}
& \sum_i^J \left\{ \int_0^1 \phi_i''(x) \phi_j''(x) dx + K_{i1}^* \phi_i(0) \phi_j(0) + K_{r1}^* \phi_i'(0) \phi_j'(0) + \right. \\
& \left. K_{r2}^* \phi_i'(1) \phi_j'(1) + K_{i2}^* \phi_i(1) \phi_j(1) - F_1 \left[\sum_{n=1}^N V_n^2 \int_{x_{2n-1}}^{x_{2n}} \phi_i(x) \phi_j(x) dx \right] \right\} A_i \\
& = F_2 \left[\sum_{n=1}^N V_n^2 \int_{x_{2n-1}}^{x_{2n}} \phi_j(x) dx \right]
\end{aligned} \tag{2.8}$$

$$i = 1, 2, \dots, J \quad \text{and} \quad j = 1, 2, \dots, J$$

$$\text{where, } K_{ts}^* = \frac{K_{ts} L^3}{EI}, K_{rs}^* = \frac{K_{rs} L}{EI}, (s = 1, 2); F_1 = \frac{\varepsilon_0 \varepsilon_r w L^4}{E I d_0^3} \text{ and } F_2 = \frac{d_0 F_1}{2}$$

The maximum values of i and j are determined by the number of boundary characteristic orthogonal polynomials J in the Eq. (2. 1). The solutions of Eq. (2. 8) lead to static equilibrium deflection of the microbridge. Thus, it is possible to predict different static equilibrium deflections under various applied voltages.

In the case of clamped-clamped boundary supports, the end conditions are modeled by very high values of rotational stiffness and translational stiffness. Some geometry constants are chosen as given in Table 2. 1, so as to test the model in the following cases:

Table 2. 1. Geometry constants for the microbridge model

Length (μm)	Width (μm)	Thickness (μm)	Initial Gap of Electrostatic Actuators (μm)	Young's Modulus E (GPa)
350	100	1	3	130

2.2.3 Static Influence Functions

A microbridge as shown in Fig. 2. 2 with three electrostatic actuators are used for illustration. The deflections of node points on the microbridge beam, whose location correspond to the centre of the bottom electrodes, are considered. The static deflection of the beam is shown in Fig. 2. 3 when unit voltage is applied at the bottom electrodes individually. These responses under unit bias voltages at any electrode are called *Influence Functions*. The elastic foundation in Fig. 2. 2 represents elastic effect due to electrostatic softening. The static deflections of nodal points under the influence of different applied voltages at the central electrode are shown in Fig. 2. 4. It indicates that the deflection of the microbridge is generally nonlinear with respect to the applied voltages. However, the deflection from Eq. (2. 1) in which the ' A_i 's are determined by the solution of Eq. (2. 8) is plotted against the square of the applied voltage in Fig. 2. 5, which shows a linear relation in a certain region. Here, we can make use of this property and try to combine the deflections that are caused by each of the electrostatic actuators to represent the shape of the whole microbridge. It will also be used to estimate the required voltages at each electrostatic actuator for a desired deflection hereafter.

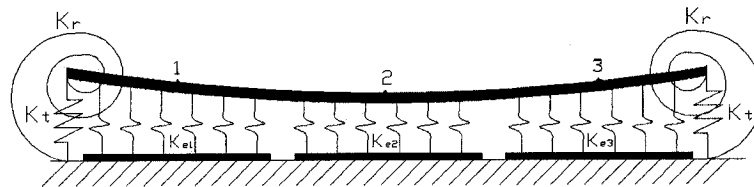


Fig. 2. 2. The scheme of a three-electrode microbridge under the electrostatic force

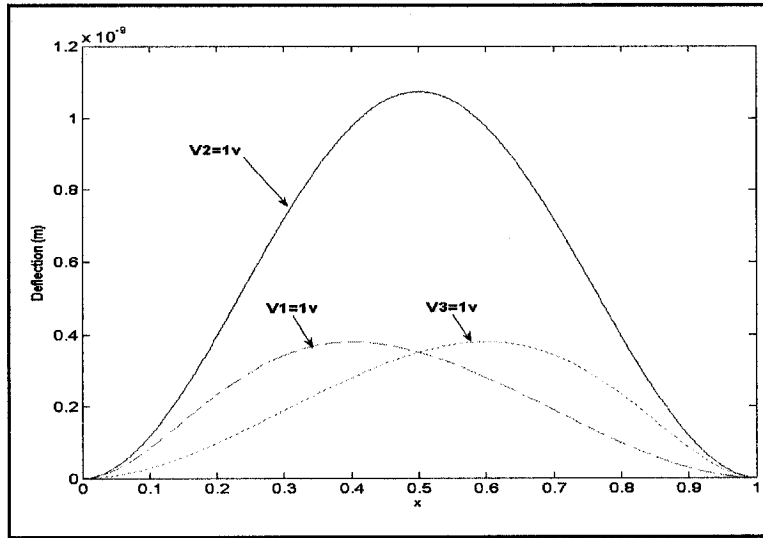


Fig. 2. 3. Influence functions of the microbridge with three electrostatic actuators

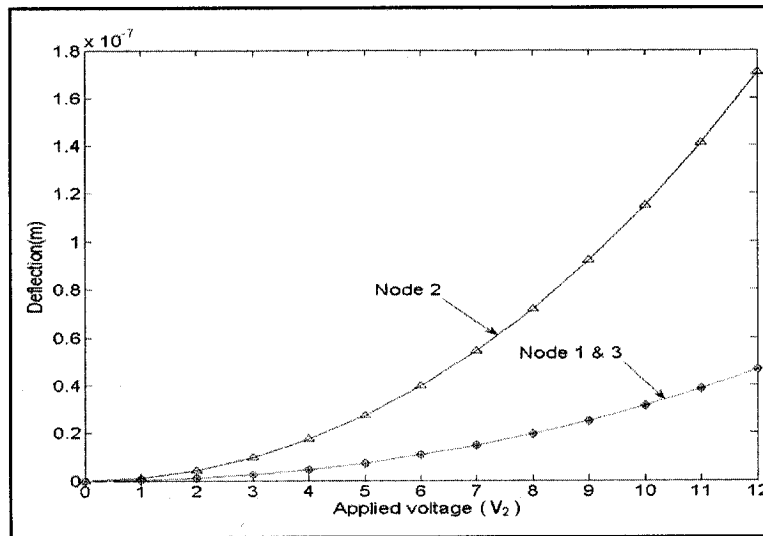


Fig. 2. 4. Static deflection of three node points when voltage applied only at the central actuator ($V_1=V_3=0, V_2 \neq 0$)

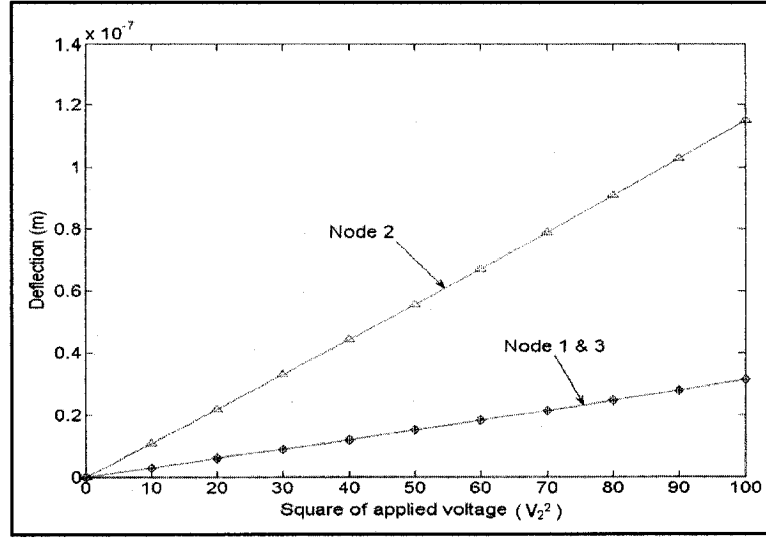


Fig. 2. 5. The influence function having linear relationship between nodal displacement and square of applied voltage on the central actuator ($V_1=V_3=0, V_2 \neq 0$)

We define $C_n(x)$ to be the influence function of microbridge due to the n^{th} actuator, which represents the deflection of the microbridge due to the n^{th} actuator under unit voltage. The deflection of the microbridge structure is now represented by a linear combination of these influence functions as,

$$W(x) = \sum_{n=1}^N C_n(x) V_n^2 \quad (2.9)$$

Defining $U_n(V) = V_n^2$, the Eq. (2.9) can be rewritten as,

$$W(x) = \sum_{n=1}^N C_n(x) U_n(V) \quad (2.10)$$

where, N is the total number of electrodes.

Above equation provides the deflection as a linear combination of deflections due to many electrostatic actuators. The results shown in Fig. 2. 6, shows perfect agreement between the curves W and $W3$, validating the assumption of linear relation of deflection and the square of applied voltage. $W3$ is the deflection obtained for $V1=2$ V, $V2=0$, $V3=3V$ by solving Eq. (2. 8). W is the linear combination deflections using influence functions for $V1=2$ V and $V3=3$ V. Similarly, the close agreement between the curves W and $W2$ in Fig. 2. 7 also validates the use of linear combination of influence functions defined by Eq. (2. 10). In these cases, the assumption of linearity is considered safe for practical applications in which the actual deflections are small and well within the linear region of deflections less than approximately $2/3$ of the pull-in deflection.

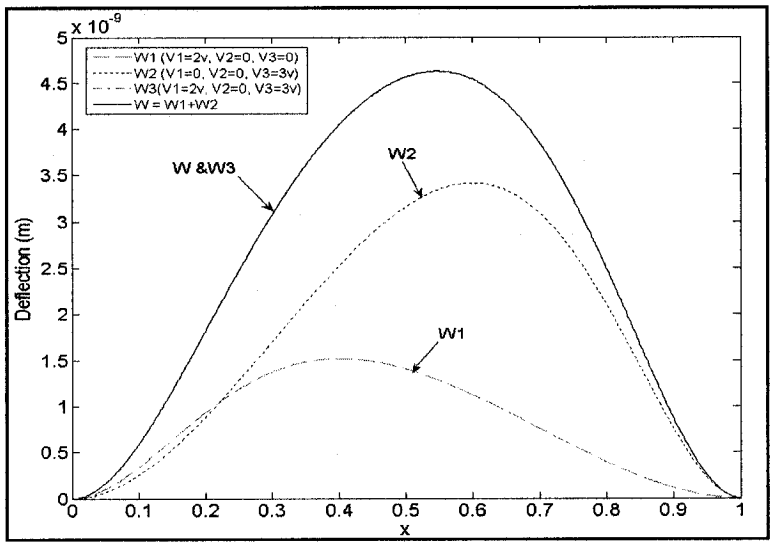


Fig. 2. 6. The deflection can be represented by combination of the influence functions

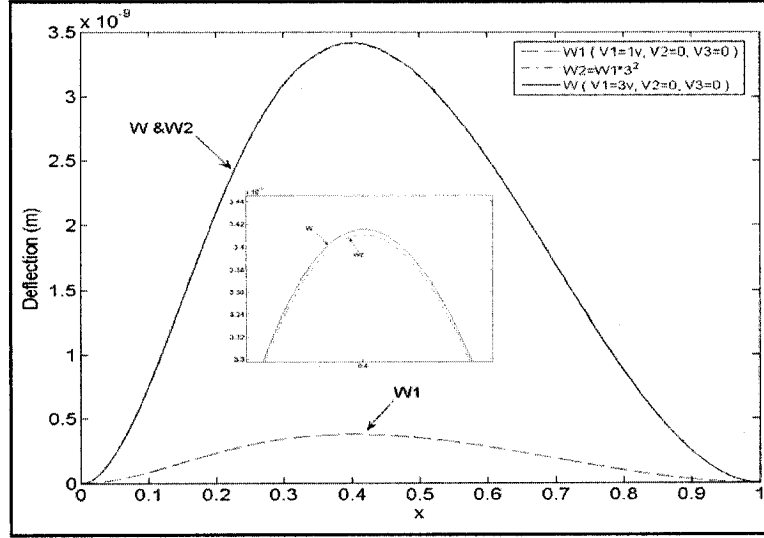


Fig. 2. 7. Deflection estimated with influence function

2.2.4 Shape Optimization

Let $\psi(x)$ be the desired shape of the microbridge. The residual error between the actual deflection $W(x)$ and the desired deflection $\psi(x)$, is taken as the function defined as follows:

$$\begin{aligned}
 ER &= \int_0^1 [W(x) - \psi(x)]^2 dx \\
 &= \int_0^1 \left[\sum_{n=1}^N C_n(x) U_n(V) - \psi(x) \right]^2 dx
 \end{aligned} \tag{2.11}$$

For easier implementation, optimization of the shape is normally carried out at discrete nodal points which are numbered from 1 to M here. One has to be careful in selecting the nodes so that the optimization of the nodal deflection will ensure the required shape because it is hard to achieve any kind of shape just using a certain number of electrostatic actuators.

Considering a set of nodal points, the residual error function Eq. (2. 11) is rewritten as,

$$ER = \sum_{p=1}^M \left[\sum_{n=1}^N C_n(x_p) U_n(V) - \psi(x_p) \right]^2 \quad (2. 12)$$

where, M is the total number of the nodal points, which can be any point on the microbridge along the x -direction and $C_n(x_p)$ is the influence function at the point x_p due to unit voltage at the n th actuator. $C_n(x_p)$ is defined as C_{np} hereafter.

The residual error ER is minimized with respect to $U_g(V)$ by using least-square fitting method as follows:

$$\sum_{p=1}^M \left[\sum_{n=1}^N C_{np} C_{gp} U_n(V) - \psi(x_p) C_{gp} \right] = 0 \quad (2. 13)$$

$$g = 1, 2, \dots, N$$

Rewriting Eq. (2. 13) in matrix format results in,

$$\sum_{p=1}^M C_p U = \sum_{p=1}^M \Phi_p \quad (2. 14)$$

where, $C_p = C_{np} C_{gp}$ and $\Phi_p = \psi(x_p) C_{gp}$

Φ_p and U are $N \times 1$ vectors and C_p is an $N \times N$ matrix.

Defining the following:

$$\tilde{\psi} = [\psi(x_1), \psi(x_2), \dots, \psi(x_M)] \quad (2.15)$$

$$\tilde{C}_n = [C_{n1}, C_{n2}, \dots, C_{nM}]^T \quad , \quad n=1,2,\dots,N \quad (2.16)$$

$$R = [\tilde{C}_1, \tilde{C}_2, \dots, \tilde{C}_N] \quad (2.17)$$

and substituting Eq. (2.15) to (2.17) into Eq. (2.14), yield:

$$\Phi = \sum_{p=1}^M \Phi_p = (\tilde{\psi}R)^T = R^T \tilde{\psi}^T \quad (2.18)$$

$$C = \sum_{p=1}^M C_p = R^T R \quad (2.19)$$

$$R^T R U = R^T \tilde{\psi}^T \quad (2.20)$$

Therefore, we can obtain the optimum voltage from:

$$U = (R^T R)^{-1} R^T \tilde{\psi}^T \quad (2.21)$$

The optimization procedure can be summarized as follows. First of all, energy method is used to derive each influence function $C_n(x)$. And then, $\psi(x)$, an initial deflection profile is selected that could be a measured shape or a desired deflection. Thus, Eq. (2.21) can be used to estimate the required voltages. Finally, the optimized voltages are used to generate a static deflection $W(x)$, which can be easily compared with the desired deflection.

2.2.5 Dynamic Analysis

The electrostatic force which is always attractive and proportional to the square of the applied voltage, will act to draw the top structure downward. As the structure deforms, the electrostatic fields redistribute and modify the mechanical loads. Here, the change in electrostatic effects with structural deformation has to be taken into account in the analysis.

The dynamics of a microbridge which is subjected to bias voltages is studied in this section. As is well known, the dynamic characteristics of a structure depend on the material properties, geometrical dimensions and boundary conditions. In the electrostatically actuated system, the electrostatic forces not only cause the structure to deform but also alter its dynamic properties at the same time [Rinaldi G et al., 2004] through electric softening. The electrostatic forces weaken the structure resulting in elastic softening of the structure.

For the dynamic behavior of the microbridge, the contribution of the kinetic energy must be taken into account. At the same time, electrostatic stiffness K_{es} will also be calculated in order to represent the influence of electrostatic field that was generated by every electrostatic actuator using the method of artificial springs as shown in Fig. 2. 2.

As earlier, the dynamic flexural deflection $W_d(x)$ of the microbridge is defined similar to Eq. (2. 1), so that each function of $W_d(x)$ also satisfies the essential boundary conditions.

The kinetic energy of the microbridge is given by,

$$T_{\max} = \frac{1}{2} \rho \omega t L \omega^2 \int_0^1 [W_d(x)]^2 dx \quad (2.22)$$

where, ρ is the mass density and ω is the natural frequency.

The electrostatic stiffness of each actuator is estimated at the static equilibrium deflection, namely $W(x)$. The maximum potential electrostatic energy due to the dynamic deflection is obtained by subtracting the electrostatic potential energy due to static deflection from the total electrostatic potential energy as,

$$U_{d,e} = \frac{\varepsilon_0 \varepsilon_r \omega L}{2} \sum_{n=1}^N \left\{ \int_{x_{2n-1}}^{x_{2n}} \frac{V_n^2}{d_0 - [W(x) + W_d(x)]} dx - \int_{x_{2n-1}}^{x_{2n}} \frac{V_n^2}{d_0 - W(x)} dx \right\} \quad (2.23)$$

By Taylor's series expansion with respect to the static equilibrium point and taking only up to the linear term based on the small deflection assumption, the Eq. (2.23) is reduced to the form,

$$U_{d,e} = \frac{\varepsilon_0 \varepsilon_r \omega L}{2} \sum_{n=1}^N \left\{ \int_{x_{2n-1}}^{x_{2n}} \frac{V_n^2 W_d(x)}{[d_0 - W(x)]^2} dx \right\} \quad (2.24)$$

and the electrostatic forces at the static equilibrium position can be achieved as,

$$F_{d,e} = \frac{\partial U_e}{\partial [d_0 - W(x)]} = -\varepsilon_0 \varepsilon_r \omega L \sum_{n=1}^N \left\{ \int_{x_{2n-1}}^{x_{2n}} \frac{V_n^2 W_d(x)}{[d_0 - W(x)]^3} dx \right\} = \sum_{n=1}^N \int_{x_{2n-1}}^{x_{2n}} K_{en} W_d(x) dx \quad (2.25)$$

where, $K_{en} = -\frac{\varepsilon_0 \varepsilon_r w L V_n^2}{[d_0 - W(x)]^3}$ is the softening stiffness per unit normalized length due to the n^{th} electrode actuator. x_{2n-1} and x_{2n} are two end coordinates of the n^{th} fixed electrode along x direction.

The potential energy of artificial springs due to electrostatic forces is represented as,

$$U_{d,e} = \sum_{n=1}^N U_{d,en} = \sum_{n=1}^N \frac{1}{2} \int_{x_{2n-1}}^{x_{2n}} K_{en} [W_d(x)]^2 dx \quad (2.26)$$

The maximum strain energy with reference to the static equilibrium is estimated by,

$$U_{\max} = U_{d,p} + U_{d,s} + U_{d,e} \quad (2.27)$$

Using extension of Rayleigh Ritz method [Thomsen J J, 2003], the coefficients of the dynamic flexural deflection coefficients A_i are estimated by minimizing the Rayleigh quotient, R as:

$$\frac{\partial U_{\max}}{\partial A_j} - R_j \frac{\partial (T_{\max} / \omega^2)}{\partial A_j} = 0 \quad (2.28)$$

$$j = 1, 2, \dots, J$$

which results in

$$\sum_i^J \left\{ \int_0^1 \phi_i''(x) \phi_j''(x) dx + K_{r1}^* \phi_i(0) \phi_j(0) + K_{r1}^* \phi_i'(0) \phi_j'(0) + K_{r2}^* \phi_i(1) \phi_j(1) + K_{r2}^* \phi_i'(1) \phi_j'(1) \right. \\ \left. + \sum_{n=1}^N \int_{x_{2n-1}}^{x_{2n}} K_{en}^*(x) \phi_i(x) \phi_j(x) dx - \lambda_j^2 \int_0^1 \phi_i(x) \phi_j(x) dx \right\} A_i = 0 \quad (2.29)$$

$$\text{where, } K_{en}^*(x) = -\frac{K_{en}(x)L^3}{EI} \text{ and } \lambda_j^2 \cong \frac{\omega_j^2 \rho w t L^4}{EI}$$

Therefore, natural frequencies of the structure are given as,

$$\omega_j \cong \lambda_j \sqrt{\frac{EI}{\rho w t L^4}} \quad (2.30)$$

$$j = 1, 2, \dots, J$$

Normally, the accuracy of the Rayleigh Ritz method degenerates progressively for the higher natural frequencies. The lower frequency approximations, however, are quite satisfactory. The first three eigenvalues and natural frequencies of the clamped-clamped microbridge are compared Ref. [Thomson W T and Dahleh M D, 2003] and given in Table 2. 2.

Table 2. 2. The natural frequencies of the clamped-clamped microbridge under the zero applied voltage

n	Eigenvalue λ_n [Thomson W T and Dahleh M D, 2003]	Present Prediction Eigenvalue λ_n	Present Prediction Natural Frequency f_n (kHz)	ω_n/ω_1 [Thomson W T and Dahleh M D, 2003]	Present Prediction ω_n/ω_1
1	22.3733	22.3733	62.8132	1.0000	1.0000
2	61.6728	61.6728	173.1470	2.7565	2.7565
3	120.9034	120.9034	339.4373	5.4039	5.4039

2.3 Application to a Microbridge with Three Electrostatic Actuators

In order to demonstrate the proposed method, a three-electrode microbridge is presented. The applied voltages for each of the three bottom electrodes are assumed to be $V_1=4$ V, $V_2=1$ V and $V_3=1$ V. The solution of Eq. (2. 8) leads to a static deflection $W(x)$ with respect to the above applied voltages shown as solid line in Fig. 2. 8. The values at nodes denoted by ‘*’ in the Fig. 2. 8 can be estimated and used to describe the desired deflection shape. From Fig. 2. 8, it is very clear that the maximum discrepancy at the centre of microbridge is less than 0.5 % of the maximum deflection. This means that the desired deflection can be matched precisely in our case.

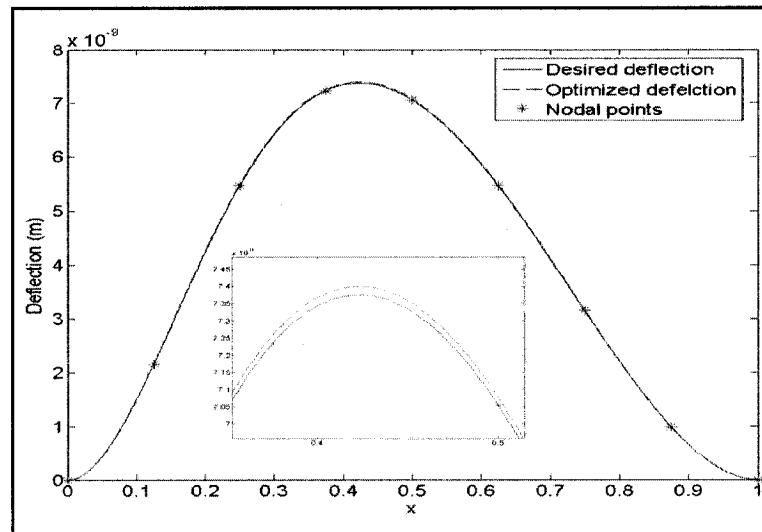


Fig. 2. 8. Comparison between the desired deflection and optimized shape

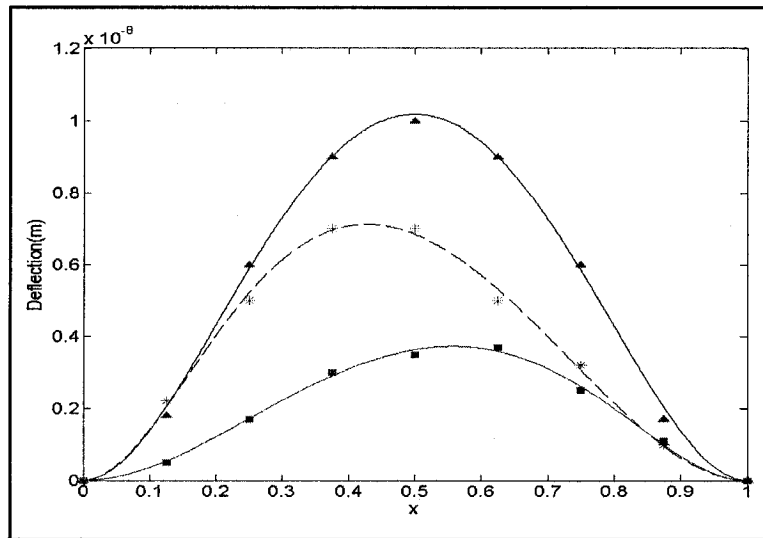


Fig. 2. 9. Three sets of fixed grid points used as input to optimize the required voltages

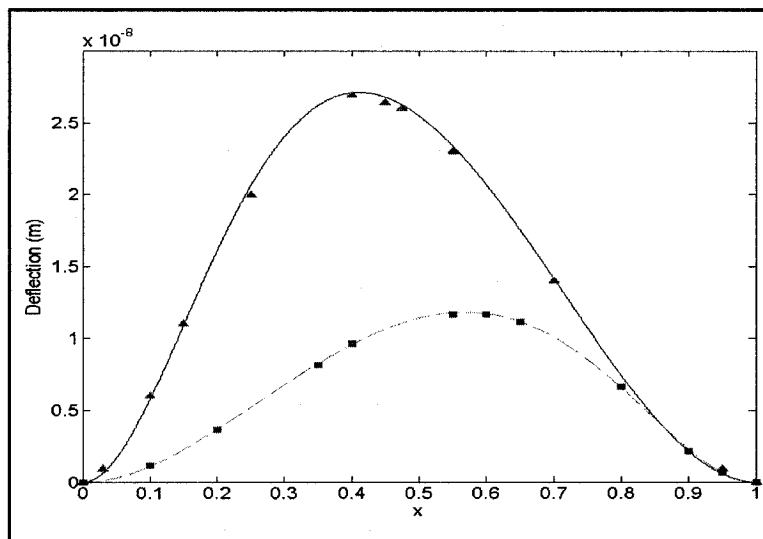


Fig. 2. 10. Two sets of random points used as input to optimize required voltages

The significant aspect of the method is that the use of the least squares method allows the freedom of choosing either a deflection function or a set of regular/ random points to describe the desired deflection. The exact deflection of the whole structure need not be known previously. The three sets of regular fixed nodal points chosen for generating the desired deflections was shown in Fig. 2. 9. In Fig. 2. 10, two sets of random points were used for searching the target shapes. The close agreements can be seen clearly from Fig. 2. 9 and Fig. 2. 10 for both regularly spaced and irregularly spaced points. According to Eq. (2. 10), the desired deflection can be represented by a linear combination of influence functions. The error is very small when using an influence function to represent the desired deflection. It will be very useful in the case of complicated shapes and large number of electrodes.

The dynamic behavior of the 3-electrode microbridge which is subjected to a bias voltage are analyzed here. It is known that the fundamental natural frequencies and mode shapes of the system mainly depend upon the material properties, geometrical dimensions and the boundary conditions. The most outstanding problem in MEMS devices is the nonhomogeneous boundary conditions of the microstructures. Translational springs and rotational springs are used in this paper to represent these kinds of nonhomogeneous boundary conditions. As the stiffness of translational springs is much higher than the rotational springs in practice, the stiffness of the right-hand side rotational spring was changed for analysis of its influence on the microbridge, as shown in Fig. 2. 11 for different Kr values of 20, 40, 80, 160 and 320 Nm/rad. The stiffness of the whole microstructure will be changed with the stiffnesses of the boundary springs.

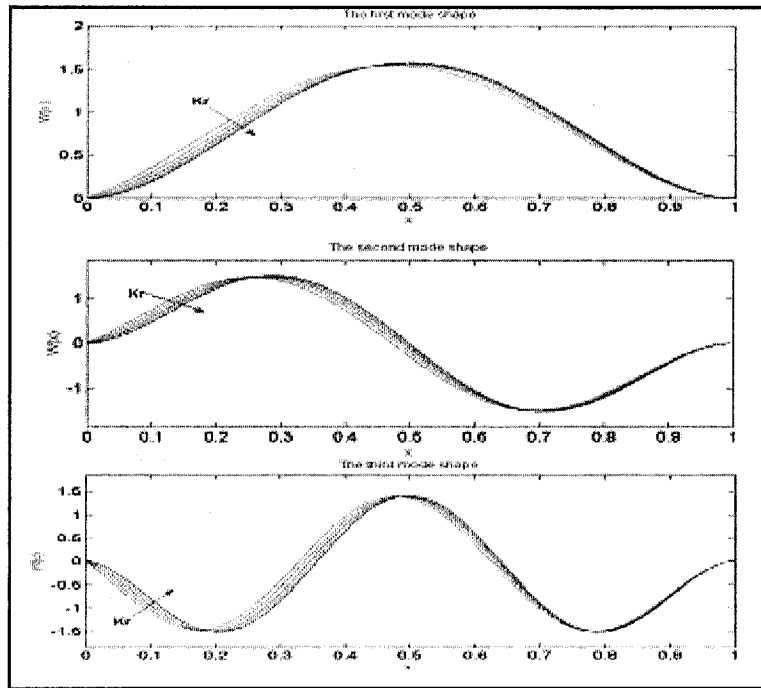


Fig. 2. 11. The first three mode shapes of the microbridge with different rotational stiffness on left hand side boundary at $V_1=V_2=V_3=0$

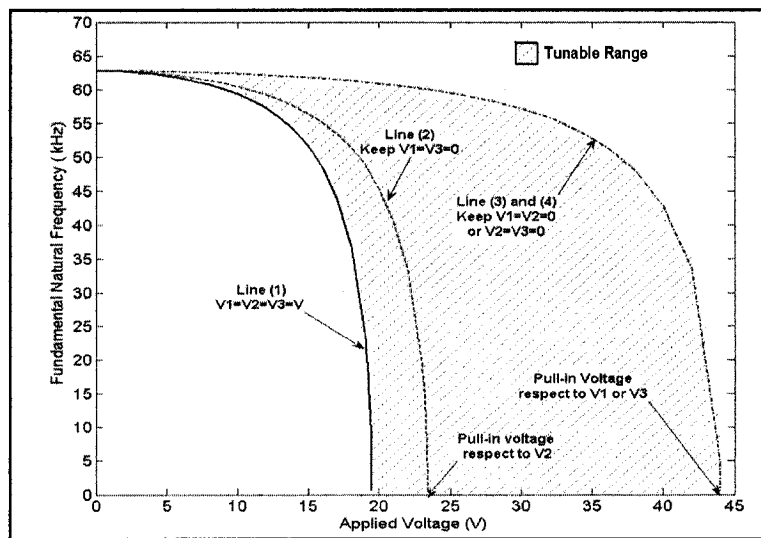


Fig. 2. 12. The variation of fundamental frequency against the bias voltages

On the other hand, the electrostatic forces will also alter the dynamic characteristics of the microstructures. The “mechanical and electrostatic coupling effects” must be taken into account in the electrostatically actuated micro systems. Because it is a multielectrode actuating system, each electrostatic actuator will affect the whole microstructure and each of the bottom electrodes would influence the stiffness of the whole microbridge differently due to its location, as seen from Fig. 2. 12. In order to understand the influence of voltage on dynamic behavior, three cases are considered here. In the first case, the same voltage was applied on all the electrodes together. One can see Line (1) from Fig. 2. 12 that frequency changes rapidly with increase in voltage and clearly shows its pull-in condition. In the second case, the effect of only the central electrode is shown. Here the Line (2) shows a similar tendency with increasing bias voltage. In the third case, the effect of side electrodes is shown. Line (3) and (4) show the influence of either of electrode 1 or electrode 3 which are the side electrodes. The results show a clear symmetrical nature of response. Thus, using the combination of the voltage on three electrode actuators, one can manipulate the natural frequency of the suspended electrode. The potential controllable region is shadowed in the Fig. 2. 12.

2.4 Summary

In this chapter, boundary conditions of the microstructure are modeled using both translational and rotational artificial spring stiffnesses. Boundary characteristic orthogonal polynomials are used in Rayleigh Ritz method in order to predict the static and dynamic behavior, create the influence function and find the optimal required voltages to achieve the desired deflection of the microbridge structure using the method

of least squares. It is clearly demonstrated that the energy based Rayleigh Ritz method can efficiently and precisely predict steady deflection and fundamental frequencies in small deflection region. The method proposed here can easily be put into use for any nonhomogeneous boundary conditions and extended for rectangular microplates as well in the next chapter. The boundary conditions of the structure, the electrode dimension and the electrode pattern can also be defined easily.

Chapter 3

3 MODELING OF DEFORMABLE MICROPLATE WITH MULTIPLE ELECTRODES

3.1 Introduction

The rapid progress in telecommunications in the last decade greatly helped the development of the optical systems to meet the needs of increased bandwidth for optical networks with terabit capacities. Micro-Electro-Mechanical System (MEMS) devices are inherently smaller, lighter, faster and much more precise than macro-scale counterparts, which make MEMS suitable for different guided wave optical applications, such as tunable filters, optical switches, waveguides and cross connectors. At the same time, the benefits of MEMS technologies, such as scalability, precision position control and reconfigurability, make optical MEMS devices attractive in a variety of image processing systems. Further more, electrostatic principle is an important branch in sensing and actuation of MEMS devices because it is straightforward to build it using existing microfabrication methods [Marques A F et al., 2005]. When voltage is applied to an electrostatic actuator, the suspended structure (electrode plate) will be pulled and deflected towards the fixed electrode. This simplicity makes electrostatic principle well suited for MEMS devices.

The Digital Micromirror Devices (DMD) are the proven examples of electrostatically actuated MEMS devices [Douglass M R, 2003; Kim S et al., 2004]. It is clear that micromirrors in DMD just change the direction of reflected light. For spatial light modulation (SLM) and specifically for phase modulation, which is the requirement in

adaptive optics (AO) systems, segment mirrors or continuous surface deformable mirrors have tremendous applications. These kinds of MEMS based mirrors have been investigated as an inexpensive and high performance alternative technology to the conventional piezoelectric deformable mirrors [Claflin E S and Bareket N, 1986]. One of these segmented micromirror devices based on micromachining of silicon was pioneered by [Miller L M et al., 1993]. Subsequently, two-layer and three-layer MEMS based deformable mirrors were designed [Mansell J D et al., 2000 and 2002]. For the wave front correction, segment mirrors can correct high spatial frequencies but is limited in temporal frequency response [Tyson R K, 1998]. In addition, the gaps between segments have an impact on overall performance. The gaps between mirrors act like a grating, which make light diffracted. These drawbacks of segment mirrors greatly limit their applications. The continuous surface deformable mirrors can be used for high resolution over a large spectral range that requires corrections of astigmatism, coma, spherical aberration and other higher order aberrations. The MEMS based continuous deformable mirrors enable insertion of AO into a greatly expanded set of optical systems, including in many applications such as in laser communication, target tracking, medical imaging and ophthalmic imaging systems [Doble N and Williams D R, 2004].

In many optoelectronic devices, micromirrors can be modeled as rigid or flexible microplates. The deformed shapes of a micromirror plate can be manipulated by strategically designing electrostatic actuators. In recent years, micromachined membrane deformable mirrors (MMDM) provide a low cost and compact solution for the AO systems [Claflin E S and Bareket N, 1986]. Influence functions are used to represent the deformation shape of the thin elastic plate type mirrors [Menikoff A, 1991]. The highly

nonlinear nature of electrostatic forces requires nonlinear computation in modeling the deformation by nonlinear partial differential equations [Wang P K C and Hadaegh F Y, 1996]. The required voltages for electrostatic actuators can be obtained by solving these equations with known boundary conditions. The knowledge of the device parameters is usually not directly available with desired precision in practice [Zhu L J et al. 1999]. The nonclassical boundary conditions of micromachined structures are also different for different microfabrication methods. It is known that the material properties, geometrical dimensions and boundary conditions keep influencing the dynamic characteristics of the microstructures. In electrostatic actuated systems, electrostatic forces not only cause the deformations of the structures but also alter their dynamic characteristics [Hu Y C et al., 2004]. As a result, the electrostatic forces soften the elastic property of the microstructures.

It is possible to model the support of microstructures with artificial springs [Muthukumaran P et al., 1999 and 2002] and also to model the microbridge with multiple electrostatic actuators [Li Y Q et al., 2006]. Based on this idea, the application was extended to microplate structures with multiple electrostatic actuators. The static deflections and dynamic responses are analyzed using the Rayleigh Ritz method [Thomson W T and Dahleh M D, 2003] using boundary characteristic orthogonal polynomials [Bhat R B, 1985]. Translational and rotational artificial springs were used at the boundary supports to model the nonclassical boundary conditions caused by microfabrication. The Influence Functions are also determined using proposed method in order to relate the external forces and the out-of-plane deflections of the microstructures. After the boundary conditions were defined, the applied voltage for each of the

electrostatic actuators can be optimized in order to achieve the desired deflections. Not only the geometrical shape of microstructures can be easily defined and changed, the actuation pattern of the electrostatic actuators can also be easily altered. The full range of natural frequency response can be obtained for various situations, such as different boundary conditions, different applied voltage on each of electrostatic actuators. The results from the Rayleigh Ritz method are compared with other published results in this chapter and are compared with Reduced Order Modeling (ROM) method in the next chapter.

3.2 Electrostatically Actuated Microplate

3.2.1 Model of a Microplate

The static and dynamic behavior of structures depends on the elastic properties of the system and the boundary conditions. MEMS microdevices are made by non-conventional microfabrication techniques. At Sandia National Laboratories, the beam support post model was used by [Jensen B D et al., 1999] to understand the boundary effects in micromachined beams. However, it is difficult to accurately measure boundary conditions, such as the beam end angle, as its size is too small for most measurement techniques. Interferometry for Material Properties (IMaP) technique was also used in measuring several boundary effects [Jensen B D et al., 1999].

In the present study, non-classical boundary conditions are modeled using rotational and translational springs at the edges of the microplate as shown in Fig. 3. 1, where, K_T represents the spring constant of the translational spring and K_R is the stiffness of the rotational spring. Thus, the flow of the energy in the microstructure will be changed by

altering rotational stiffness and/or translational stiffness. The nonclassical boundary conditions are parameterized by stiffness values of K_R and K_T . The geometry of the microplate and the parameters used in the modeling are listed in Table 3. 1.

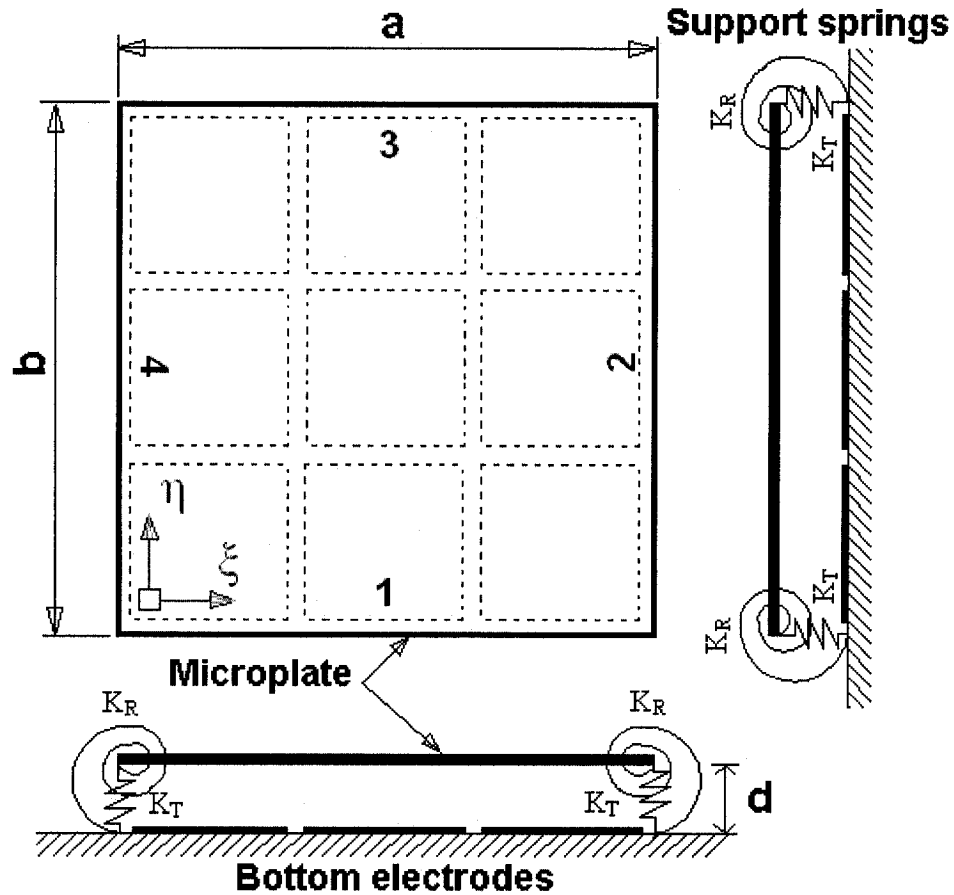


Fig. 3. 1. The microplate supported by artificial springs on edges with multiple electrodes underneath

Table 3. 1. Geometry and parameters of the microplate model

Length, a (μm)	Width, b (μm)	Thickness, t (μm)	Dielectric Gap, d (μm)	Young's Modulus E (GPa)	Poisson's Ratio, γ	Density, ρ (kg/m^3)
600	600	2	12	129.5	0.22	2320

3.2.2 Static Analysis

Boundary characteristic orthogonal polynomials, which were generated by Gram Schmidt orthogonalization process as proposed by [Bhat R B, 1985], were linearly combined to define the static flexural deflection of the microplates as,

$$W(x, y) = \sum_m^I \sum_n^J A_{mn}^S \phi_m(x) \varphi_n(y) \quad (3.1)$$

where, $x = \frac{\xi}{a}$ and $y = \frac{\eta}{b}$, ξ and η are coordinates of the plate, a and b are dimensions of the plate with $\alpha = a/b$. Terms $\phi_m(x)$ and $\varphi_n(y)$ are the boundary characteristic orthogonal polynomials in x and y directions and A_{mn}^S are arbitrary static deflection coefficients. I and J are the total number of orthogonal polynomials used assumed deflection shapes along x and y coordinates, respectively.

The total strain energy of the microplate includes the strain energy of the microplate due to bending (U_P), the potential energy of the support boundary springs (U_T and U_R), and energy due to the electrostatic field (U_E) as follows:

$$U_{TOTAL} = U_P + \sum_{S=1}^4 U_{T,S} + \sum_{S=1}^4 U_{R,S} + U_E \quad (3.2)$$

where,

$$U_P = \frac{Dab}{2a^4} \int_0^1 \int_0^1 \left[(W''')^2 + \alpha^4 (\ddot{W})^2 + 2\nu\alpha^2 (W''\ddot{W}) + 2(1-\nu)\alpha^2 (\dot{W}')^2 \right] dx dy \quad (3.3)$$

The strain energy of the translational springs along the side 'S' is

$$U_{T,S} = \frac{1}{2} K_{T,S} \int_0^{l_S} W_S^2 dl_S \quad (3.4)$$

The strain energy of the rotational springs along the side 'S' is

$$U_{R,S} = \frac{1}{2} K_{R,S} \int_0^{l_S} (W_S')^2 dl_S \quad (3.5)$$

where, W_S is the deflection along the S^{th} side; W_S' is the slope along the S^{th} side; D is flexural rigidity of the plate; l_S is the length of the S^{th} side; $K_{T,S}$ is the translational spring stiffness per unit length along S^{th} side and $K_{R,S}$ is the rotational spring stiffness per unit length along S^{th} side.

The total electrostatic energy U_E is given by,

$$U_E = -\frac{1}{2} \epsilon_0 \epsilon_r ab \sum_{k=1}^N V_k^2 \int_{y_{2k-1}}^{y_{2k}} \int_{x_{2k-1}}^{x_{2k}} \frac{dxdy}{d - W(x,y)} \quad (3.6)$$

where, N is the total number of electrostatic actuators;

x_{2k} , x_{2k-1} , y_{2k} and y_{2k-1} —upper and lower limits of the k^{th} bottom electrode along x and y directions, respectively. They are non-dimensional variables between 0 and 1.

Nonlinear electrostatic energy terms in Eq. (3. 6) are expanded using Taylor series with respect to the initial position. Based on the small displacement assumption, the higher order terms can be neglected and the nonlinear electrostatic energy is expanded as:

$$U_E = -\frac{\varepsilon_0 \varepsilon_r ab}{2d} \sum_{k=1}^N V_k^2 \int_{y_{2k-1}}^{y_{2k}} \int_{x_{2k-1}}^{x_{2k}} \left[1 + \frac{W(x,y)}{d} + \left(\frac{W(x,y)}{d} \right)^2 \right] dx dy \quad (3. 7)$$

The static equilibrium deflection of the microplate can be obtained by the stationary condition, (i.e.) minimizing the Eq. (3. 2) with respect to A_{ij} as:

$$\begin{aligned} & \sum_m^I \sum_n^J \left[\Gamma_{mnij} + \Psi_{mnij} + \beta_1 \cdot \sum_{k=1}^N V_k^2 E_{kmi}^{00} F_{knj}^{00} \right] A_{mn}^S \\ & = \beta \cdot \sum_{k=1}^N V_k^2 \int_{y_{2k-1}}^{y_{2k}} \int_{x_{2k-1}}^{x_{2k}} \phi_i(x) \phi_j(y) dx dy \end{aligned} \quad (3. 8)$$

$$i = 1, 2, \dots, I \quad \text{and} \quad j = 1, 2, \dots, J$$

where,

$$\begin{aligned} \Gamma_{mnij} = & E_{mi}^{22} F_{nj}^{00} + \alpha^4 \cdot E_{mi}^{00} F_{nj}^{22} + \\ & \nu \alpha \cdot (E_{mi}^{02} F_{nj}^{20} + E_{mi}^{20} F_{nj}^{02}) + 2(1-\nu) \alpha^2 \cdot E_{mi}^{11} F_{nj}^{11} \end{aligned}$$

$$\begin{aligned} \Psi_{mnij} = & K_{T,1}^* \alpha \cdot E_{mi}^{00} \varphi_n(0) \varphi_j(0) + K_{T,2}^* \cdot \phi_m(1) \phi_i(1) F_{nj}^{00} \\ & + K_{T,3}^* \alpha \cdot E_{mi}^{00} \varphi_n(1) \varphi_j(1) + K_{T,4}^* \cdot \phi_m(0) \phi_i(0) F_{nj}^{00} \\ & + K_{R,1}^* \alpha^3 \cdot E_{mi}^{00} \varphi_n'(0) \varphi_j'(0) + K_{R,2}^* \cdot \phi_m'(1) \phi_i'(1) F_{nj}^{00} \\ & + K_{R,3}^* \alpha^3 \cdot E_{mi}^{00} \varphi_n'(1) \varphi_j'(1) + K_{R,4}^* \cdot \phi_m'(0) \phi_i'(0) F_{nj}^{00} \end{aligned}$$

$$E_{mi}^{rs} = \int_0^1 \left(\frac{d^r \phi_m}{dx^r} \right) \left(\frac{d^s \phi_i}{dx^s} \right) dx; \quad E_{kmi}^{rs} = \int_{x_{2k-1}}^{x_{2k}} \left(\frac{d^r \phi_m}{dx^r} \right) \left(\frac{d^s \phi_i}{dx^s} \right) dx$$

$$F_{nj}^{rs} = \int_0^1 \left(\frac{d^r \varphi_n}{dy^r} \right) \left(\frac{d^s \varphi_j}{dy^s} \right) dy; \quad F_{knj}^{rs} = \int_{y_{2k-1}}^{y_{2k}} \left(\frac{d^r \varphi_n}{dy^r} \right) \left(\frac{d^s \varphi_j}{dy^s} \right) dy$$

$$K_{T,S}^* = \frac{a^3 \cdot K_{T,S}}{D}; \quad K_{R,S}^* = \frac{a \cdot K_{R,S}}{D}; \quad \beta = \frac{\varepsilon_0 \varepsilon_r a^4}{2Dd^2}; \quad \beta_1 = -\frac{\varepsilon_0 \varepsilon_r a^4}{Dd^3}; \quad S=1, 2, 3, 4$$

3.2.3 Static Influence Functions and Shape Optimization

As the linearity assumption provides results that are satisfactory for initial design, we use the same technique and try to combine the deflections that are caused by each of the bottom electrodes to reform the modulation shape of the whole microplate within the clamped-clamped boundary conditions. Let $C_k(x,y)$ be the influence function of microplate due to the k^{th} actuator, which represents the deflection of the microplate due to the k^{th} actuator under unit voltage.

$$W(x,y) = \sum_{k=1}^N C_k(x,y) U_k(V) \quad (3.9)$$

where, $U_k(V) = V_k^2$

Let $\psi(x,y)$ be the desired shape of the microplate. The discrete form of residual error between the actual deflection $W(x,y)$ and the desired deflection $\psi(x,y)$, is taken as the error function defined as follows:

$$E = \sum_{i=1}^M \left[\sum_{k=1}^N C_k(x_i, y_i) U_k(V) - \psi(x_i, y_i) \right]^2 \quad (3.10)$$

where, M is the total number of the nodal points selected for error minimization, which can be any point on the microplate and $C_k(x_i, y_i)$ is the influence function at the point $p(x_i, y_i)$ due to unit voltage at the k^{th} actuator. $C_k(x_i, y_i)$ is defined as C_{kp} hereafter. Minimizing E using the least-square fitting method with respect to $U_g(V)$ yields:

$$\sum_{p=1}^M \left[\sum_{k=1}^N C_{kp} C_{gp} U_k(V) - \psi_p C_{gp} \right] = 0 \quad (3.11)$$

Rewriting Eq. (3.11) in matrix format:

$$\sum_{p=1}^M C_p U = \sum_{p=1}^M \Phi_p \quad (3.12)$$

where, $C_p = C_{kp} C_{gp}$ and $\Phi_p = \psi_p C_{gp}$, $g = 1, 2, \dots, N$

Define the following relationship,

$$\tilde{\psi} = [\psi(x_1, y_1), \psi(x_2, y_2), \dots, \psi(x_M, y_M)]$$

$$\tilde{C}_n = [C_{n1}, C_{n2}, \dots, C_{nM}]^T, \quad n = 1, 2, \dots, N$$

$$R = [\tilde{C}_1, \tilde{C}_2, \dots, \tilde{C}_N]$$

and substitute into Eq. (3.12). The same relation can be achieved as in Chapter 2, which is used to optimize the applied voltages for each of the electrostatic actuators in the show case hereafter.

$$U = (R^T R)^{-1} R^T \tilde{\psi}^T \quad (3.13)$$

3.2.4 Dynamic Analysis

For the dynamic behavior of the microplate, the contribution of the kinetic energy must be taken into account. Softening of the electrostatic stiffness must also be calculated in order to represent the influence of electrostatic field that was generated by each of the electrostatic actuators.

As before, the dynamic flexural deflection W_D of the microplate is defined as Eq. (3. 1), so that each function of W_D satisfies the essential boundary conditions.

$$W_D(x, y) = \sum_m^I \sum_n^J A_{mn}^D \phi_m(x) \varphi_n(y) \quad (3. 14)$$

The kinetic energy of the micromachined plate is given by,

$$T_{\max} = \frac{1}{2} \rho a b t \omega^2 \int_0^1 \int_0^1 [W_D(x, y)]^2 dx dy \quad (3. 15)$$

where, t is the thickness, ρ is the density and ω is the frequency.

The electrostatic stiffness of each actuator is estimated at the static equilibrium condition.

Thus, the potential energy of electrostatic actuators is represented as,

$$U_{D,E} = \sum_{k=1}^N U_{D,Ek} = \sum_{k=1}^N \frac{1}{2} \int_{y_{2k-1}}^{y_{2k}} \int_{x_{2k-1}}^{x_{2k}} K_{Ek} [W_D(x, y)]^2 dx dy \quad (3. 16)$$

where, $K_{Ek} = -\frac{\varepsilon_0 \varepsilon_r a b V_k^2}{[d - W(x, y)]^3}$, referring to Eq. (2. 25).

$W(x,y)$ is the static equilibrium position at the optimized voltage condition. The coefficients of the dynamic flexural deflection A_{ij}^D are chosen so as to minimize the Rayleigh quotient R of W_D as

$$\frac{\partial U_{MAX}}{\partial A_{ij}^D} - R_{ij} \frac{\partial (T_{max} / \omega^2)}{\partial A_{ij}^D} = 0 \quad (3.17)$$

$$i = 1, 2, \dots, I \quad \text{and} \quad j = 1, 2, \dots, J$$

U_{MAX} is the maximum strain energy corresponding to the dynamic deflections with reference to the static equilibrium position.

$$U_{MAX} = U_{D,P} + \sum_{S=1}^4 U_{D,T,S} + \sum_{S=1}^4 U_{D,R,S} + U_{D,E} \quad (3.18)$$

The Eq. (3.17) constitutes a set of $I \times J$ homogeneous equations in A_{ij}^D . It has $I \times J$ roots, which are the upper-bound approximations to the natural frequencies as $R_{ij} \geq \omega_{ij}^2$. After simplification, Eq. (3.17) for U_{MAX}^D and T_{MAX} , yields:

$$\sum_m^I \sum_n^J \left[\left(\Gamma_{mnij} + \Psi_{mnij} + \beta_2 \cdot \sum_{k=1}^N V_k^2 G_{kmnij}^{00} \right) - \lambda_{ij}^2 E_{mi}^{00} F_{nj}^{00} \right] A_{mn}^D = 0 \quad (3.19)$$

where, Γ_{mnij} and Ψ_{mnij} are estimated referring to Eq. (3.8).

$$G_{kmnij}^{00} = \int_{y_{2k-1}}^{y_{2k}} \int_{x_{2k-1}}^{x_{2k}} \frac{\phi_m(x) \varphi_n(y) \phi_i(x) \varphi_j(y)}{[d - W(x,y)]^3} dx dy$$

$$E_{mi}^{rs} = \int_0^1 \left(\frac{d^r \phi_m}{dx^r} \right) \left(\frac{d^s \phi_i}{dx^s} \right) dx \quad \text{and} \quad F_{nj}^{rs} = \int_0^1 \left(\frac{d^r \varphi_n}{dy^r} \right) \left(\frac{d^s \varphi_j}{dy^s} \right) dy$$

$$\beta_2 = -\frac{\varepsilon_0 \varepsilon_r a^4}{D} \text{ and } \lambda_{ij}^2 = \frac{\omega_{ij}^2 \rho t a^4}{D}$$

Therefore, natural frequencies of the structure are given as,

$$\omega_{ij} = \lambda_{ij} \sqrt{\frac{D}{\rho t a^4}} \quad (3.20)$$

where λ_{ij} are called eigenvalues. $i = 1, 2, \dots, I$ and $j = 1, 2, \dots, J$

3.3 Validation of the Method

In order to verify the numerical method, different boundary configurations were modeled and compared with published results. The configurations along with support boundary conditions modeled with artificial springs are given in Table 3.2. In the present study, the clamped edge is modeled with very high values of translational and rotational stiffnesses. Both $K_{TS}^* = K_{RS}^* = K = 1 \times 10^{10}$, $S = 1$ to 4. The simply supported edge is modeled with $K_{TS}^* = K$ and $K_{RS}^* = 0$. The free edge has no stiffness $K_{TS}^* = K_{RS}^* = 0$. The nominal stiffnesses for microfabricated boundaries lay in between the clamped and simply supported condition depending upon the microfabrication processes.

The different boundary conditions and the corresponding stiffness values of artificial support spring are listed in Table 3.2: (i) all edges are simply supported (SSSS); (ii) all edges are clamped (CCCC); (iii) two parallel edges are simply supported and two sides are free (SFSF); (iv) two parallel edges are clamped and two sides are free (CFCF); (v) one end clamped cantilever plate (CFFF). The computed eigenvalues for above boundary conditions are compared with published results in Table 3. 3 to Table 3. 7.

Table 3. 2. Boundary configurations for square microplate

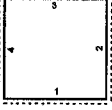
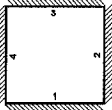
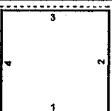
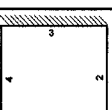
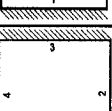
Boundary Configuration	$K=1 \times 10^{10}$ (N/m ²)	side 1		side 2		side 3		side 4	
		K_{T1}^*	K_{R1}^*	K_{T2}^*	K_{R2}^*	K_{T3}^*	K_{R3}^*	K_{T4}^*	K_{R4}^*
SSSS		K	0	K	0	K	0	K	0
CCCC		K	K	K	K	K	K	K	K
SFSF		K	0	0	0	K	0	0	0
CFCF		K	K	0	0	K	K	0	0
CFFF		K	K	0	0	0	0	0	0

Table 3. 3. Comparison eigenvalues for SSSS boundary condition

Mode No.	Ref. [Leissa W, 1969]	Present Prediction
		λ
1(1,1)	19.739	19.739
2(1,2)	48.348	49.348
3(2,1)	48.348	49.348
4(2,2)	78.957	78.957
5(1,3)	98.696	98.716
6(3,1)	99.696	98.716

Table 3. 4. Comparison eigenvalues for CCCC boundary condition

Mode No.	Beam Functions Method [Leissa A W, 1973]	S.S. Plate Functions Method [Dickinson S M and Li E K H, 1982]	Series Method [Claassen R W and Thorne C J, 1960]	Present Prediction λ
1(1,1)	35.992	35.988	35.985	35.986
2(1,2)	73.413	73.406	73.394	73.395
3(2,1)	73.413	73.406	73.393	73.395
4(2,2)	108.27	108.25	108.216	108.218
5(1,3)	131.64	131.62	131.581	131.779
6(3,1)	132.24	132.23	132.205	132.410

Table 3. 5. Comparison eigenvalues for SFSF boundary condition

Mode No.	Ref. [Fletcher H J et al., 1956]	Ref. [Jankovic V, 1964]	Present Prediction λ
1	9.63	9.87	9.631
2	16.13	16.13	16.134
3	36.72	36.71	36.725
4	38.94	39.48	38.944
5	46.74	46.73	46.738
6	70.75	70.73	70.740

Table 3. 6. Comparison eigenvalues for CFCF boundary condition

Mode No.	Series Method [Claassen R W and Thorne C J, 1960]	Present Prediction λ
1	22.17	22.178
2	26.4	26.426
3	43.6	43.609
4	61.2	61.192
5	67.2	67.205
6	79.8	79.826
7	87.5	87.621
8	120.1	120.372

Table 3. 7. Frequency parameters for CFFF square plate

Mode No.	Deflection Functions Method [Bazley N W et al., 1965] (Symmetric modes)	Admissible Functions Method [Sigi Lito V G, 1965] (Symmetric modes)	Series Method [Claassen R W and Thorne C J, 1962]	Present Prediction λ
1	3.482	3.473	3.472	3.472
2	----	----	8.55	8.509
3	21.367	21.304	21.29	21.290
4	27.278	27.291	27.2	27.199
5	----	----	31.1	30.964
6	54.301	54.262	54.3	54.197
7	61.405	61.276	61.3	61.263
8	----	----	64.2	64.143
9	----	----	71.1	70.985

The above comparisons validate the present model for the condition without electrostatic forces applied for various boundary conditions. But the current model could be extended for any non-classical boundary conditions resulting from micromachining by defining the appropriate values for K_T^* and K_R^* . The proposed model is applied to certain electrode configuration in the next section.

3.4 Application to a 3x3 -Electrode Microplate

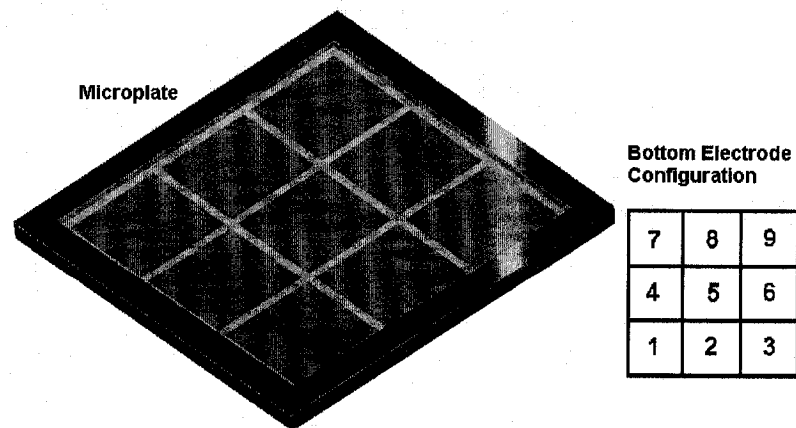


Fig. 3. 2. 3D Geometry of microplate and configuration of bottom electrodes

The proposed method is demonstrated for the case of a 3×3 -bottom electrodes. To simplify the discussion, the boundary conditions are assumed to be clamped at all edges. The voltage is applied on selected electrodes. In this case, a bias voltage of 100 V is applied to the electrodes 3 and 7 ($V_3=V_7=100$ V) while no voltage is applied on all other electrodes. The static deflection $W(x,y)$ with respect to the above applied voltages is shown in Fig. 3. 3, Fig. 3. 4 and Fig. 3. 5 are the other cases when different combinations of electrodes are biased. It is very clear that the deflection shape of the microplate can be changed by applying different voltages on different configurations of electrodes. The next step is to manipulate the deflection shape of the microplate through electrostatic actuation in order to obtain required deflection shapes.

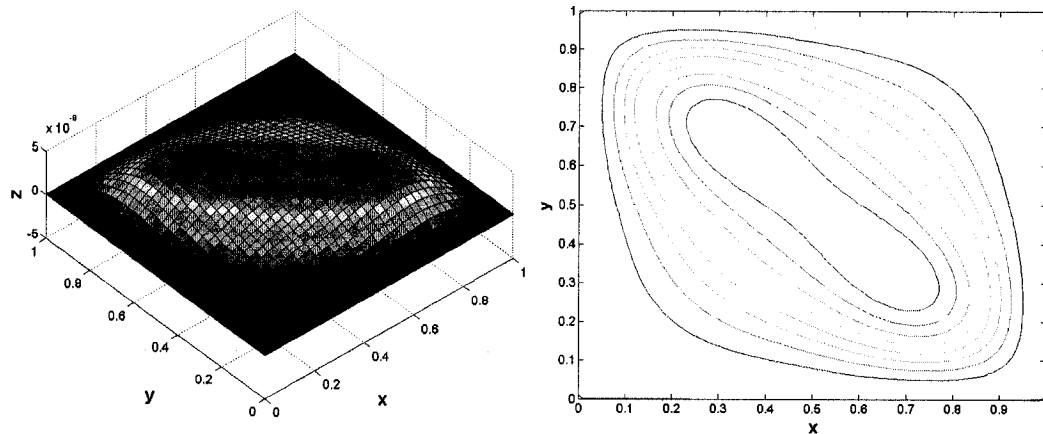


Fig. 3. 3. The static deflection of the microplate at $V_3=V_7=100$ V

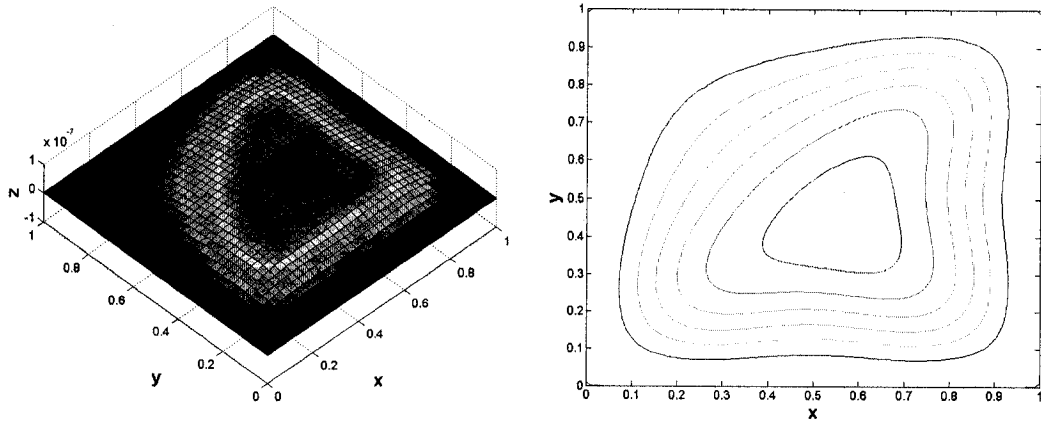


Fig. 3. 4. The static deflection of the microplate at $V_1=V_3=V_9=100$ V

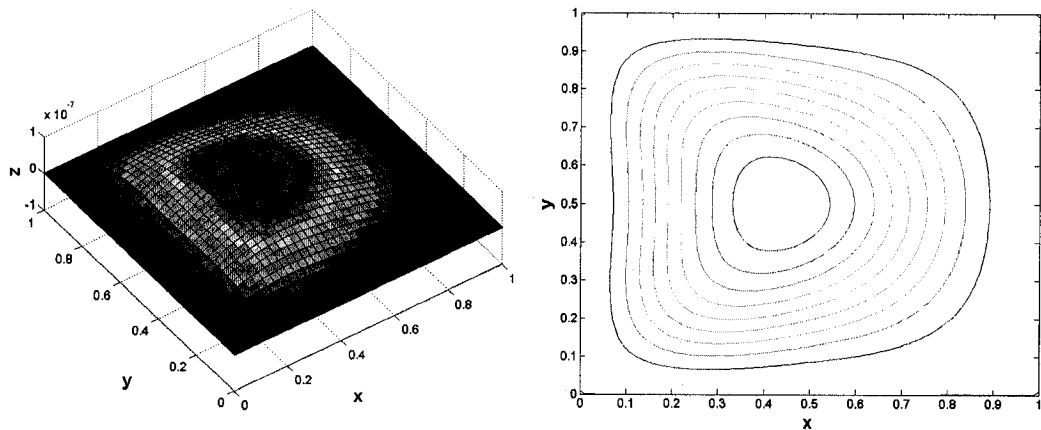
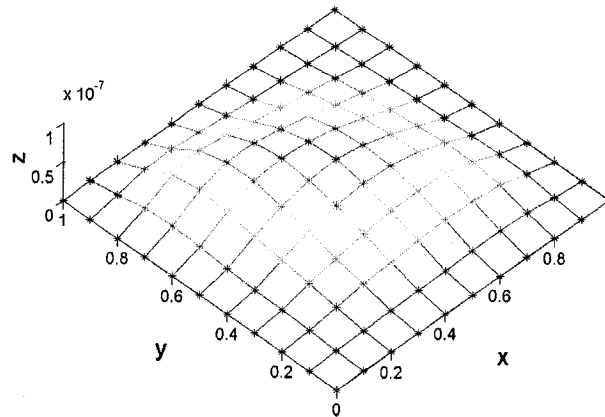


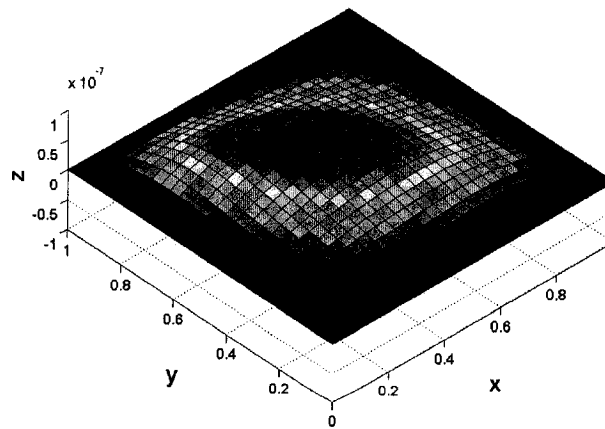
Fig. 3. 5. The static deflection of the microplate at $V_1=100$ V, $V_5=50$ V, $V_7=100$ V

The desired deflection can be in the form of measured values or a shape defined by a set of design points. The method is applied using the deflection known at every nodal points (x_i, y_i) . The sample selected points are given in Table 3. 8 and also shown in Fig. 3. 6(a). The voltages for the electrodes were optimized using Eq. (3. 13) and the deflection shape was achieved from Eq. (3. 8). The optimized voltages are given in Table 3. 9. At the same

time, the predicted deflection shape generated by the optimized voltages is shown in Fig. 3. 6(b). The discrepancy between desired and optimized deflection shapes was estimated and found to be very low as shown in Table 3. 10. In most of the cases, the deviation between the desired shape and optimized shape was less than 2%. This means that the desired deflection can be generated with reasonable accuracy.



(a)



(b)

Fig. 3. 6. Comparison of the desired deflection and the optimized deflection: (a) The mesh of the desired deflection at nodal points; (b) The deflection generated with the optimized voltages

Table 3. 8. Desired deflection at the nodal points of the microplate (m)

	x=0.0	x=0.1	x=0.2	x=0.3	x=0.4	x=0.5	x=0.6	x=0.7	x=0.8	x=0.9	x=1.0
y=0.0	0	0	0	0	0	0	0	0	0	0	0
y=0.1	0	1.13 e-09	3.18 e-09	4.90 e-09	6.00 e-09	7.30 e-09	8.80 e-09	1.00 e-08	8.70 e-09	4.10 e-09	0
y=0.2	0	3.22 e-09	9.10 e-09	1.44 e-08	1.83 e-08	2.20 e-08	2.43 e-08	2.47 e-08	2.00 e-08	8.70 e-09	0
y=0.3	0	5.09 e-09	1.49 e-08	2.30 e-08	3.00 e-08	3.60 e-08	3.70 e-08	3.40 e-08	2.47 e-08	1.00 e-08	0
y=0.4	0	6.68 e-09	2.10 e-08	3.38 e-08	4.30 e-08	4.70 e-08	4.50 e-08	3.73 e-08	2.50 e-08	8.90 e-09	0
y=0.5	0	9.50 e-09	2.71 e-08	4.20 e-08	5.00 e-08	5.27 e-08	4.70 e-08	3.60 e-08	2.15 e-08	7.30 e-09	0
y=0.6	0	1.33 e-08	3.40 e-08	4.94 e-08	5.45 e-08	5.10 e-08	4.31 e-08	3.15 e-08	1.80 e-08	6.00 e-09	0
y=0.7	0	1.60 e-08	3.88 e-08	4.90 e-08	5.00 e-08	4.27 e-08	3.40 e-08	2.44 e-08	1.44 e-08	4.90 e-09	0
y=0.8	0	1.52 e-08	3.30 e-08	3.87 e-08	3.46 e-08	2.70 e-08	2.04 e-08	1.50 e-08	9.20 e-09	3.10 e-09	0
y=0.9	0	7.20 e-09	1.52 e-08	1.65 e-08	1.30 e-08	9.49 e-09	6.80 e-09	5.10 e-09	3.27 e-09	1.13 e-09	0
y=1.0	0	0	0	0	0	0	0	0	0	0	0

Table 3. 9. The optimized voltages for the electrodes

Electrode	1	2	3	4	5	6	7	8	9
Voltage(V)	32.53	2.65	73.53	2.00	25.81	7.94	99.65	9.27	31.95

Table 3. 10. The error between desired and optimized deflection (%)

	x=0.0	x=0.1	x=0.2	x=0.3	x=0.4	x=0.5	x=0.6	x=0.7	x=0.8	x=0.9	x=1.0
y=0.0	~~	~~	~~	~~	~~	~~	~~	~~	~~	~~	~~
y=0.1	~~	3.28	2.18	2.48	0.21	0.04	1.63	0.53	1.03	0.73	~~
y=0.2	~~	0.89	0.60	1.12	0.66	2.07	0.34	0.77	0.00	1.18	~~
y=0.3	~~	1.59	0.96	5.10	4.42	0.35	1.03	1.07	1.07	1.03	~~
y=0.4	~~	1.14	3.21	0.53	0.10	0.18	0.29	0.62	1.74	1.54	~~
y=0.5	~~	0.41	0.12	1.29	2.80	0.06	0.24	0.49	1.47	1.61	~~
y=0.6	~~	0.21	1.67	0.09	0.02	1.21	0.51	0.68	2.58	1.61	~~
y=0.7	~~	2.80	0.08	1.72	0.91	0.47	0.15	0.58	0.38	1.20	~~
y=0.8	~~	0.36	0.45	0.45	0.62	1.53	1.34	0.02	0.56	0.65	~~
y=0.9	~~	1.59	0.22	0.12	3.53	1.41	1.51	0.11	1.89	4.27	~~
y=1.0	~~	~~	~~	~~	~~	~~	~~	~~	~~	~~	~~

Predictions of dynamic behaviour of the microplate subjected to bias voltages are analyzed in this section. The fundamental natural frequency and mode shape of the system mainly depend upon the material properties, geometry and support boundary conditions. One of the most outstanding problems in microfabricated systems is the nonhomogeneous boundary conditions of the microcomponents. Therefore, the artificial translational and rotational springs are used to model the non-classical boundary conditions. In order to demonstrate the predictions of dynamic behaviour under various support boundary conditions, three boundary conditions are considered, namely, SSSS, CCCC and a microfabricated condition which locates somewhere in between clamped and pinned. The selected microfabricated boundary condition which is modelled with $K_T^*=1 \times 10^{10}$ and $K_R^*=300$ at all edges. The predicted natural frequencies for the above three boundary conditions are given in Table 3. 11 at the optimized voltage configuration as shown in Table 3. 9.

Table 3. 11. The natural frequencies of the structure for different boundary conditions at optimized voltage configuration

Mode No.	Natural Frequencies	Natural	Natural Frequencies
	SSSS (kHz)	Frequencies CCCC (kHz)	$K_T^*=1 \times 10^{10}$ and $K_R^*=300$ at all edges (kHz)
1	38.281	70.224	69.312
2	96.142	143.33	141.49
3	96.409	143.44	141.61
4	154.11	211.41	208.73
5	192.83	257.6	254.3
6	192.95	258.74	255.42
7	250.64	322.71	318.62
8	250.81	322.84	318.74
9	328.35	413.82	408.43

3.5 Summary

In this chapter, boundary characteristic orthogonal polynomials are used in the Rayleigh Ritz method to model the microplate structures subjected to multiple electrostatic actuators. The non-classical boundary condition of the microstructures was modeled and quantified through artificial translational and rotational springs which would help model the non-classical boundary conditions resulting from various microfabrication processes. Based on this method, influence functions were created and optimal bias voltages were estimated in order to obtain the desired 3D deflection shape of a microplate.

The electromechanical coupling was taken into account in the Rayleigh Ritz method. The results under different sets of bias voltages will be further verified against ANSYS simulation based on Reduced Order Modeling (ROM) method in the next chapter. Further, the method proposed in this chapter can be easily extended for complicated geometries. The different geometry of the microstructures, locations, shapes and gaps of electrostatic actuators can be conveniently modeled using this method. It is very useful for applications in AO devices, dealing with predictions of both static and dynamic characteristics of deformable structures with high density of electrostatic actuators.

Chapter 4

4 Modeling Using Finite Element Method

4.1 Introduction

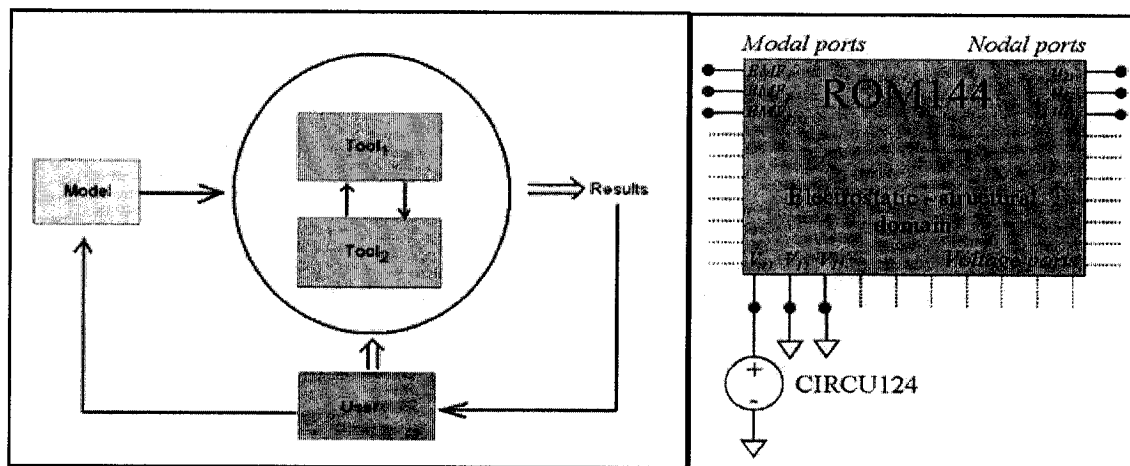
There are many difficulties in modeling MEMS devices due to strong coupling between the multiple energy domains as individual physical effects are governed by partial differential equations which are typically nonlinear. If finite element analysis is used on direct simulation mode for such kinds of problems, it is very cumbersome and time consuming. They cannot be simplified by a set of parameters for an equivalent model. Co-simulation is required in such kinds of problems [Bauer P and Van Duijssen P J, 2005]. If the model is highly nonlinear, an inter-process interface between tools is not available and the parameters cannot be exchanged, as shown in Fig. 4. 1(a). In such situation, Reduced Order Modeling (ROM) can be used. The goal of ROM method is to generate a fast and accurate description of coupled-physics systems that can model the response of the original problem. This method is based on a modal representation of coupled domains and can be viewed as an extension of the mode superposition method to nonlinear structural and couple-physics systems [Gabbay L D et al., 2000].

In this chapter, the ROM method will be used in ANSYS to simulate the strong nonlinear coupling between electrostatic forces and elasticity mechanics. The static deflections and dynamic responses of the microbridges and microplates will be compared with the results of proposed method in the last two sections.

4.2 Modeling Used ANSYS

The use of a general FEM simulation tool will allow to model complicated device and to understand the static and dynamic interactions between the parameters. A new method called Reduced Order Modeling (ROM) method, is an approximation method used in ANSYS for 2D and 3D models.

In ROM, a model can be constructed based on results from one tool to another and vice versa until reaching a new equilibrium condition. Although the size and complexity of the model is reduced, all relevant properties of the model are conserved with the reduced model. The ROM method does not require to set-up a new model in the second tool, because the reduced order model captures the model and its parameters. The only requirement is that the second tool should be able to include the ROM in its modeling environment. That's why an inter-process interface is necessary in ROM.



(a)

(b)

Fig. 4. 1. (a) Flow of Co-Simulation; (b) ROM144 element in ANSYS (adapted from ANSYS Help)

The reduced order model (ROM) is a suitable method to mathematically represent MEMS structures based on potential and kinetic energy representations of preset fundamental modes [Gabbay L D et al., 2000]. ROM144 element in ANSYS is used to simplify the reduced 2D or 3D model and develop the governing equations for predetermined master nodes. The element fully couples the electromechanical domains and represents a reduced order model suitable for use in finite element analysis as well as electromechanical circuit simulations, Fig. 4. 1(b).

There are four key steps required for creating and using ROM144 model as follows: (i) Model Preparation (ii) Generation Pass (iii) Use Pass and (iv) Expansion Pass. After creating the necessary finite element model in Model Preparation, a model analysis and an optional static analysis of the microstructure are executed in Generation Pass. Therefore, the deformation states of the microstructure under operating conditions are determined. Using this information, the Generation Pass selects the modes and performs computations to create a reduced order model, which is stored in a ROM database and utilized by ROM144 element. The Use Pass allows many types of analyses, such as transient, harmonic and static with various load situations. Finally, Expansion Pass allows detailed review of the stress and displacement in original FEA model. Sometimes, animations can also be created to visualize the dynamic response of the structures.

Among these four steps, Generation Pass, is very important. A test load is applied to the model to simulate the primary motion of the device. A modal analysis is then performed to compute the mode shapes. The user can then select the modes that will be used to build the device response surface through linear combination of these selected modes.

The reduced order elements have a fraction of nodes of the full model. Thus, it helps greatly reduce computational time [Bradley J K et al., 2005]. Although the ROM144 element is inherently less accurate, the computational savings allow a refined mesh, which enhances accuracy. Overall, the ROM144 model can calculate static, modal and harmonic solutions. The simulation can converge within reasonable computational time. It provides a significant advantage over the other models.

4.3 Simulating a Deformable Microbridge with Three Electrostatic Actuators

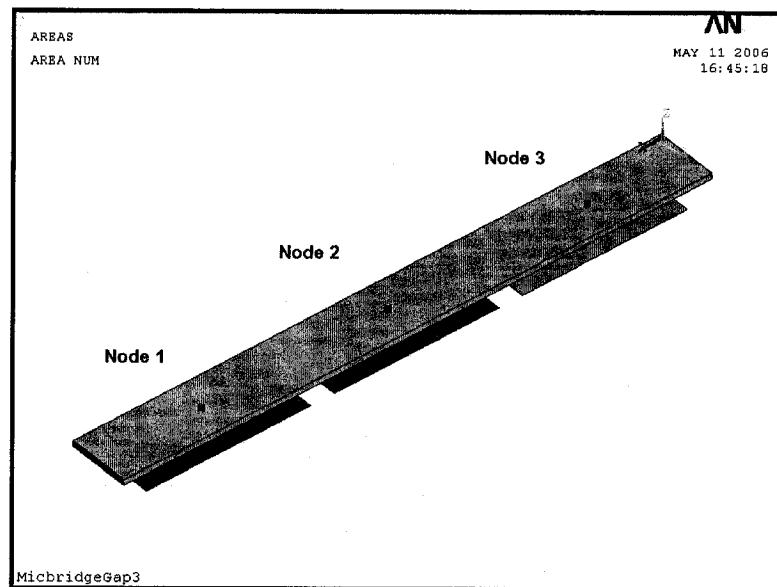


Fig. 4. 2. 3D solid model of the microbridge with three electrostatic actuators

In order to save computational time, the geometry of microbridge was scaled down to length of $100\mu\text{m}$ and width of $10\mu\text{m}$ as shown in Table 4. 1. The length of the electrostatic actuators is $28\mu\text{m}$ and the same width as the microbridge. The top suspended electrode was modeled by SOLID45 and SOLID122 element was used for

surrounding air. ROM144 element was generated from a 3D model, as in Fig. 4. 2, including the microbridge, fixed electrodes and air, which fully coupled the electromechanical domains. The master nodes were defined on the central axils of microbridge's top surface for the pass generation and used to create first one or two dominant modes.

Table 4. 1. The parameters of microplate model used in simulation

Size of Microbridge L×W (μm ²)	Size of Electrode a×b (μm ²)	Thickness t (μm)	Gap of Electrostatic Actuators d (μm)	Young's Modulus	Density
				E (GPa)	ρ (kg/m ³)
100×10	28×10	1	3	169	2329

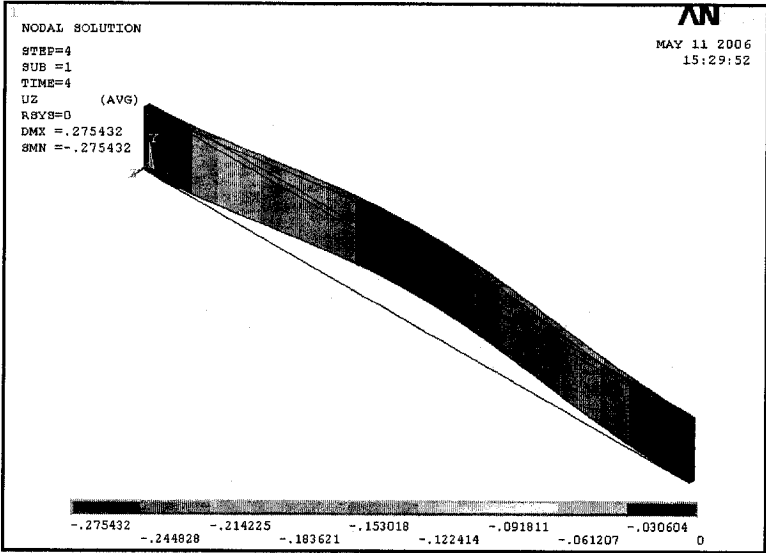


Fig. 4. 3. The static deflection of the microbridge (V1=300v, V2=50v, V3=150v)

The static deflection with $V_1=300$ V, $V_2=50$ V and $V_3=150$ V obtained using ANSYS is given in Fig. 4. 3. A voltage sweep was applied on electrode 1 and 2 respectively, starting from 0 volts up to pull-in voltage. The results were summarized and compared with energy method in Fig. 4. 4 and Fig. 4. 5. It is clear that the results of the proposed method agree very well with ANSYS, especially in small deflection region. The largest difference mainly locates at the node 2, which is the weakest part of the structure. The discrepancy will be enlarged with the bias voltage increasing near pull in. In near pull-in condition, the whole system becomes very unstable. Although using nonlinear method can achieve relatively better approximate results, it is hard to guarantee its accuracy. Taylor series was used in proposed method to linearize electrostatic force term based on the small deflection assumption which also causes the inaccuracy around pull-in status. Therefore, the agreement between results of energy method and ROM methods near pull-in condition are expected to be poor.

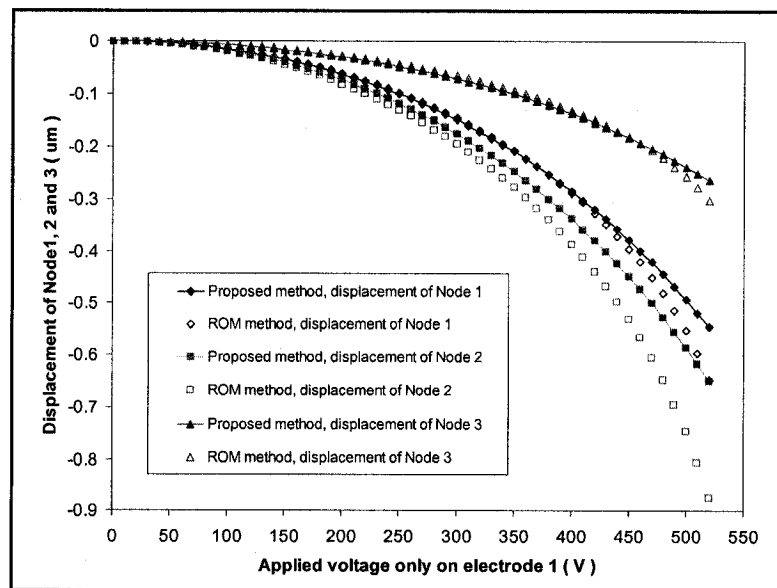


Fig. 4. 4. Comparison of node deflections when voltage was only applied at electrode 1

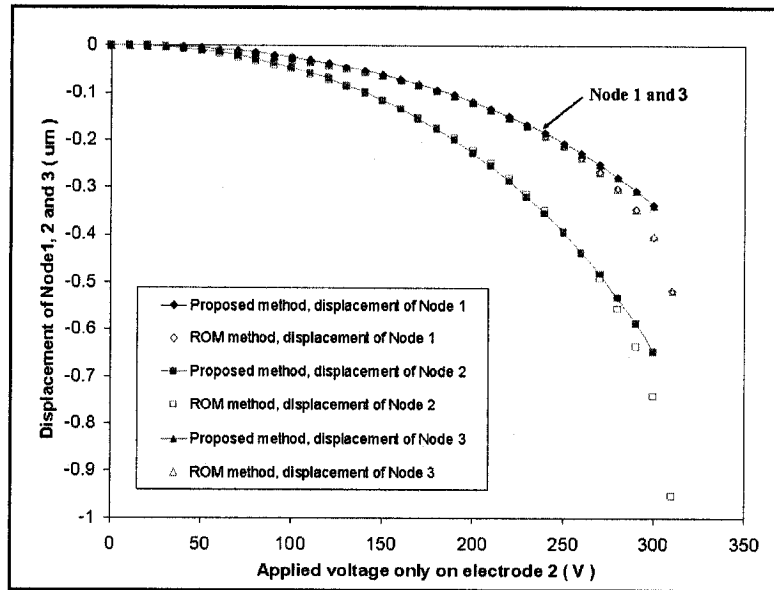


Fig. 4. 5. Comparison of node deflections when voltage was only applied at electrode 2

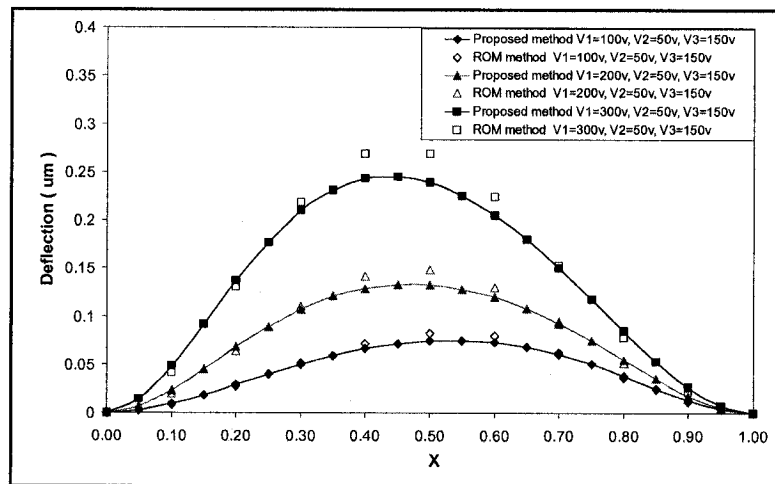


Fig. 4. 6. Comparison of deflection shapes under different applied voltages

The static deflections under different applied voltage combinations were also compared in the Fig. 4. 6. The applied voltages on the electrostatic actuators 2 and 3 were fixed and voltage on the first side electrode was changing form 100 V to 300 V. The discrepancies

between energy method and ROM method results were magnified for deflections. It is worth to mention that the polynomials of sixth order were used to represent the deflection shapes in ROM method. While, the number of orthogonal polynomials used in energy method is fourteen. That means the power order of polynomials for the deflection shape can be up to power thirteen. There is no doubt that the results achieved by proposed method can sophisticatedly describe the deformation. The other reason could be the fringe effect in ROM method.

In the harmonic analysis of ROM method, 1 volt AC driving voltage was used for searching the resonant frequencies. It is very clear to see the fundamental frequencies shifting to the right hand side, closer to zero, with the increase of applied voltage on the central electrostatic actuator, as shown in Fig. 4. 7. This phenomenon is called electrostatic softening effect. The stiffness of the microdevice is altered with the change of applied voltage. The second mode was activated accompanying with the first mode in Fig. 4. 8. The frequency of the second mode did not vary as obviously as the first one when the applied voltage was changed.

The results from ROM method and Rayleigh-Ritz method were compared in the Table 4. 2. The error was calculated based on the results of ROM methods. The difference of the first mode between these two methods is around 1.0%. Same phenomena were found around the pull-in condition, i.e. $V_2=300$ V, the error is around 2%.

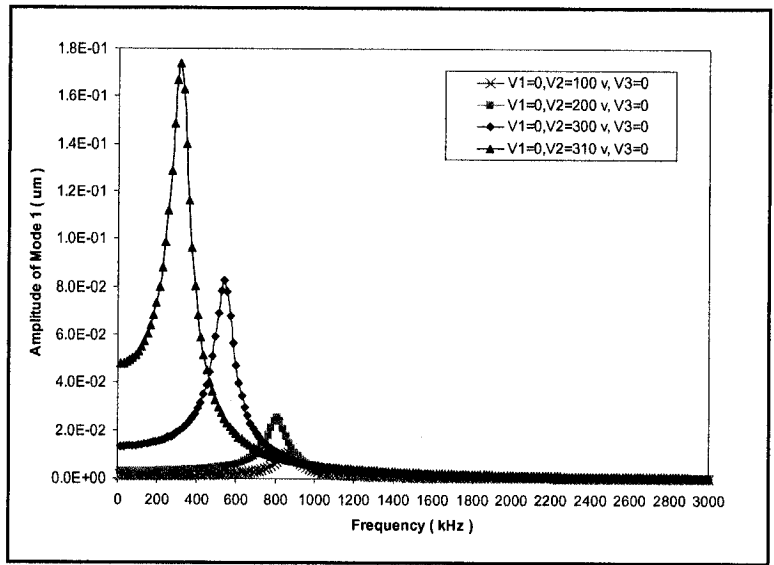


Fig. 4. 7. Shift of the resonant frequency of mode 1 under different applied voltages at the central electrostatic actuator

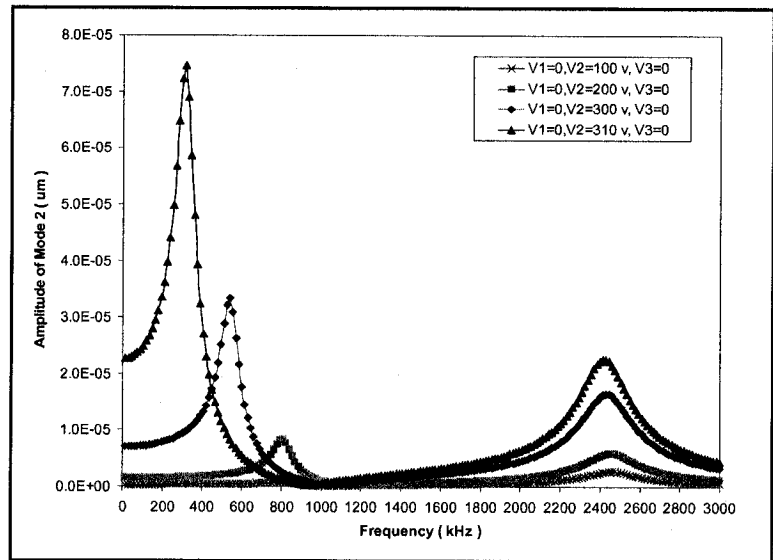


Fig. 4. 8. Shift of the resonant frequency of mode 2 under different applied voltages at the central electrostatic actuator

Table 4. 2. Comparison between Rayleigh-Ritz and Ansys (ROM) results

V_1 (V)	V_2 (V)	V_3 (V)	Mode 1 (kHz)		Error (%)	Mode 2 (kHz)		Error (%)
			ANSYS (ROM)	Rayleigh Ritz		ANSYS (ROM)	Rayleigh Ritz	
0	100	0	870.00	859.99	1.15	2460.00	2411.43	1.97
0	200	0	810.00	796.81	1.63	2460.00	2402.85	2.32
0	300	0	540.00	523.45	3.06	2430.00	2374.62	2.28
100	50	150	870.00	861.86	0.94	2445.00	2404.2	1.67
200	50	150	855.00	851.65	0.39	2445.00	2395.3	2.03
300	50	150	825.00	830.99	0.73	2430.00	2378.1	2.14
400	50	150	780.00	790.03	1.29	2385.00	2347.4	1.58

4.4 Simulating a Microplate with 2×2-Electrostatic Actuators

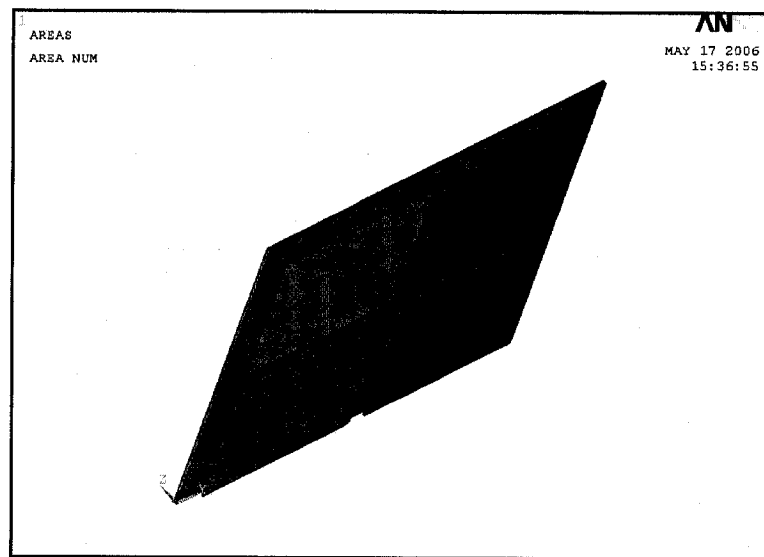


Fig. 4. 9. 3D solid model of the microplate with 2x2 electrostatic actuators arrays

Table 4. 3. The parameters of microplate model used in simulation

size of plate $a \times b$ (μm^2)	size of electrode $a' \times b'$ (μm^2)	thickness t (μm)	gap of electrostatic actuators d (μm)	young's modulus E (GPa)	density ρ (kg/m^3)
100×100	44×44	1	3	169	2329

The same method was also applied to simulate the static and dynamic behaviors of a microplate structure. The geometry of microbridge was also scaled down as shown in Table 4. 3 in order to reduce the computational time. ROM144 fully couples the electrostatic and structure domains. The element has ten modal degrees of freedom relating modal forces and modal displacements; ten voltage degrees of freedom relating electrical current and potential and optionally, ten master nodes relating nodal forces to nodal displacements. Nodes 11 to 20 in ROM144 are electrical conductor ports and they relate voltage (VOLT degree of freedom). That means only the first 5 ports can be included in the model, from node 11 to 15, and node 16 to 20 are the corresponding applied voltages on them. It is the main reason that a microplate with four electrostatic actuators was modeled in this section, as shown in Fig. 4. 9. The equilibrium position when electrostatic forces equal to elastic forces of the microplate is shown in the Fig. 4. 10. A static deflection in Fig. 4. 11 was created by Expansion Pass when applied voltages are $V_1=400$ V, $V_2=150$ V, $V_3=50$ V and $V_4=200$ V.

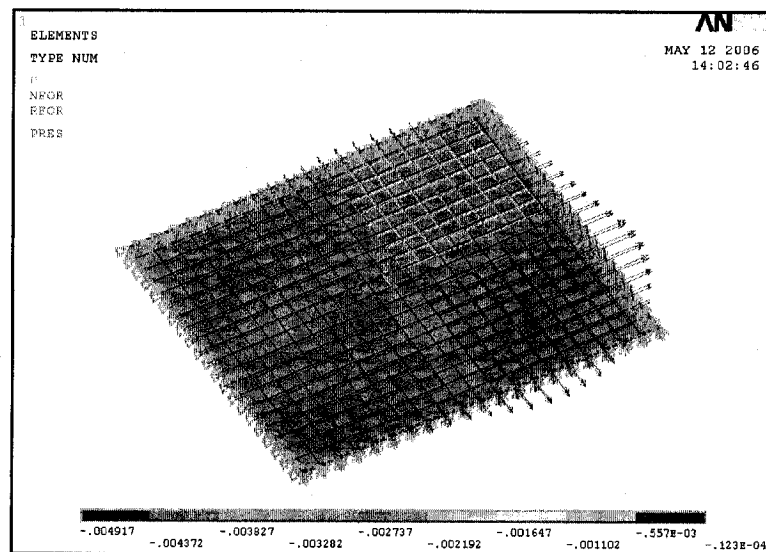


Fig. 4. 10. Electrostatic forces equilibrate with elastic forces of the microplate

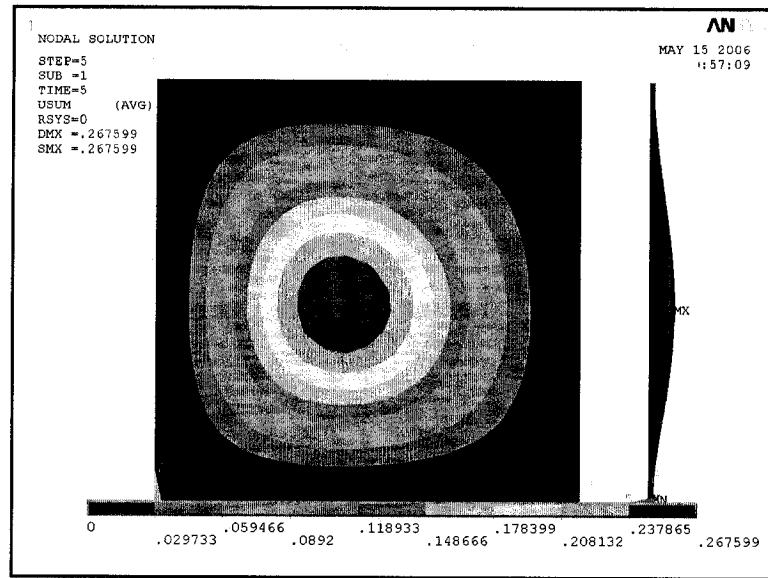


Fig. 4. 11. The static deflection of the microplate ($V_1=400$ V, $V_2=150$ V, $V_3=50$ V, $V_4=200$ V)

Ten orthogonal polynomials were used for x coordinate and another ten for y coordinate in the microplate model. Therefore, proposed method can describe the complex surface deflection in detail. The difference is obvious by comparing Fig. 4. 11 with Fig. 3. 3, Fig. 3. 4 and Fig. 3. 5. The displacements of some nodes on the neutral plate in the ANSYS model were used to compare with the prediction results, as shown in Fig. 4. 12 at different sections along x and y. Although they can agree generally with each other, the discrepancy is obvious in some parts. It needs further verification with experiments.

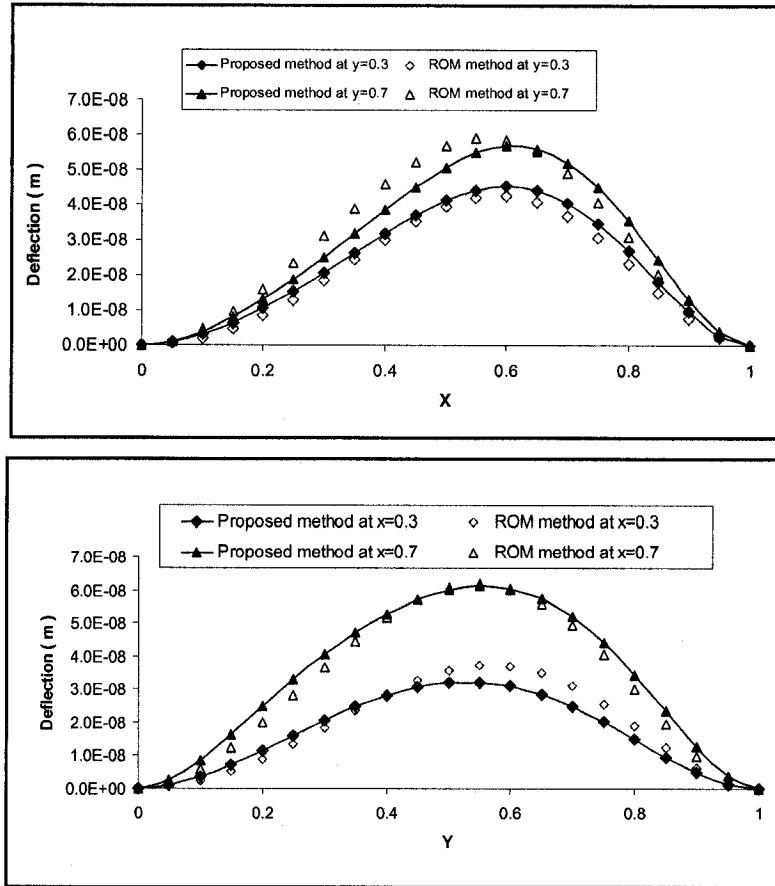


Fig. 4. 12. Comparison of deflection shapes at different sections along x and y, ($V_1=0$, $V_2=150$ V, $V_3=50$ V, $V_4=200$ V)

In the case of dynamic behavior, the accuracy of Rayleigh Ritz method degenerates progressively for the higher natural frequencies. But, using large number of orthogonal polynomials is a way to guarantee high accuracy for the first few eigenvalues and natural frequencies, as shown in Table 3. 3 to Table 3. 7. Since ROM method is also a simplified method, both size and complexity of the model are reduced in calculation which required refined mesh to enhance accuracy. Comparison of ROM and Rayleigh Ritz results of the first two modes are given at the first row in Table 4.4 when there is no voltage applied on electrodes. The Rayleigh Ritz method can achieve very good results as seen from the previous comparisons. Further it is also difficult for ROM method to figure out the small

discrepancies on dynamic response between two different cases as can be seen in row 6 and 7 in Table 4.4. The results of ROM method can be enhanced by increasing the order of polynomials in simulation but at the expense of computation time and only the first few dominant frequencies can be produced by ROM method. Nevertheless the ROM simulation results serve as a very good reference for comparing the capabilities and accuracy of the Rayleigh Ritz method used for modeling microdevices with multiple electrostatic actuators. Comparison of the results from Rayleigh Ritz and ROM methods in Table 4.4 show that the discrepancies are around 1.5% for the first mode and 3% for the second mode for different cases of bias voltage input.

Table 4. 4. Comparison the discrepancy of between Rayleigh Ritz and ROM results

V ₁ (V)	V ₂ (V)	V ₃ (V)	V ₄ (V)	Mode 1 (kHz)		Error (%)	Mode 2 (kHz)		Error (%)
				ANSYS (ROM)	Rayleigh Ritz		ANSYS (ROM)	Rayleigh Ritz	
0	0	0	0	1435.70	1411.44	1.69	2968.30	2878.73	3.02
200	0	0	0	1420.00	1401.23	1.32	2960.00	2868.59	3.09
400	0	0	0	1380.00	1362.12	1.30	2920.00	2832.55	2.99
600	0	0	0	1260.00	1237.76	1.77	2840.00	2741.02	3.49
0	150	50	200	1420.00	1394.66	1.78	2960.00	2867.74	3.12
200	150	50	200	1400.00	1383.75	1.16	2940.00	2857.15	2.82
200	0	0	300	1400.00	1375.72	1.73	2940.00	2843.84	3.27
500	0	0	300	1300.00	1286.41	1.05	2860.00	2766.69	3.26

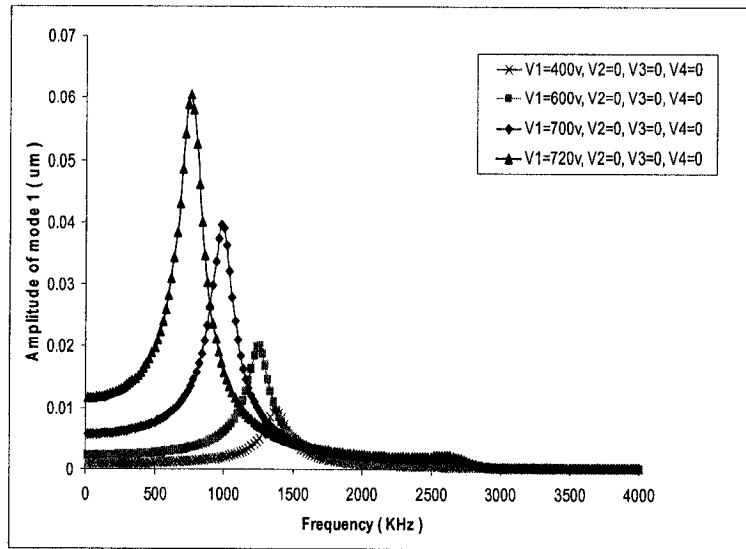


Fig. 4. 13. Shift of the resonant frequency of mode 1 under different applied voltages at electrostatic actuator 1

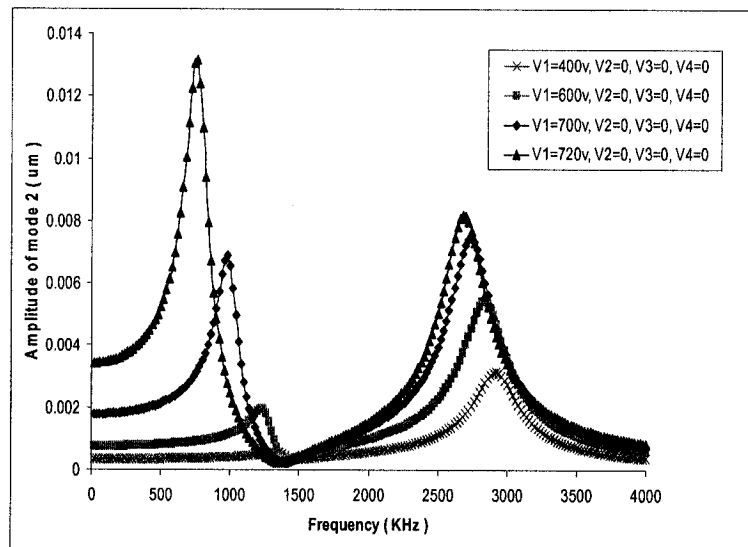


Fig. 4. 14. Shift of the resonant frequency of mode 2 under different applied voltages at electrostatic actuator 1

4.5 Summary

ROM method offers another simple and efficient way to solve mechanical and electrostatic coupling problems. Since ROM method is also a simplified method, both size and complexity of the model are reduced in calculation and too much emphasis on

the computation speed will lead to less precise results. From the above comparison, it is difficult for ROM simulation to produce sophisticated deflection shapes and higher natural frequencies. For the case having nonhomogeneous boundary conditions, extra techniques are needed for model building. The model has to be changed for different situations, such as geometry and boundary condition when using FEA. The advantage and benefit of generating pass will be lost. As non-linear method was used in ROM simulations; it can achieve better approximate prediction in the unstable region and near pull-in voltage when compared with Rayleigh Ritz method.

It is very safe to use proposed energy method to accurately predict static deflections of the microstructures up to around $2/3$ of the pull-in condition, based on the comparison of simulation results. For a deformable microstructure with multiple electrodes, accurately predicting deflection shapes will be of more concern than the pull-in situation. As large number orthogonal polynomials are used in calculation, Rayleigh Ritz method can give more accurate results in the first few natural frequencies when compared with ROM method. The different geometry of the microstructures, locations, shapes and gaps of electrostatic actuators can be conveniently modeled. Therefore, the proposed energy method is a very simple, efficient and accurate method to predict steady deflections and dynamic behaviors of MEMS structures with single or multiple electrostatic actuators.

The next chapter will discuss the microfabrication of microdevices, bridges and plates with multiple electrodes used for further verifying the proposed method by experiment.

Chapter 5

5 Design Layout, Microfabrication and Packaging

5.1 Introduction

The theoretical models of microbridges and micromirror plates were presented in the earlier chapters. Comparison between ANSYS simulation and proposed method was in close agreement in the last chapter. But it is very essential to validate the prediction method with experimental results. Hence, the fabrication of devices and building of the required experimental technique along with setup will be very important for further validation of the proposed model.

In order to test and validate, PolyMUMPs surface micromachining process [MUMPs Process, 2003] and Micragem SOI bulk micromachining process [CMC/SCM, 2005] are used to fabricate microbridges and micromirror plates with multiple electrostatic actuators. The support boundary conditions, geometries of the microstructures and electrodes are significant parameters that influence the stiffness of the structures. Different patterns of electrodes and distances between them can also be considered as main design parameters.

Multi-User MEMS Process (MUMPs) [MUMPs Process, 2003] and Micragem [CMC/SCM, 2005] are two main standardized commercial MEMS processes selected for microfabrication. Their general process description and design rules can be found in their user guide from MEMSCAP Inc. and MICRALYNE Inc.. Therefore, the process overview and the design layout of these two chips will only be briefly presented.

Wirebonding of these chips are finished in our lab, and the post processing of the devices are also discussed in this chapter.

5.2 PolyMUMPs

The cross section of PolyMUMPs surface micromachining process is shown in Fig. 5. 1. Three-layer polysilicon is used as structural material and the deposited oxide, Phospho Silicate Glass (PSG), is used as sacrificial layers and the silicon nitride layer is used for electrical isolation between polysilicon and the substrate. Therefore, the basic PolyMUMPs process incorporates seven layers as shown in Fig. 5. 1. The thicknesses of the structural and sacrificial layers are structured and cannot be modified.

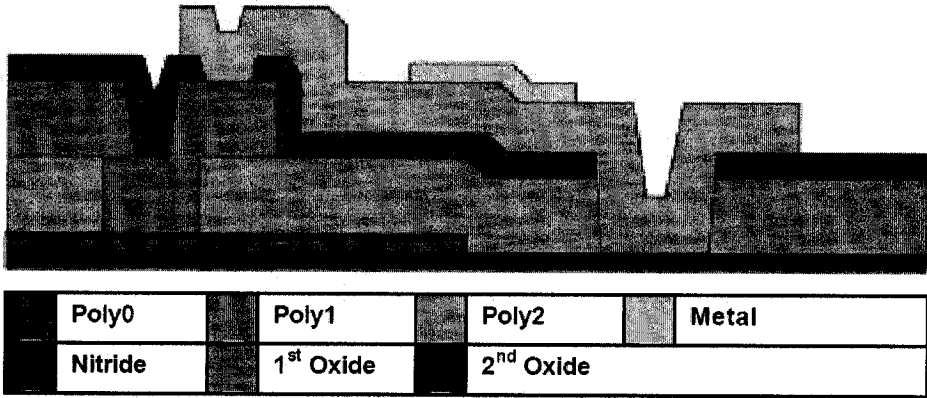


Fig. 5. 1. Cross-section view of 7-layer of PolyMUMPs process (adapted from MUMPs Process, 2003)

The process begins with n-type (100) silicon wafers of 1-2 Ω -cm resistivity. The surfaces of the wafers are first heavily doped with phosphorous in a standard diffusion furnace. This helps reduce or prevent the charge feed through to the substrate from electrostatic devices on the surface. Next, a 600 nm thick low stress silicon nitride layer

is deposited using LPCVD (low pressure chemical vapor deposition) on the wafers as an electrical isolation layer. Then, the first 500 nm polysilicon layer (Poly0) is directly deposited and patterned by photolithography. A 2.0 μm thick PSG sacrificial layer (Oxide1) is then deposited by LPCVD. This layer of PSG will be removed at the end of the process to free the first mechanical layer of polysilicon (Poly1). The sacrificial layer is lithographically patterned by Reactive Ion Etching (RIE).

The first structural layer of polysilicon (Poly1) is deposited on the sacrificial layer with a thickness of 2.0 μm . A thin layer of PSG is deposited over the polysilicon and annealed at 1050°C for 1 hour. Since the Poly1 layer is sandwiched by PSG layers and annealed at a high temperature, the net stress in Poly1 layer is significantly reduced. The top PSG layer also produces a hard mask for the subsequent polysilicon etch and then is removed by RIE. After Poly1 is patterned, a second PSG layer (Oxide2) is deposited which is patterned using two different etch masks with different objectives. The etch holes on the second Oxide are defined using RIE to provide Poly1-Poly2 contacts. This provides mechanical and electrical connection between two structural polysilicon layers. It is also possible to etch both Oxide layers so that Poly2 can contact with substrate, either Poly0 or silicon nitride layer.

The second structural layer (Poly2) is then deposited up to 1.5 μm thickness followed by the deposition of 200 nm PSG. As with Poly1, the PSG layer works as both an etch mask and dopant source for Poly2. Finally a 0.5 μm thick metal layer (Au) is deposited and patterned by lift-off method. The metal layer provides for probing, bonding, electrical routing and highly reflective mirror surfaces.

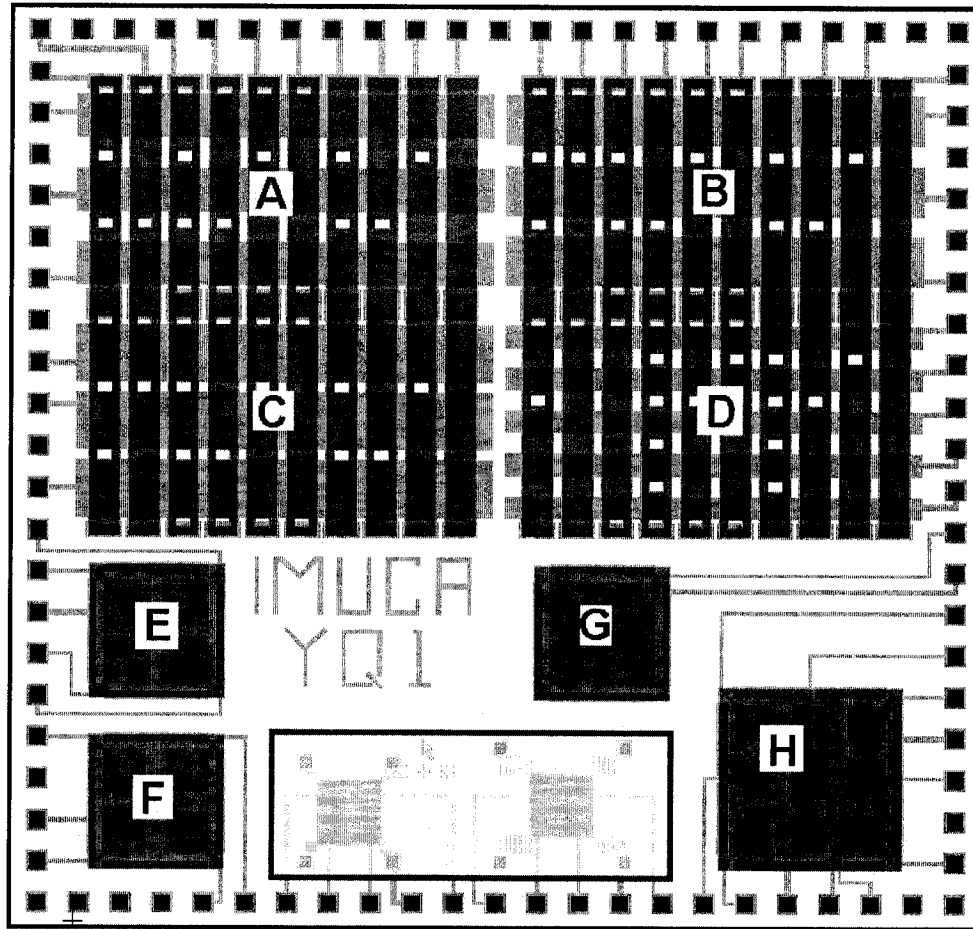










Fig. 5. 2. Layout of the PolyMUMPs design

In the present work, various types of microdevices with multiple electrodes were designed for PolyMUMPs process. The design layout consists of microbridges and rectangular micromirrors of various dimensions and different number of electrostatic actuators as shown in Fig. 5. 2. The corresponding geometry of the microstructures and patterns of electrodes are listed in the Table 5. 1. The design layout was created by L-Edit layout editor of *MEMS ProTM* software package. The released microstructures were clearly shown by the Scanning Electron Microscope (SEM) picture of the loose dices. A close-up top view of the microbridge array is shown in Fig. 5. 3. The anchors, gaps, side

etch holes of the microbridges can be clearly observed in the Fig. 5. 4. The top microstructures are Poly2 and metal layers and the bottom electrode layer is Poly0 layer. Since the layers were deposited one by one, the shapes of the early steps will translate to the final structures. The gaps between the bottom electrode layers (poly1) will produce ridges on the top suspending structures which causes the stiffness increase of the microstructures. The etch cutouts which are located in different places of the microstructures were used to change the structure stiffness so as to alter the static and dynamic response of the microdevices.

Table 5. 1. Definitions of microstructures on the PolyMUMPs chip

Region	Microstructure	Definitions
A		Microbridge array: L: 1000 μm , W: 150 μm , with 3 electrodes Width of electrode: 207 μm Gap between electrodes: 150 μm
B		Microbridge array: L: 1000 μm , W: 150 μm , with 3 electrodes Width of electrode: 240 μm Gap between electrodes: 100 μm
C		Microbridge array: L: 1000 μm , W: 150 μm , with 3 electrodes Width of electrode: 270 μm Gap between electrodes: 50 μm
D		Microbridge array: L: 1000 μm , W: 150 μm , with 5 electrodes Width of electrode: 100 μm Gap between electrodes: 100 μm
E		Microplate: L: 600 μm , W: 600 μm , with 2 \times 2 electrodes Electrode: 225 μm \times 225 μm Gap between electrodes: 50 μm
F		Microplate: 600 μm \times 600 μm , with 2 \times 2 electrodes Electrode: 200 μm \times 200 μm Gap between electrodes: 100 μm
G		Microplate: 600 μm \times 600 μm , with 1 electrodes Electrode: 500 μm \times 500 μm
H		Microplate: 800 μm \times 800 μm , with 3 \times 3 electrodes Electrode: 170 μm \times 170 μm Gap between electrodes: 100 μm

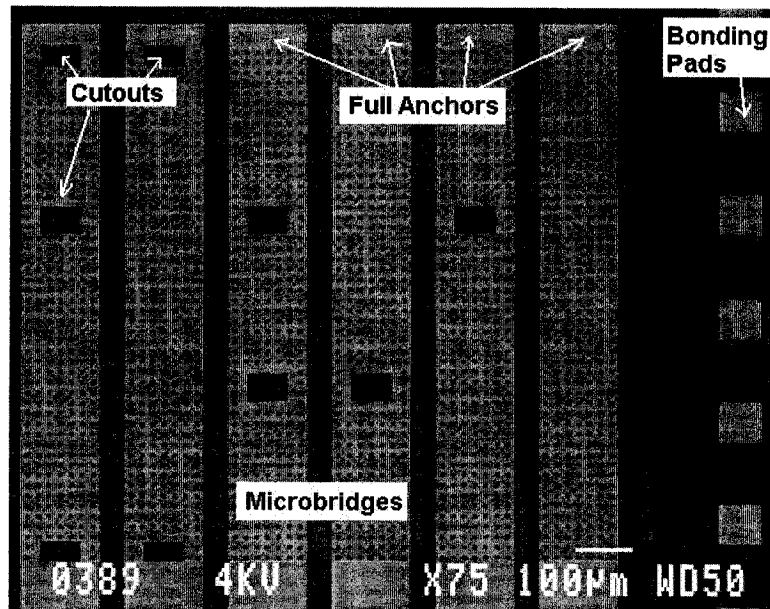


Fig. 5. 3. SEM picture of microbridge array

As part of the process, the surfaces of the microbridges and microplates have etch holes as shown in Fig. 5. 5. Etch holes increase the sacrificial undercutting rate so as to decrease the release time. However, due to the presence of etch holes on the surface, light diffraction and absorption would lead to the loss of optical signal. In addition to the holes, the maximum gap between the bottom electrode (poly0) and top suspending microstructures (poly2) is $2.75 \mu\text{m}$ which is a fixed value and decided by the thickness of the sacrificial oxide layers between Poly0 and Poly2. These two drawbacks become the greatest barrier for the application of PolyMUMPs process for MOEMS applications. Small gap and etch holes also create a challenge for out of plate motion applications.

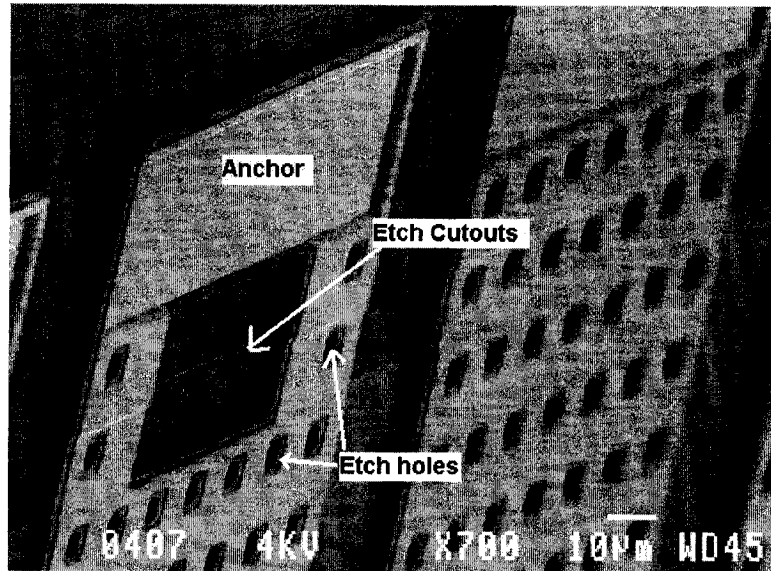


Fig. 5. 4. The boundary conditions and gap of microbridges fabricated through PolyMUMPs technology

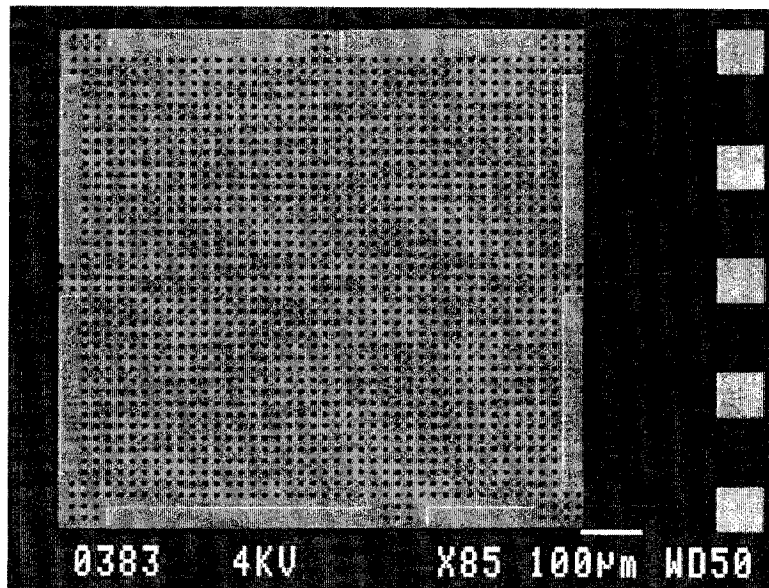


Fig. 5. 5. Top view of the microplate with 9 electrodes fabricated through PolyMUMPs technology

5.3 Micragem

Micragem SOI process [CMC/SCM, 2005] is a very new microfabrication procedure introduced by Micralyne Inc. and made available to researchers through CMC

Microsystems Corporation. Since the residual stress involved in SOI wafer is very low and etch holes are not the requirement, this fabrication process is very suitable for MOEMS and various other applications. Compared with PolyMUMPs, Micragem process enables the suspended MEMS devices using metal electrodes rather than polysilicon. Users can select two gap depths or combination of these to increase the gap value between the electrode layers. These advantages make Micragem process more versatile and flexible than other MEMS prototyping technologies. Fig. 5. 6 gives an overview of the Micragem prototyping process steps.

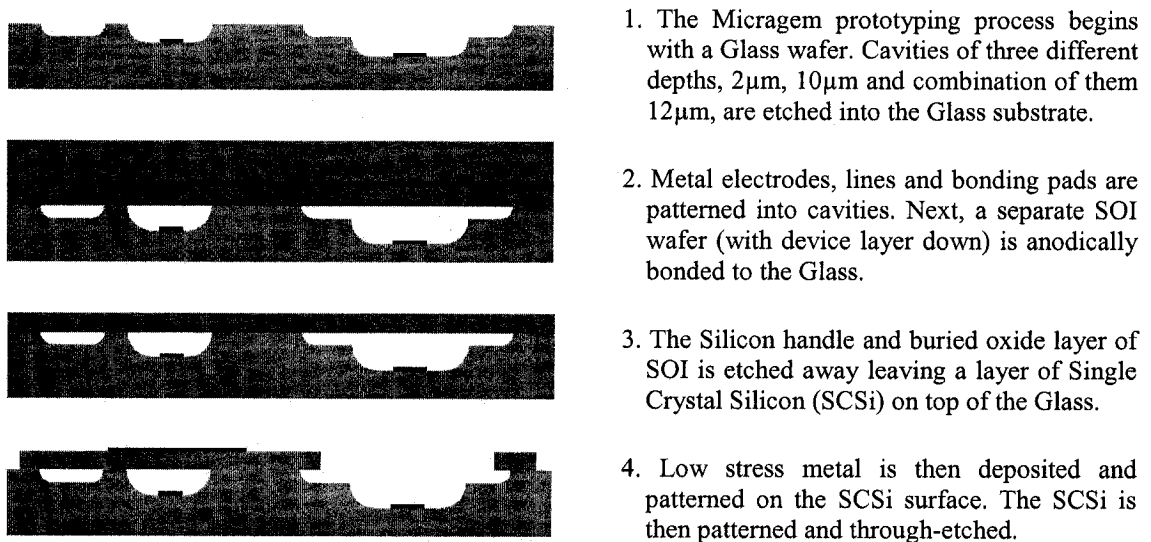


Fig. 5. 6. Scheme of Micragem process (adapted from CMC/SCM, 2005)

The area of each Micragem chip is 9mm \times 5mm \times 0.5mm. The same design ideas of PolyMUMPs process were transferred to the layout design of Micragem process, as shown in Fig. 5. 7. The SEM picture in Fig. 5. 8 offers an overview of microdevices on

the Micragem loose dice manufactured according to the layout design. The larger area of the Micragem chip allows that various designs of microbridges and mirror plates could be fabricated. What is more, the idea of the bottom electrodes of different independent devices sharing the same electrical pad efficiently makes efficient use of the area of the chip. Two kinds of cutouts were created as Fig. 5. 9, (a) the cutouts are located on the boundary and above the gap of the electrode layer so as to weaken the stiffness of the microbridge by changing the geometry (b) the cutouts are exactly located above the bottom electrode layer. Thus, not only the geometries of the microstructures were changed, but also the efficient area of the electrostatic actuators. Different patterns of bottom electrodes were designed to further analyze the influence of the electrostatic actuators' locations, as shown in Table 5.2.

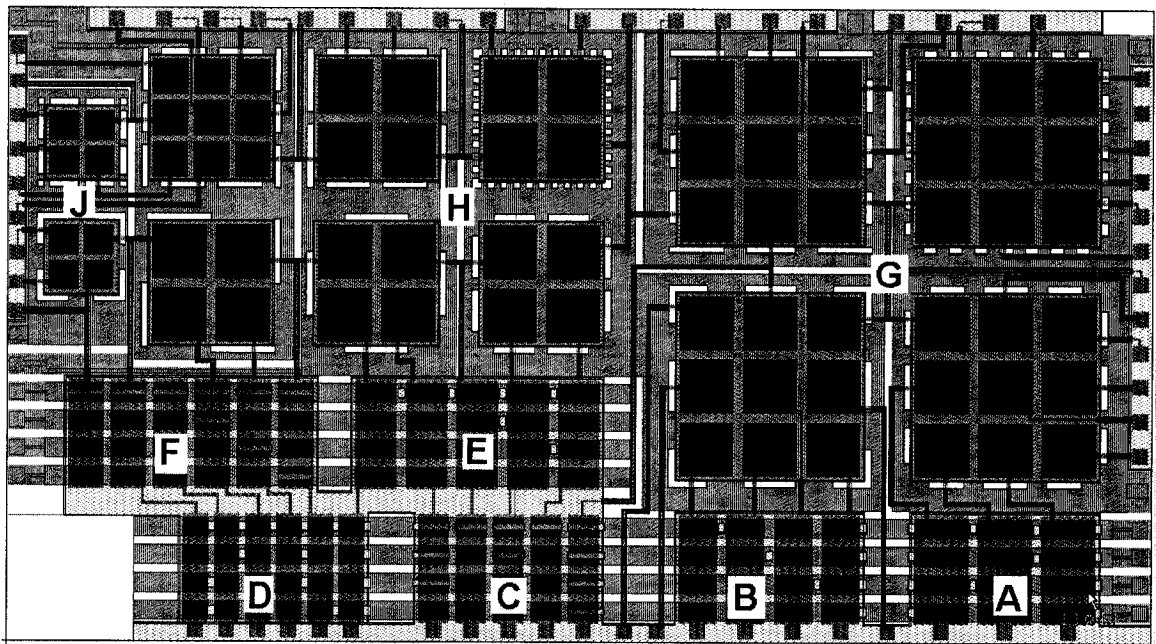


Fig. 5. 7. Layout of Micragem design with microbridges and microplates

Since the SCSi wafer and glass substrate are anodically bonded together, there are no etch holes present on top of the metal layer as compared to the MUMPS process. A low stress gold layer is deposited and patterned on the SCSi top surface before SCSi layer is etched through to create the desired microstructures. The top low stress metal layer enhances the optical reflectivity of the top surface which make Micragem process very suitable for MOEMS application. The top metal layer also makes electrostatic capacitors built between two metal layers against polysilicon electrodes in PolyMUMPs process. Obviously, Micragem SOI has many advantages over PolyMUMPs. It is a reliable technology to develop designs with low optical insertion loss, electrostatic actuation and low power consumption.

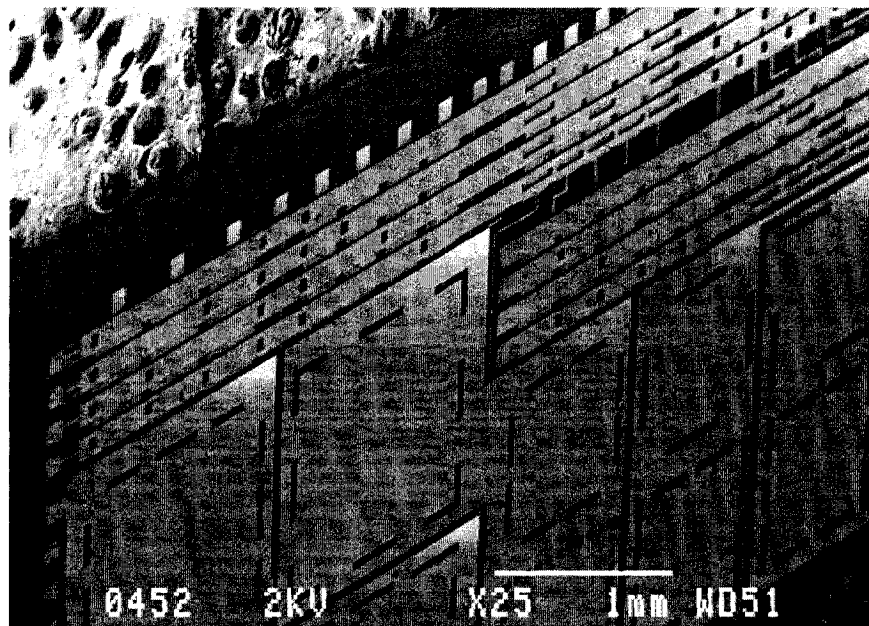






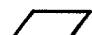


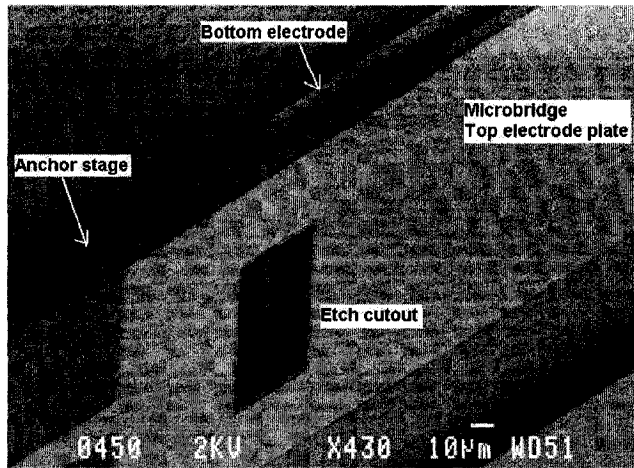


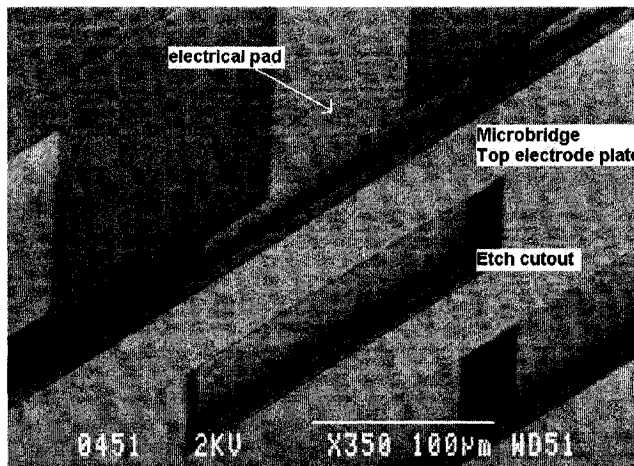
Fig. 5. 8. Close-up SEM view of the SOI microbridges and microplates designed on Micragem chip

Table 5. 2. Definitions of microstructures on the Micragem chip

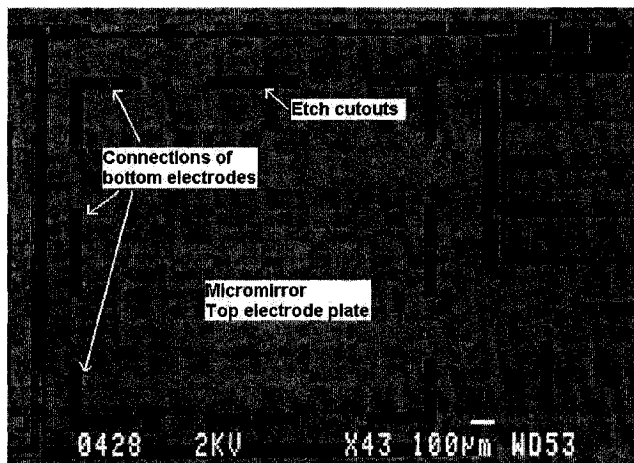
Region	Microstructure	Explanations
A		Microbridge array: L: 1500 μm , W: 150 μm , with 3 electrodes Width of electrode: 420 μm Gap between electrodes: 80 μm
B		Microbridge array: L: 1500 μm , W: 150 μm , with 4 electrodes Width of electrode: 295 μm Gap between electrodes: 80 μm
C		Microbridge array: L: 1500 μm , W: 150 μm , with 5 electrodes Width of electrode: 240 μm Gap between electrodes: 55 μm
D		Microbridge array: L: 1500 μm , W: 150 μm , with 6 electrodes Width of electrode: 200 μm Gap between electrodes: 50 μm
E		Microbridge array: L: 2000 μm , W: 150 μm , with 5 electrodes Width of electrode: 320 μm Gap between electrodes: 80 μm
F		Microbridge array: L: 2000 μm , W: 150 μm , with 6 electrodes Width of electrode: 270 μm Gap between electrodes: 60 μm
G		Microplate: 1500 μm \times 1500 μm , with 3 \times 3 electrodes Electrode: 420 μm \times 420 μm Gap between electrodes: 80 μm
H		Microplate: 1000 μm \times 1000 μm , with 2 \times 2 and 3 \times 3 electrodes Electrode: 420 μm \times 420 μm (2 \times 2) and 270 μm \times 270 μm (3 \times 3) Gap between electrodes: 80 μm
J		Microplate: 600 μm \times 600 μm , with 2 \times 2 electrodes Electrode: 270 μm \times 270 μm Gap between electrodes: 50 μm



(a)



(b)



(c)

Fig. 5. 9. SEM pictures of anchor, bottom electrodes, gap of electrostatic actuators and cutouts of Micragem structures

5.4 Wirebonding

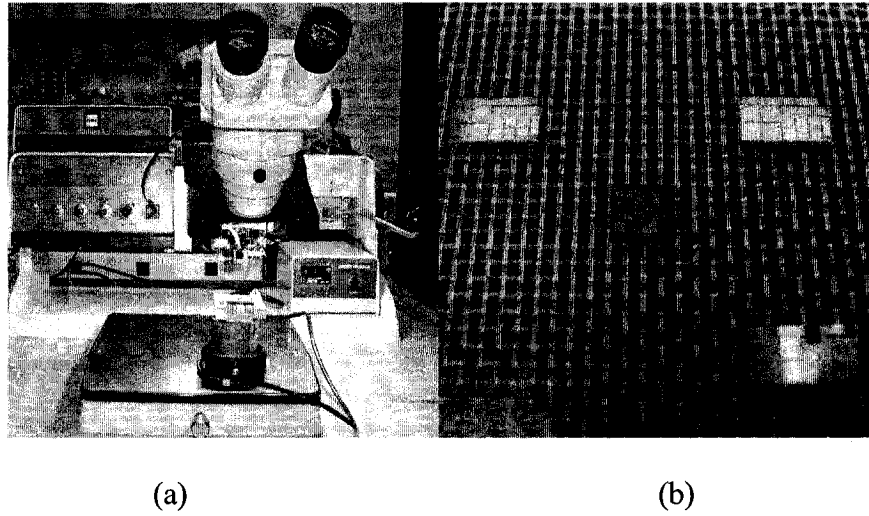


Fig. 5. 10. (a) WESTBONG 7400E manual wirebonding machine, (b) PolyMUMPs and Micragem loose dices

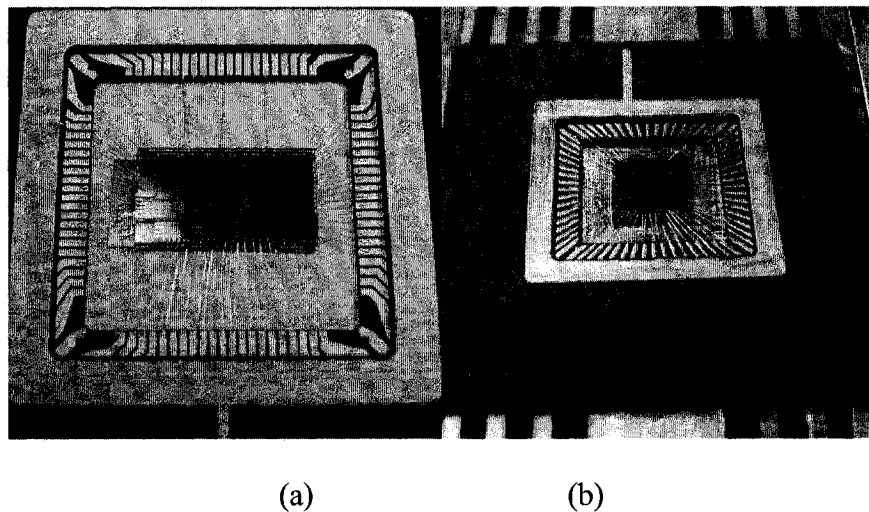


Fig. 5. 11. (a) Micragem and (b) PolyMUMPs chips after wirebonding

Wire bonding provides electrical connections for MEMS components. Besides the common wire materials, namely gold and aluminum, there are other materials such as

copper, silver and palladium. There are three common bonding techniques used in the IC and MEMS industries [Hsu T R, 2002], which include (i) thermocompression, (ii) wedge-wedge ultrasonic and (iii) thermosonic wire bonding.

The wire bonding equipment used in our laboratory is an ultrasonic/thermosonic wedge-wedge wire bonder, WESTBOND 7400E as shown in Fig. 5. 10(a). The machine bonds aluminum or gold wires ranging from 17 μ m to 50 μ m. Bonds are made by the wedge-wedge technique using ultrasonic energy to attach aluminum wire at room temperature and heating up the work piece for gold wire. Wire is clamped and threaded diagonally under the bonding wedge, allowing independent feeding action. The bonding tool is guided manually by the operator using hand/eye reference to bond targets. Small working distance of microscope requires the loose dices, as shown in Fig. 5. 10(b), must be packaged. Two kinds of Ceramic Pin Grid Array (PGA) cavities, namely 84 PGA and 68 PGA, were used for Micragem and PolyMUMPs loose dices respectively based on the electrical pad number and the size of chips. Fig. 5. 11 shows the chips after wirebonding.

The predominant failure in wire bonding is the intermittent lifting of bonds causing resistive contacts or open connections. Control of the bonding processes is critical to assure reliability in the interconnection. The following parameters need to be carefully assessed and implemented during this bonding process: (i) Process temperature (ii) Contact forces (iii) Atmospheric conditions (iv) Contamination of bonding surface and (v) Bonding time. Since a new 84 PGA cavity for Micragem chip as shown in Fig. 5. 11(a) and a reused 68 PGA cavity for PolyMUMPs chip, Fig. 5. 11(b) were tried using 20 μ m aluminum bonding wire, the surface contamination and metal purity would cause

very obvious variability in mechanical strength and performance of the bonds. This will result in poor structural integrity as well as a reduction in electrical performance. Although the standard set of force springs generates 15 to 250 gram force in the user manual, the suitable contact force have to be achieved by trial and error in practical use. The following parameters are used for WESTBOND 7400E in this wire bonding procedure, which are given for future reference.

Table 5. 3. The parameters of WESTBOND 7400E bonding machine

Vertical movement range (mm)	14.29
Horizontal movement range (mm)	15.88
Ultrasonic power supply (W)	3.25
Ultrasonic time (ms)	30
Wire feed angle (°)	45
Contact forces (gram force)	15~250
Bonding wire	Diameter 20 μ m, Aluminum
Work piece temperature (°C)	Aluminum wire: room temperature Gold wire: 100~140°C
Loop height before bond (μ m)	2540
Drop before clamp (μ m)	660
Motor steps for wire pull	34
Motor steps for wire tail	28

5.5 Summary

Two commercial micromachining processes, PolyMUMPs and Micragem were outlined in this chapter. The advantages of Micragem process for the applications of MOEMS were also presented. WESTBOND 7400E manual bonding machine were used for post process package and wire bonding. Some of parameters which influence the performance of wire bonding were studied and listed in this chapter. They can work as a guide line for wire bonding process troubleshooting. The microbridge fabricated through Micragem

process will be used for the out of plane deflection testing under different applied voltages on the electrostatic actuators. The fabricated designs will be analyzed, tested and verified with theoretical models.

Chapter 6

6 EXPERIMENTAL DESIGN AND VALIDATION

6.1 Introduction

In the previous chapters, the numerical analysis of the nonhomogeneous boundary conditions, static and dynamic characteristics of microstructures, bridges and plates working under multiple electrodes have been presented. Theoretical analysis alone cannot be fully relied upon for the performance analysis unless it is validated by tests. For example, the boundary conditions, the rotational stiffness and translational stiffness need to be quantified and estimated for real technologies. Hence, experimental testing for the microstructures is necessary for validation and developing reliable working devices. The applications of new techniques, however, are always intriguing and present new challenges at the same time.

Multiplicity, multidisciplinary integration and miniaturization are the three main reasons to make MEMS technology popular. MEMS technology reduces the physical size and weight of sensors and actuators and makes them appealing in many new applications. At the same time, MEMS devices pose a great technical challenge for testing and measurement as they are extremely sensitive to outside environment. Therefore, a non contact testing technique is much preferred for this application.

The surface contour and deformation measurement of MEMS devices are beneficial in providing feedback to manufacturing process and investigating the working response of micro components. Another reason for using non contact testing technique is its

simplicity in terms of setting up the test platform. Several non contact techniques have been investigated for the measurement of surface characteristics. These include scanning electron microscopes (SEM), laser scanning, light scattering approaches and various interferometric techniques, such as Tolansky multiple beam interferometry and two-beam interferometry based on Michelson, Linnik and Mirau.

Optical interferometric technique is believed to be the most versatile measurement tool for non contact surface measurement since they give a direct measure of surface height [Hariharan P, 1985; Quan C et al., 2003]. With suitable computer analysis, these can provide surface characteristics with high precision [Wang S H et al., 2000]. Among the various forms of interferometers, double beam interferometry is especially simple and straightforward in principle, as well as in practice, and is therefore utilized for a wide range of applications. The actual sample can be measured directly without applying a high-reflectivity coating. Since the surface-height profile is being measured, the actual values of heights, slopes and curvatures of surfaces can also be determined.

While several two-beam interferometers can be used for deformation measurement, a coaxial interference Mirau technique [Wang S H and Tay C J, 2006; Bhushan B et al., 1985] based on the principle of Michelson interferometer was selected in the study. With this technique, whole-field surface contours on different conditions can be evaluated quantitatively. Its advantages and limitations will also be discussed in this chapter.

6.2 Interference Phenomenon

The interference rings were first studied by Isaac Newton. When two light beams interfere, they produce interference patterns depending upon the phase difference [Dwight E G]. If crests are superimposed on the crests or valleys on valleys, the waves will be mutually reinforced. While, if crests are superimposed upon valleys, two will be mutually cancel. Consequently, a succession of alternately bright and dark interference fringes will arise.

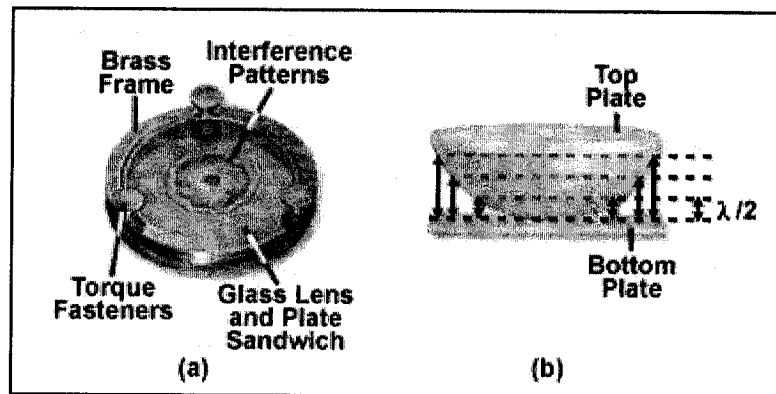


Fig. 6. 1. Interference fringe formation (adapted from *Nikon's MicroscopyU*)

The interference fringes appear like contour lines in Fig. 6. 1(a) on the top surface of the apparatus at intervals corresponding to height differences of half a wavelength of light source as shown in Fig. 6. 1(b). Newton's rings formed in an apparatus that allows a convex lens to contact with a flat glass plate. The order of the interference fringes, denoted by N ($N=0,1,2,\dots$), is counted from the dark disk at the center of the pattern. The interference fringes will satisfy the following condition [Tolansky S, 1996]:

$$N\lambda = 2nt \cdot \cos \Phi \quad (6. 1)$$

where, t the distance between the flat glass plate and convex lens; n the refractive index; Φ the angle of incidence of the light waves.

For the case for perpendicular incidence, $\cos\Phi=1$ and in a vacuum or in air, $n=1$, and the relation reduces to:

$$t = \frac{1}{2} N\lambda \quad (6.2)$$

The interference fringes appear at intervals corresponding to height differences of half a wavelength. Similarly, the breadth of the interference fringes governs the precision obtainable in the interferometric measurement of the irregular surfaces. This method clearly illustrates the based principle of interferometry but it has a big disadvantage that the specimen must be placed in contact with the reference plate.

6.2.1 Michelson Interferometer

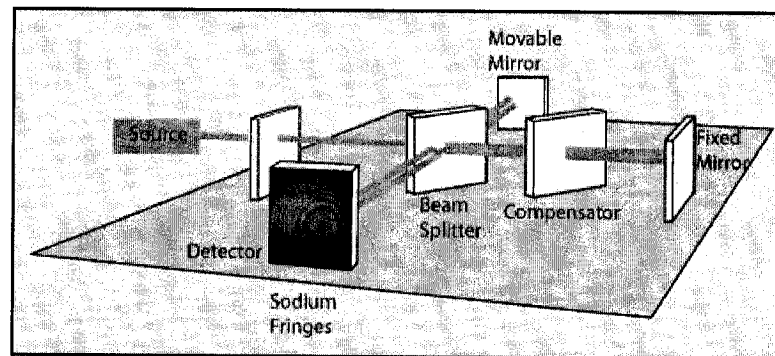


Fig. 6. 2. Principle of the Michelson interferometer (adapted from Tolansky S, 1996)

Michelson's spectroscopic technique, despite having revealed for the first time the fine structure of spectral lines (1881), did not become a popular method until the last decade. The principle of the Michelson interferometer is illustrated in Fig. 6. 2. A beam emitted

by light source is split into two beams of nearly two equal intensity by a half mirror (beam splitter). One of these beams is directed onto a flat reference fixed mirror and the other onto movable mirror under testing. When the reflected beams are brought back together, they result in an interference pattern depending upon the path difference. Since the light waves reflected by the specimen and the reference mirror originate from the splitting of a beam emitted by the same light source, these waves are mutually coherent and consequently a stable two-beam interference pattern is achieved. Because of the presence of the compensator between beam splitter and reference fixed mirror, the two divided light beams arrive at the viewing port after propagating through the equivalent optical distance. The interaction of the waves on a viewing surface alternates between constructive interference and destructive interference causing alternating lines of dark and light depending upon the position of the moving mirror. The physical width of a fringe is governed by the difference in the angles of incidence of the component beams of light. Precise distance measurements can be made with the Michelson interferometer by moving the mirror and counting the interference fringes which move by reference point. The distance can also be calculated with Eq. (6. 2) associated with the number of fringes.

In Michelson type interferometer, the beam splitter and specimen surface are separated by an appropriate distance. Thus, an interference pattern is obtained without contact. Although this method has many advantages, the main drawback is the alignment of the light source, optical devices and microdevices. In the testing, the light scattered from the device and other equipments can also create problems since cross-talking of the light from various sources will make the optical detector yield the ambiguous results. The Mirau interference objective can offer an efficient solution to these problems.

6.2.2 Mirau Interference Objective

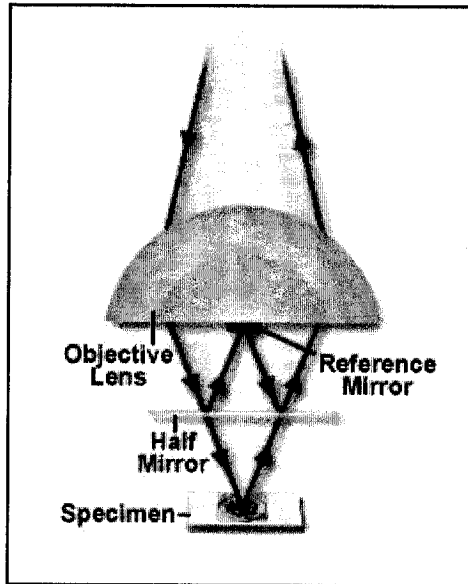


Fig. 6. 3. Mirau interference objective (adapted from *Nikon's MicroscopyU*)

The Mirau interference objective is an interference objective of comparatively high magnification (10x, 20x, or 40x) normally used in microscope instruments. It consists of an objective lens, a reference mirror and a beamsplitter. The principle of the device, as illustrated in Fig. 6. 3, relies on placing a reflection reference mirror at the center of the objective lens and the half mirror between the objective lens and the specimen. Similar to optical paths in a typical Michelson interferometer, two beams traveling along the optical axis reflected from the reference and the test surface, respectively, are recombined to interfere with each other when the system is focused on the specimen. Non-contact measurements can be performed with Mirau interference objective.

The principal advantage of the Mirau interferometer is that the manufacturer performs the optical alignment. Mirau interferometer obviates the need for precision alignment. Users do not need to focus the target while maintaining the optical paths to this precision, which

would be difficult and tedious. Because the center of the reference mirror coincides with the optical axis, the interference pattern will immediately appear at the center of the field of view. Thus, the troublesome manipulations are required for central observation sometimes.

6.3 Measurement Techniques

This section is divided into three major parts. The first part is outline of the instrumentation used for experiment. The second part is the gap measurement. The gap value of the electrostatic actuators is a very sensitive parameter for out-of-plane deformation of the microbridge in the theoretical model. For this reason, the loose dices are mounted perpendicularly so that the thickness of microstructures and gap value can be measured from the lateral side. The third part will be Fourier Transformation method, which will be used to process the images and extract required data to compare with the results from the prediction.

6.3.1 Experimental Platform

The experimental arrangement shown in Fig. 6. 4 mainly consists of an Olympus BX60M microscope, a Nikon 10x Mirau objective, an *INFINITY* digital camera, a Chroma D625/20X filter, a three-channel DC power supply and DC to HV DC converter. The equivalent optical system shown in Fig. 6. 5 consists of a Halogen light bulb, lenses 1 and 2, and a heat filter. The monochromatic light ($\lambda = 625 \mu\text{m}$ center wavelength and 20 bandwidth) is generated using a filter fitted in the filter slider. Lens 3 is used to guide the monochromatic light on to the test device through a cube beamsplitter and Mirau

objective. Although the aperture and field diaphragm can be adjusted to collect the light near the optical axis, two points should be noted in such cases. First, it is important to precisely ascertain the characteristic wavelength of the filter as the maximum transmitted wavelength usually varies to some extent with respect to particular interference filter being used. Secondly, the filter must be inserted perpendicular to the optical axis, as slight obliquity will cause a shift toward shorter wavelengths. A tilt and rotation stage was used combining with the x-y-z translation test stage of the microscope to form a 5 axis test stage, as shown in Fig. 6. 6. The microbridge was actuated by the output DC voltage of HV DC converter, which can be read out directly from digital multimeter.

The Mirau objective directs the beams reflected from reference mirror and test surface onto the CMOS sensor in the *INFINITY* digital camera. Since the reference and test surface are mounted on the same axis, the coaxial arrangement of two interference paths causes the interference fringe pattern to immediately emerge in the center of the field of view and renders the system relatively insensitive to external vibration and air turbulence. A computer, which is connected to the digital camera, is used to view the real-time changing fringe patterns. The results are recorded by the digital camera with true color BMP format. The commercially available software package, *Fringe Processor*TM is used for quantitatively evaluating the resulting interferogram. The proposed system can retrieve the surface profile and deformation of the test objects.

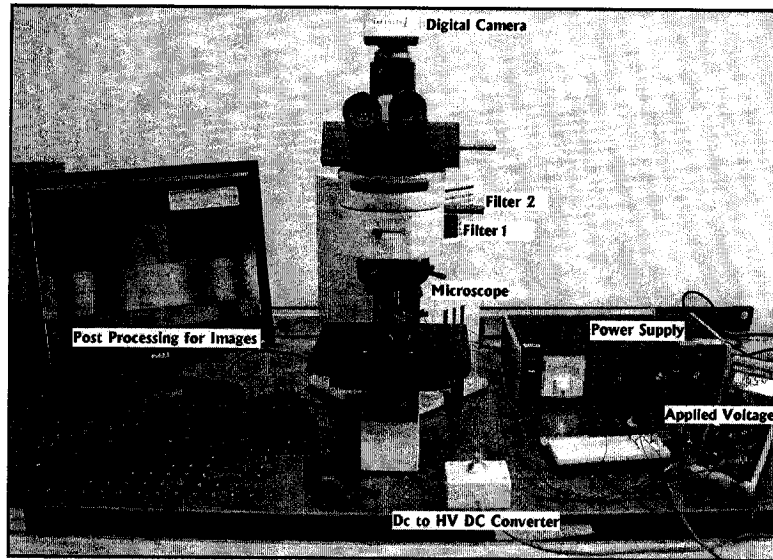


Fig. 6. 4. Experimental set up for measuring the out of plane deflection

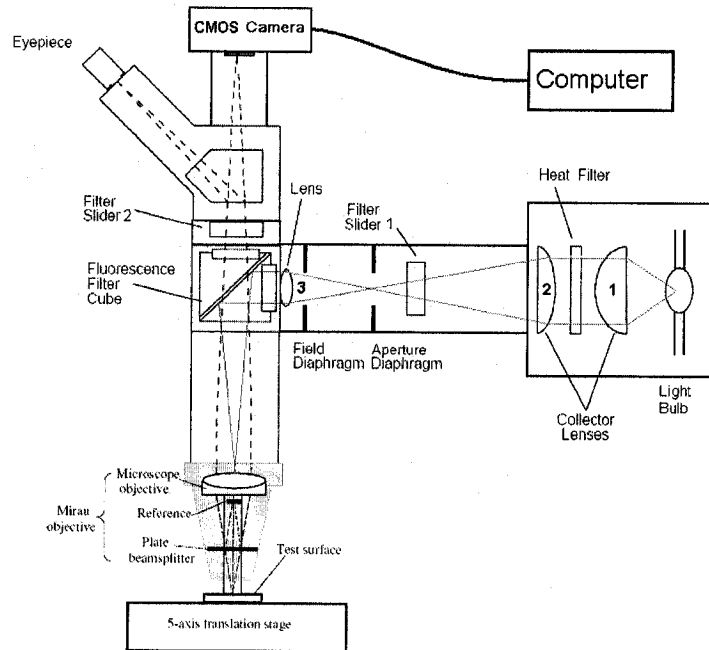


Fig. 6. 5. Schematic of the proposed interferometric system

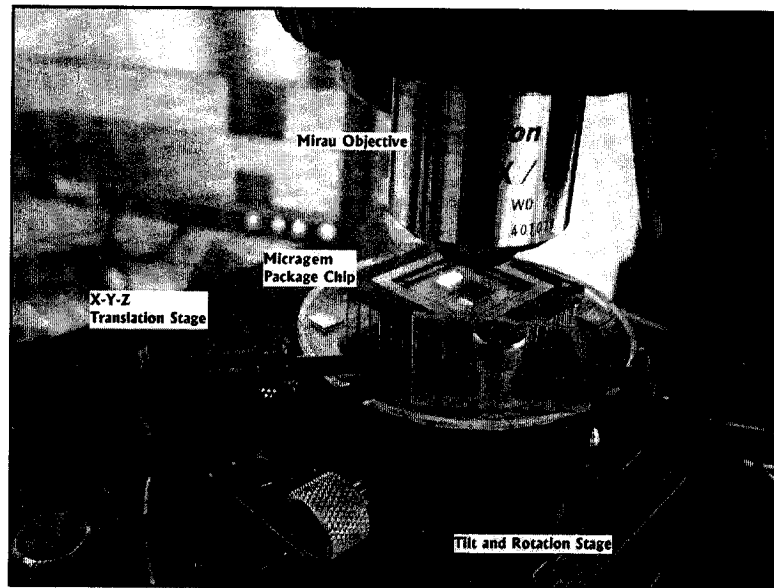


Fig. 6. 6. Fixture of the Micragem chip in measurement

Mirau interferometer does greatly reduce the working distance of the optical system. The smaller working distance restricts experimental setup and hence the parts must typically be wire-bonded. The structures to be measured should be near the surface as shown in Fig. 6. 6.

6.3.2 Gap Measurement

Compared with the wavelength of the light source used in measurement, the height differences between top of microstructures and bottom electrode are quite large. The experimental setup mentioned about can also be used to distinguish the absolute level differences by adjusting the focus of the objective. However, if the level differences are of the order of the wavelength of the light used in the observation, then this method cannot be done. This ambiguity can be eliminated by using white light in two-beam interferometry. The interference fringes are arrayed in increasing order from the vicinity of the reference plane toward the periphery of the object and the order of the fringes can

be determined from their color arrangement. Thus, the size of the air gap can be traced from sequence of colors in the interference fringes.

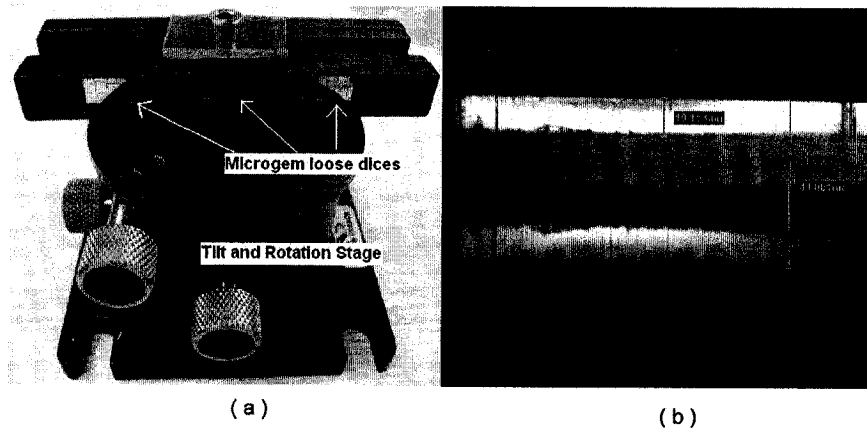


Fig. 6. 7. (a) Micragem chips installation and (b) one result of gap measurement

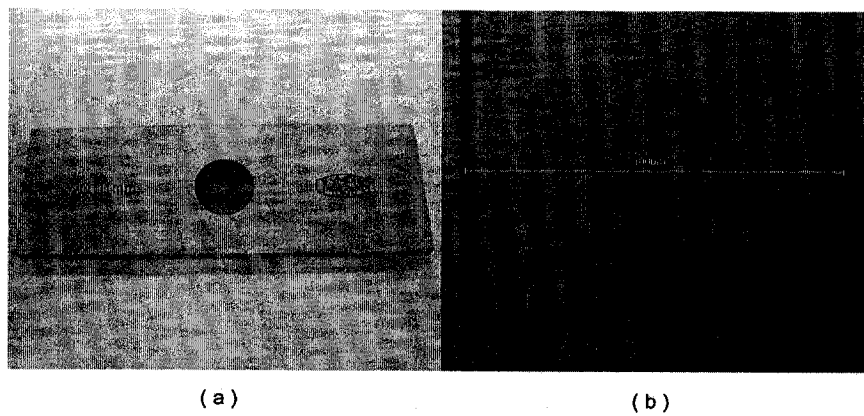


Fig. 6. 8. Microruler used for the calibration the measurement results

Here, a straight forward method is used to read out the values of the gap based on the reflection property of glass substrate. The microbridges located on the lateral side make it convenient for measurement. Some loose dices are mounted perpendicularly on the tilt and rotation stage so that the microbridges can be observed laterally under the microscope, as shown in Fig. 6. 7(a). Because the base substrate of Micragem chip is

glass, the image of the suspending structure and its reflection are symmetrically shown in one of the captured images Fig. 6. 7(b). The distance of the top and bottom surface is just twice the distance of top structure surface to the bottom electrode. An Olympus microruler shown in Fig. 6. 8(a) and *IMT iSolution Lite* software were used to calibrate pixel to pixel distance as shown in Fig. 6. 8(b). Once the camera is calibrated, distance can be directly measured in micrometer from the image. The average values of structure thickness and the gap are 10.2 μm and 11.8 μm , respectively. The dielectric gap between the metal electrodes can be calculated as follow:

$$d^* = d_0 + \frac{t}{\varepsilon} \quad (6. 3)$$

where, d^* is the dielectric gap, d_0 is the air gap, t is the thickness of the microstructure and ε is the dielectric constant of single crystal silicon given in the Table 6. 1.

6.3.3 Fourier-Transform Method

There are several methods, such as, fringe tracking, Fourier-Transform (FT) and phase shifting interferometry methods that can be used for measuring the surface properties based on the fringe patterns. Although fringe tracking method can be obtained by direct superposition of the grating photographs with one another, such a simple procedure does not yield the best results, nor does it exploit the full potential of the information that is stored in a photograph of a deformed specimen grating. Phase shifting method is based on the reconstruction of the phase by sampling a number of fringe patterns differing from each other by various values of a discrete phase. There is no doubt that the phase shifting can give much more accurate surface height variations measurement. The accuracy of

this method can be within 1nm [Wyant J C et al., 1984]. In this application, the reference mirror of Mirau objective must be adjustable and mounted on a closed-loop controlled piezoelectric transducer (PZT) [Quan C et al., 2003; Bhushan B et al., 1985]. By applying a voltage to the PZT, the reference mirror can be translated to vary the phase of the reference beam. It is capable of eliminating the local phase ambiguity in an interference pattern compared with FT method.

FT method offers the possibility of performing filtering operations on space-dependent optical signals in manner analogous to the treatment of time-dependent vibration and electrical signals. It only needs one interferogram with a monotonic phase distribution and degrades the speckle noise and background variation. It is based on fitting a linear combination of harmonic spatial functions to the measured intensity distribution $I(x,y)$ [Takeda M et al., 1982; Gorecki C, 1992]:

$$I(x, y) = a(x, y) + c(x, y) + c^*(x, y) \quad (6. 4)$$

$$c(x, y) = \frac{1}{2}b(x, y)\exp[i\delta(x, y)] \quad (6. 5)$$

where, $a(x,y)$ represents the low-frequency background intensity, $b(x,y)$ is the local fringe visibility, $\delta(x,y)$ is the local fringe phase and '*' denotes the complex conjugation. Main purpose of the problem is to determine $c(x,y)$ or $c^*(x,y)$ from intensity $I(x,y)$. Fourier transform is used for demodulating the interferogram. The Fourier transform of Eq. (6. 4) is given by

$$I(u, v) = A(u, v) + C(u, v) + C^*(u, v) \quad (6. 6)$$

Since (u, v) being the spatial frequencies, A , C and C^* represent the complex Fourier amplitudes. $I(u, v)$ is a Hermitian distribution in the spatial frequency domain. Thus, the real part of $I(u, v)$ is even and the imaginary part is odd. The amplitude of spectrum, the absolute value of $I(u, v)$ is symmetric with respect with the term $I(0, 0)$. Therefore, $C(u, v)$ and $C^*(u, v)$ carry the same information.

The admissible spatial frequencies are defined by the user via the cutoff frequencies of a band-pass filter in the spatial frequency domain. The unwanted additive disturbances $A(u, v)$ can be eliminated together with the mode $C(u, v)$ or $C^*(u, v)$ by a user defined band-pass filter. For example, If only the mode $C(u, v)$ is preserved, the Hermitian condition no longer exist in the amplitude spectrum. A complex value $c(x, y)$ will be achieved after inverse Fourier transform. The phase difference can further be calculated by

$$\delta(x, y) = \arctan \left[\frac{\text{Im } c(x, y)}{\text{Re } c(x, y)} \right] \quad (6. 7)$$

The principal value of the *arctan* function has a continuous period of 2π . In order to get a continuous phase distribution, phase unwrapping is necessary.

$$\cos(\delta) = \cos(s \cdot \delta + N \cdot 2\pi) \quad s \in \{-1, 1\} \quad (6. 8)$$

N is an integer and denotes the fringe number in the measuring region. If the phase is not monotonically increasing, this technique leads to a phase ambiguity, which can be evaluated by using of a second interferogram phase shifted [Kreis T, 1986] or compared two phase distributions reconstructed from the same interferogram using two different

band-pass filters [Kreis T and Juptner W P O, 1989]. Since the *Fringe Processor*TM does not include such function in the FT method for phase sign correction, the phase should keep increasing in the images used for evaluation. On the other hand, the view angle of the *INFINITY* digital camera is not wide enough to take the whole view. Every experimental result is achieved by combining adjacent images. Therefore, only the symmetrical deflections are considered in the next section.

6.4 Testing Procedure and Validation

The microbridge used in testing and its 3D model are shown in Fig. 6. 9. Its geometry dimensions and material properties are listed in Table 6. 1. In order to make use of the Mirau objective as a tool to measure the deflections of the microbridge, it is important to reference the initial position of the measured surface. First of all, the Mirau objective is adjusted until a clear interference pattern can be seen. Further adjustment of focus will cause shifting of fringes. A reference surface, which is the bottom electrode, is chosen for horizontal adjustment for the whole chip. Therefore, surface situation can be obtained according to the fringe pattern on the reference surface. Adjust the two knobs on the tilt and rotation stage to vary the tip-tilt of the reference surface on the chip. Since the broad band light source with center wavelength 625 μm and 20 μm band width used in experiment, the focus needs to be adjusted to maintain the fringe pattern, keeping two light waves coherent, or to increase the fringe contrast for most of time. This procedure is repeated until the fringes become fuzzy and broader to make sure the surface close to horizontal condition. At the end, the fringe pattern will disappear and a bright region or

just a halo is left behind. Now, the focus on the microbridge surface is readjusted to find the initial position of the testing surface.

Table 6. 1. Dimensions and material properties of test microbridge

Length (μm)	Width (μm)	Etch hold (L×W) (μm)	Elastic Modulus $\langle 100 \rangle$ (N/m^2)	Density (kg/m^3)	Dielectric Constant
1500	150	50×70	1.295×10^{11}	2320	13.5

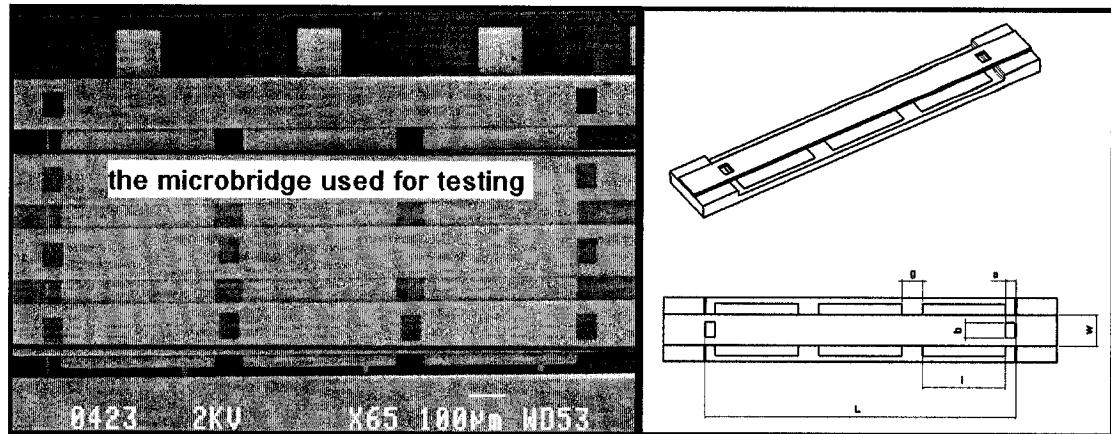


Fig. 6. 9. The microbridge structure used in testing and its 3D model

The top layer of the microbridge is made as ground. DC voltage is applied between electrodes. Here, three cases were considered (i) voltages applied only to the central electrostatic actuator (ii) same voltages applied to two side electrostatic actuators and (iii) same voltages applied to all the three electrostatic actuators at the same time. Because symmetrical deflections are achieved from these three cases, the order of fringes in the result images will only increase/decrease.

Fig. 6. 10 shows interference fringe patterns under different voltages applied only at the central electrode. With the voltage increases, new fringe will be generated from the centre of microbridge. At the same time, the fringe pattern will shift from center to two

side anchors. The breadth of each fringe and the distance between them will keep changing correspondingly. Because these patterns are photographed with monochromatic red light, the interference pattern would be displayed with almost the same contrast, but the continuity of the fringes would become obscure at the sites of abrupt changes in level.

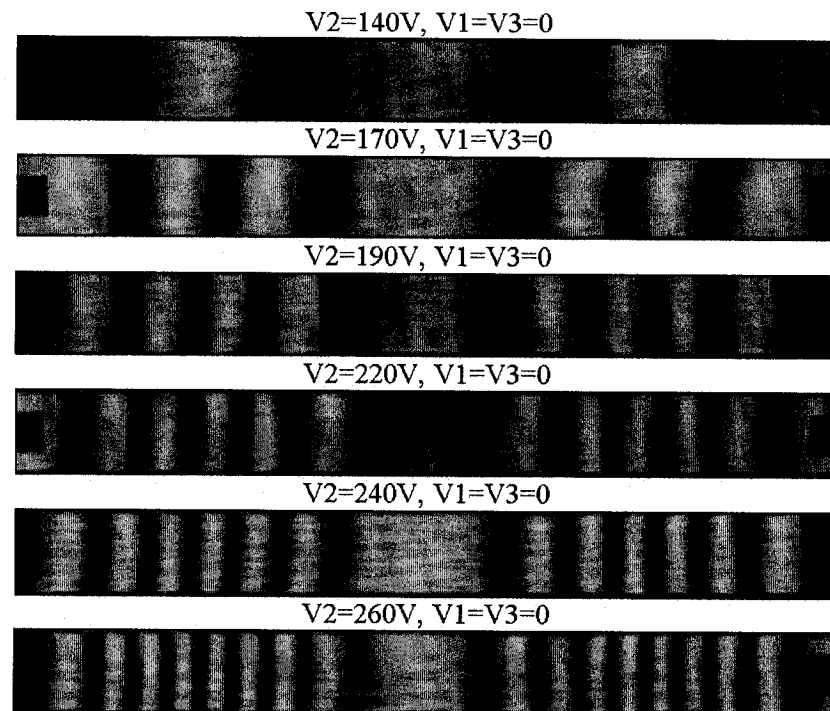


Fig. 6. 10. The fringe patterns of the microbridge for different applied voltages only on central electrode

The resultant images captured by the digital camera are in true color BMP format. The images have to be changed to 256 grayscale TIF format and resized before being evaluated by *Fringe Processor*TM. The last case in Fig. 6. 10, when voltage $V_2=260$ V is used for illustration here.

The following steps are applied to implement the FT processing: (i) extracting the mask of the measuring area and zero padding of the non-measuring area (ii) 2D FFT, (iii) 2D band-pass filtering by loading window function, (iv) inverse 2D FFT to obtain the

wrapped phase image, (v) unwrapping the saw tooth image to reconstruct the continuous phase distribution (vi) calculation of the surface profile.

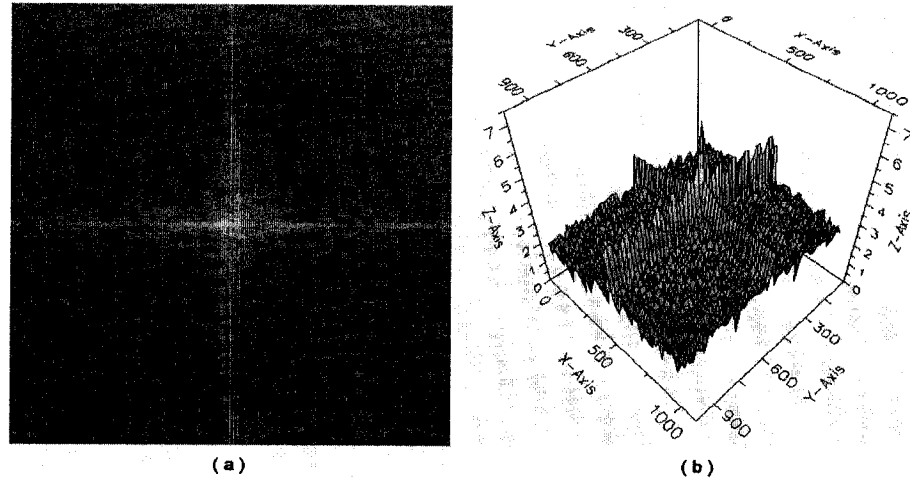


Fig. 6. 11. 2D and 3D FFT spectrum when $V_2=260$ V, $V_1=V_3=0$

Fig. 6. 11 is the FFT spectrum of the last case in Fig. 6. 10. It is clear to see that there are two close bright spots in the Fig. 6. 11(a), which are corresponding to two peaks of the symmetrical frequency spectrum of $C(u,v)$ and $C^*(u,v)$. Thus, a half plane window function for 2D band-pass filter can be specified.

From Fig. 6. 12, in wrapped phase distribution, the positions of dark fringes coincide with 2π phase difference. Therefore, the phase distribution of unwrapped phase can be determined by Eq. (6. 8) mathematically. If the phase difference between consecutive pixels is greater than π , then 2π will be added to the second pixels phase value so that new phase difference of pixels is between 0 to π again. Each row perpendicular to the fringes is unwrapped individually and a 2D phase distribution can be achieved. Adding up the data of each row, a 3D continuous phase difference surface can be constructed as

shown in Fig. 6. 13(a) and (b). The phase difference can further be transferred into real deflection of the microbridge based on the follow equation,

$$H_{x,y} = \frac{\delta_{x,y} \cdot \lambda}{2\pi(\cos \phi_1 + \cos \phi_2)} \quad (6.9)$$

where, $\delta_{x,y}$ the phase difference of the surface; ϕ_1 and ϕ_2 the angle of incidence of the light waves; λ the be center wavelength of the broad band light source. For the Mirau objective used in the experiment, the incidence of the light waves is perpendicular, with $\cos \phi = 1$.

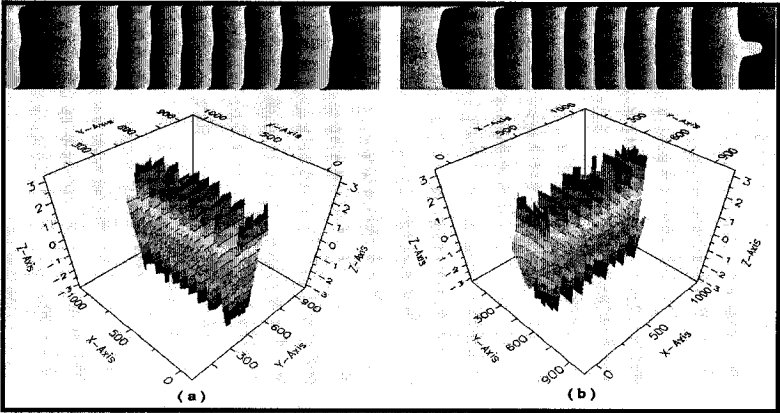


Fig. 6. 12. 2D and 3D wrapped phase map

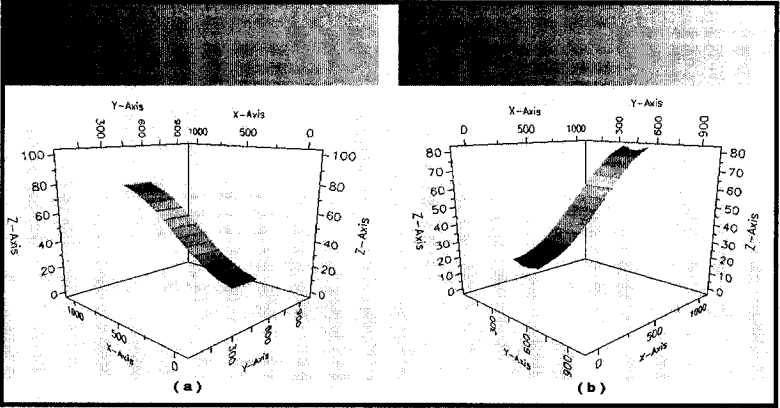


Fig. 6. 13. 2D and 3D unwrapped phase map

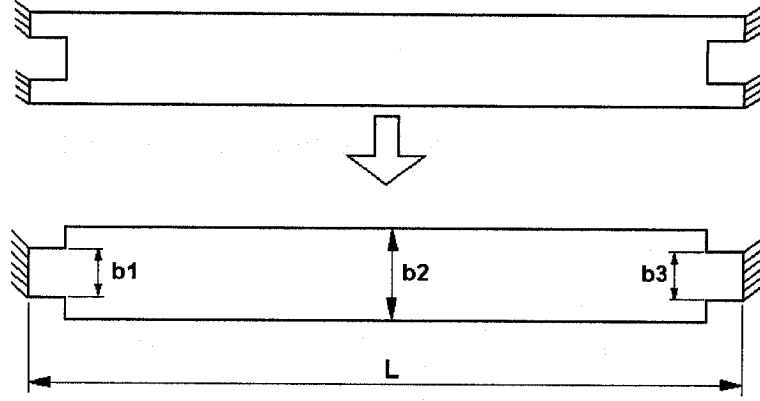


Fig. 6. 14. Equivalent structure of the microbridge used for experiment

In order to compare with the experimental results, the numerical model has to be adjusted according to the structure of microbridge used in experiment as shown in Fig. 6. 14. Since through etch holes are added at the two sides of the microbridge to lower the stiffness of the structure, the strain energy of the microbridge due to bending is estimated after taking into account the effect of cutouts as follows.

$$U_b = \frac{Et^3}{24L^3} \left\{ \int_{x_0}^{x_1} b_1(x)[W''(x)]^2 dx + \int_{x_1}^{x_2} b_2(x)[W''(x)]^2 dx + \int_{x_2}^{x_3} b_3(x)[W''(x)]^2 dx \right\} \quad (6. 10)$$

where, b_i are the beam width at different sections,

x_{i-1}, x_i are the coordinates defining the section with corresponding width b_i .

After normalized with respect to main width of the microbridge, the dimensionless translational stiffness K_t^* and rotational stiffness K_r^* are redefined as:

$$K_{ts}^* = \frac{K_{ts} L^3}{EI_2} \quad \text{and} \quad K_{rs}^* = \frac{K_{rs} L}{EI_2} \quad (s = 1, 2) \quad (6. 11)$$

Most of boundary conditions of MEMS structures fall between simply supported condition represented by a very high value of K_t and zero value of K_r , and clamped condition represented by a very high value for both K_t and K_r . This kind of boundary condition is referred to as semi-rigid boundary conditions. The glass substrate of the Micragem chip will not allow translational motion at the support. Therefore, only the rotational stiffness K_r is variable while the K_t value can be very large. Fig. 6. 15 shows the maximum deflection of microbridge with three electrodes against K_r^* when different voltages were applied only on the central electrode. Based on the experimental results shown in the Table 6. 2, the K_r^* value of Micragem microbridge was found to be between 15 and 22. After comparing with the experimental results of other cases, $K_r^*=15$ was chosen and the corresponding K_r value is equal to 1.145×10^{-1} N/rad.

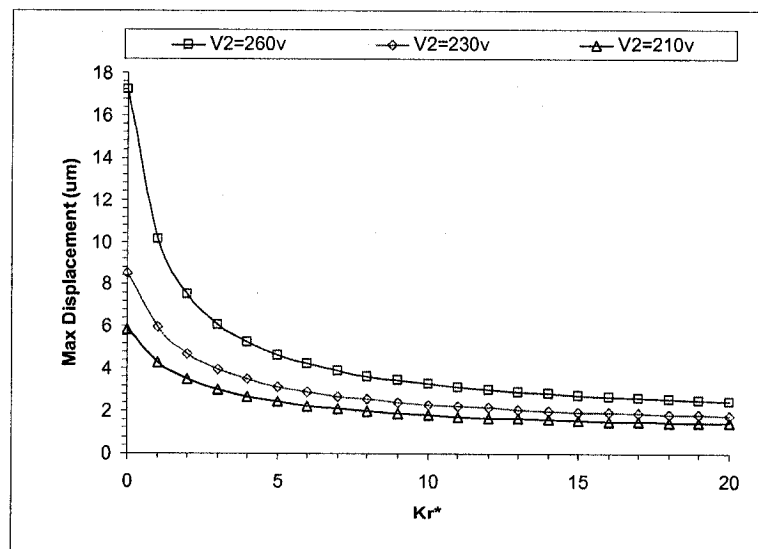


Fig. 6. 15. Maximum deflections vs. K_r^* in the case voltage only applied at central electrode

6.4.1 Case 1: Voltage Applied only at the Central Electrode

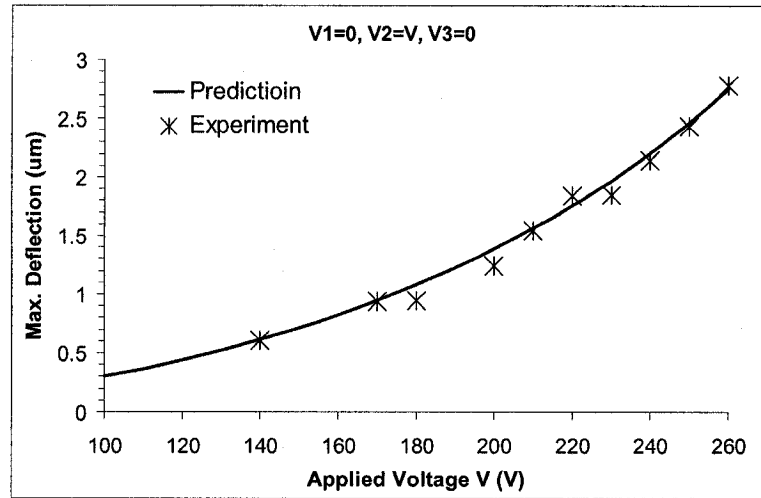


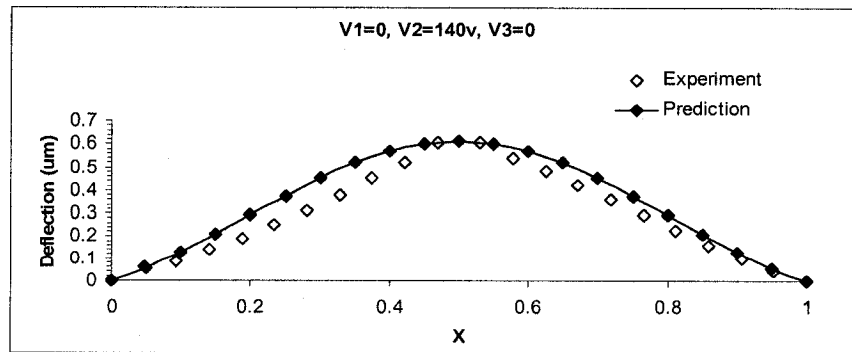
Fig. 6. 16. Discrepancies between the experimental and theoretical maximum static deflection when voltage is only applied at central electrode

Table 6. 2. Comparison of the maximum deflection between prediction and experiments when voltage is applied only at central electrode

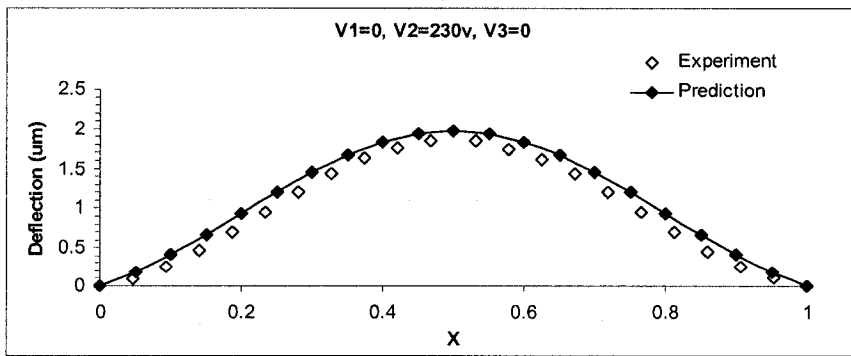
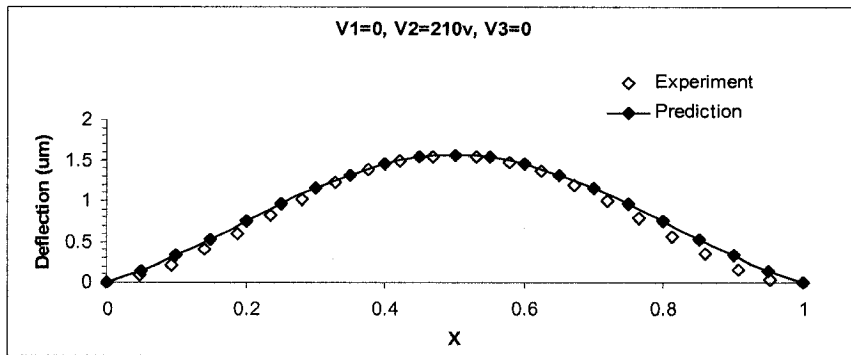
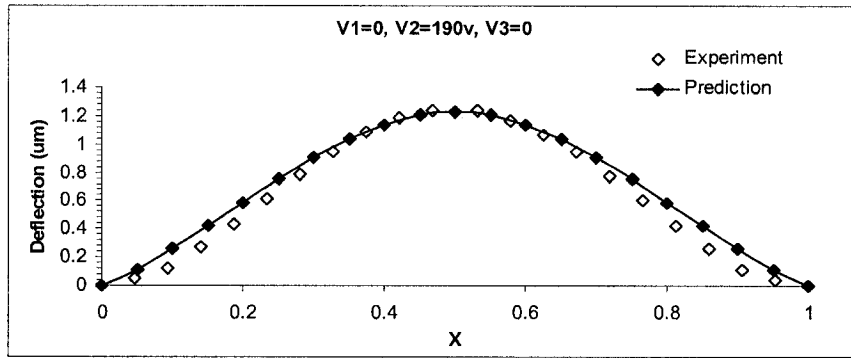
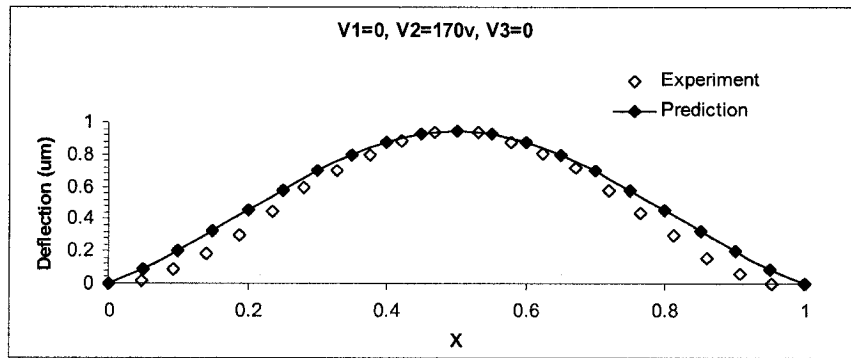
The maximum deflection (μm), with $K_r^* = 15$							
Applied voltage (V)	260 V	250 V	230 V	210 V	190 V	170 V	140 V
Present prediction	2.750	2.465	1.973	1.566	1.229	0.949	0.615
Experiment	2.779	2.435	1.851	1.546	1.240	0.937	0.608
Error (%)	1.02	1.22	6.17	1.29	0.87	1.21	1.12

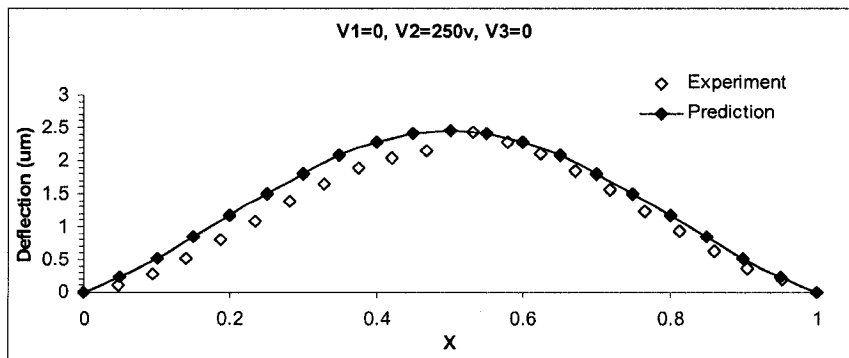
For the Case 1, the values of maximum deflection from the proposed method and experimental results are listed in Table 6. 2 and plotted in Fig. 6. 16. When different voltages are applied to the central electrostatic actuator, the static deflections would change as shown in (a) ~ (g) of Fig. 6. 17. Because the wavelength of the filter is $625 \mu\text{m}$, very fringe stripe represents for half of wavelength, $\frac{1}{2}\lambda$. From the first case shown in Fig. 6. 10, only two fringe stripes are achieved on each side of microbridge when 140 V is applied only on the central electrode. The experimental result and prediction based on this image are given in Fig. 6. 17(a). The deflection of the microstructure cannot be

correctively evaluated. The image's quality, fringe number and the process abilities of the software *Fringe Processor*TM can be estimated based on this comparison. It is the reason that experimental results are shown starting over 100 V at the central electrode actuator. As the electrical forces are focusing at the middle of the microbridge, high slope near the central deflection will give a clear and high contrast fringe pattern, which will directly improve the accuracy of maximum deflection in the experimental results. Therefore, the maximum deflection is chosen for defining boundary condition, the rotational stiffness K_r value. Since the tow-side deflections are too small to be accurately measured, main errors are also involved in these locations. This can be found in Fig. 6. 17(b) and (d) by comparing some unsymmetrical deflections of two sides. Another problem causing errors in experiment is that every result is achieved by combining two independent images. Although the symmetric deflections of the microbridge can remedy this problem, some errors are unavoidable when initial position is changed. This problem can be found in Fig. 6. 17(f) and Fig. 6. 20(b) of Case 2. Compared some experimental results and theoretical prediction, the shifting static deflections of the microbridge are clearly shown in Fig. 6. 18 for different voltages applied only at the central electrode.

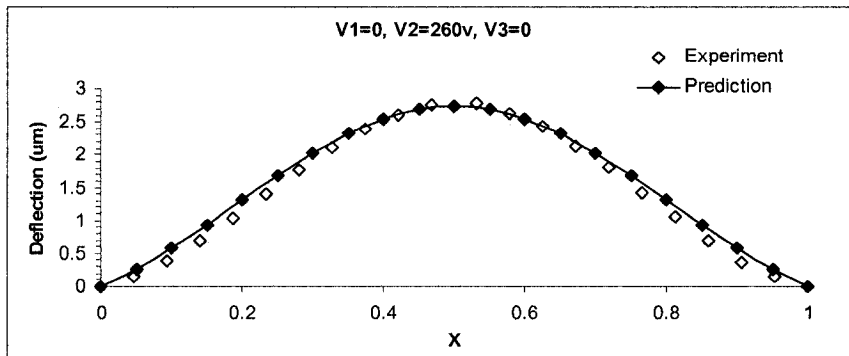


(a)





(f)



(g)

Fig. 6. 17. The comparison of prediction and experimental results, for different voltages applied only at the central electrode

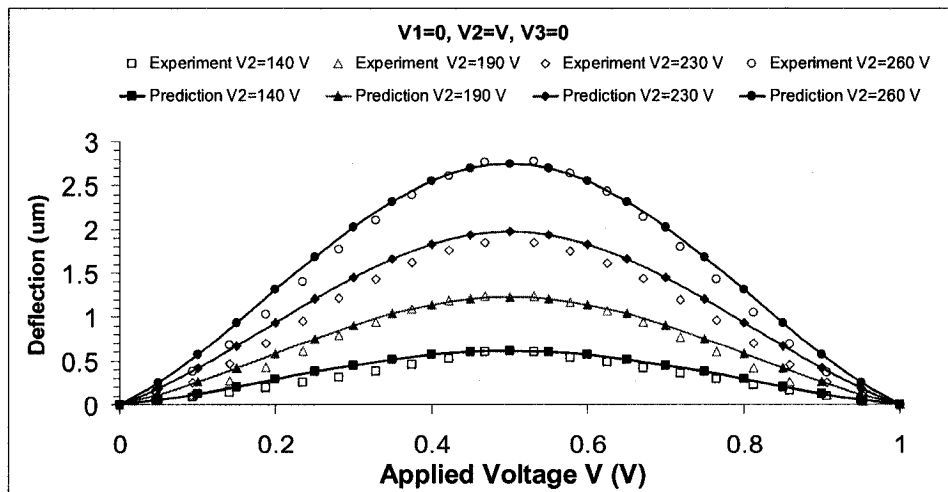


Fig. 6. 18. The static deflections of experimental results and prediction under different voltages applied only at the central electrode

6.4.2 Case 2: Same Voltage Applied on Two-Side Electrostatic Actuators

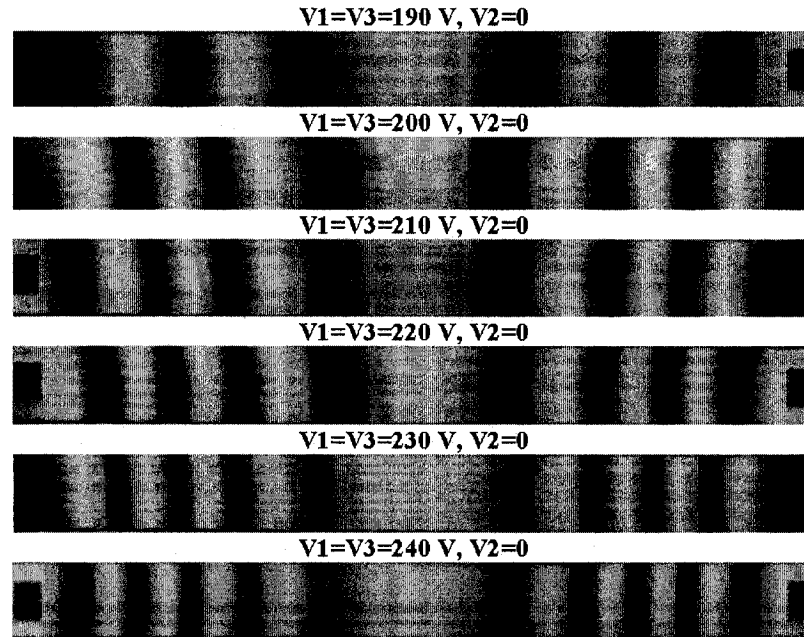


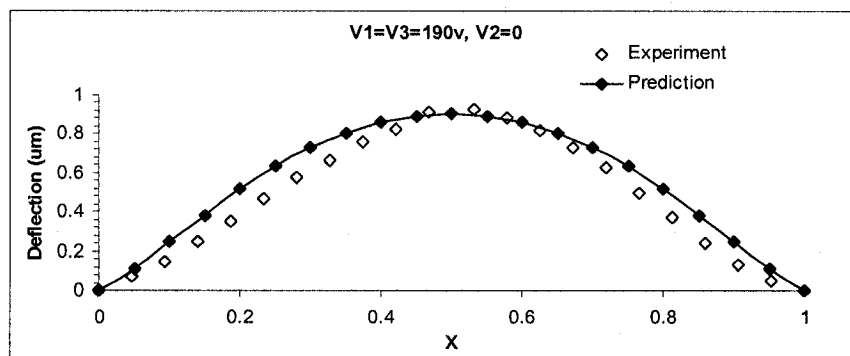
Fig. 6. 19. The fringe patterns of the microbridge for different applied voltages on two side electrodes

Table 6. 3. Comparison of the maximum deflection between prediction and experiments when same voltage is applied only at two side electrodes

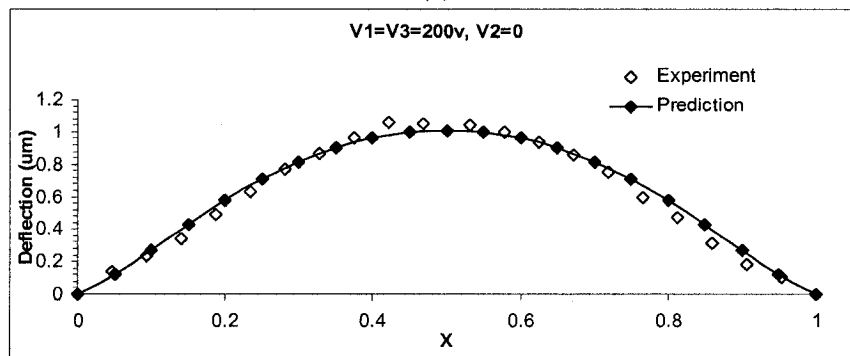
Applied Voltage (V)	The maximum deflection (μm), with $K_r^* = 15$					
	240 V	230 V	220 V	210 V	200 V	190 V
Proposed method	1.518	1.378	1.247	1.125	1.011	0.904
Experiment	1.550	1.531	1.237	1.230	1.060	0.926
Error (%)	2.10	11.07	0.87	9.31	4.84	2.45

In Case 2, same voltage is applied at the two-side electrostatic actuators. Although the maximum deflection is still located at the center of microbridge, the shapes of the deflections are quite different from the first case. From the fringe pattern as shown in the Fig. 6. 19, the fringe stripes can be clearly found with a sharp contrast on two sides but blurred at the center of the microbridge. The reason is that electrostatic forces are mainly

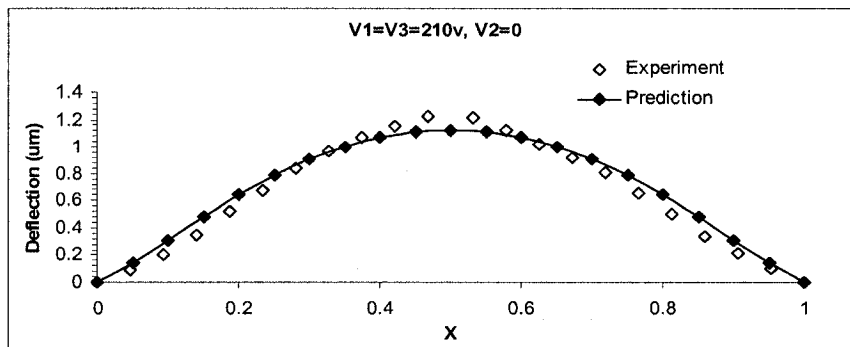
working on two-side of the microstructure which causes uneven deformation, higher tilt on two sides and less sloped surface in the middle of the microbridge as shown in Fig. 6. 20(a)~(f). Since the clear fringe patterns of the middle part of the microbridge cannot be achieved, it is difficult to accurately evaluate the maximum deflections from the images. The big errors can be found in the comparison of the experimental results and theoretical prediction in the Table 6.3.



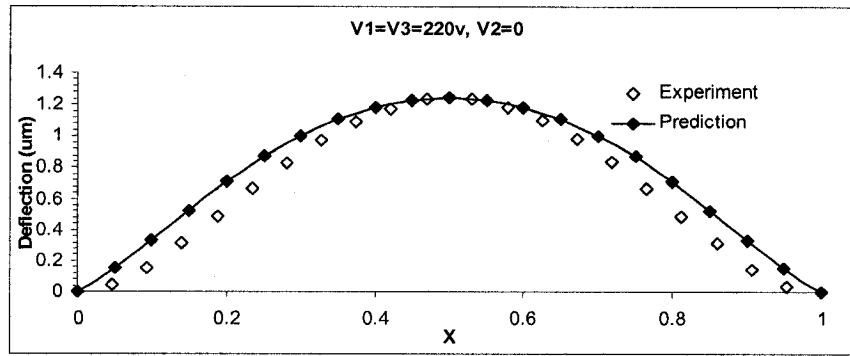
(a)



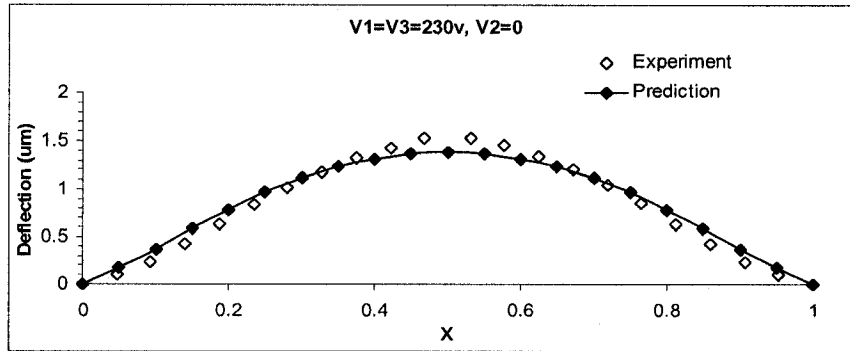
(b)



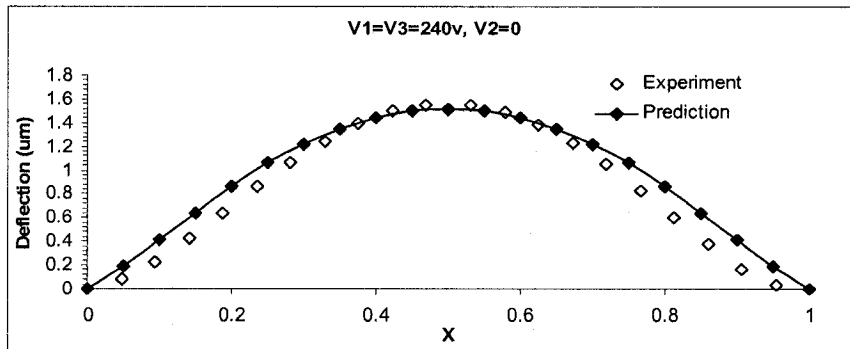
(c)



(d)



(e)



(f)

Fig. 6. 20. The comparison of prediction and experimental results when different voltages applied at two side electrodes

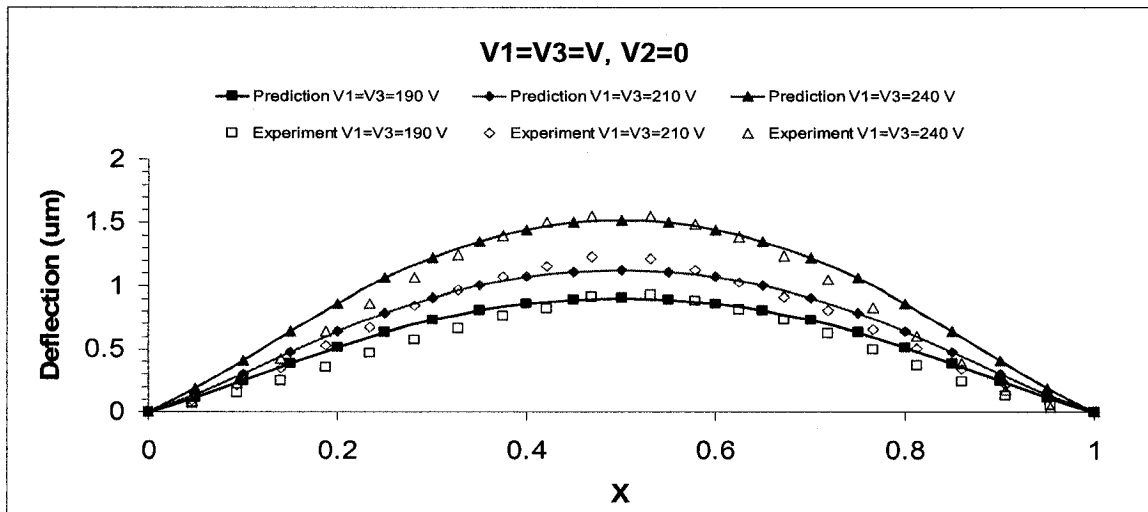


Fig. 6. 21. The static deflections of experimental results and prediction under different voltages applied at two side electrodes

6.4.3 Case 3: Same Voltage Applied at all Three Electrostatic Actuators

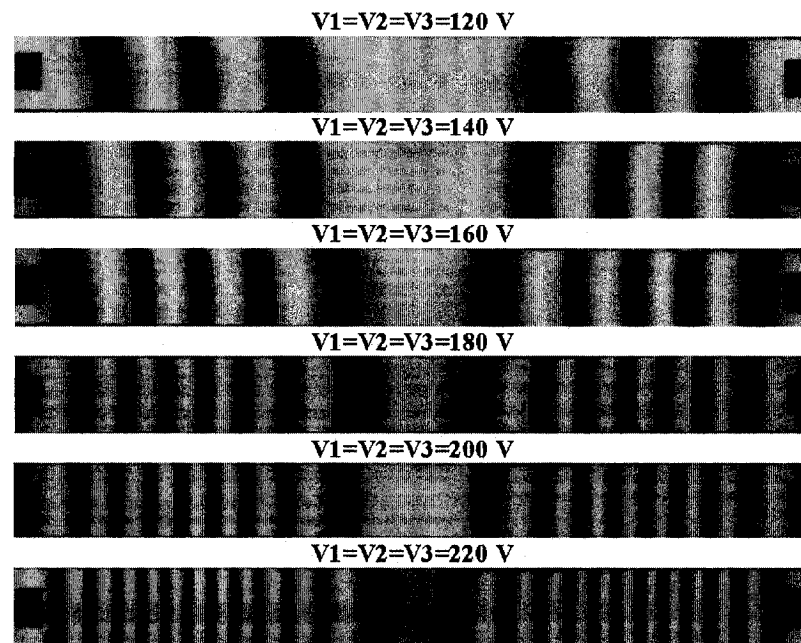


Fig. 6. 22. The fringe patterns of the microbridge for different applied voltages on three electrodes together

In this case, the efficient area for electrostatic forces is on the whole bridge, not just in the part of it as in the last two cases. The same applied voltage will cause bigger

deflection amplitude. Compared with last two cases, more fringe stripes will present in the patterns under the same applied voltage as shown in Fig. 6. 22. The even distribution of electrical field will cause the even deflection shape of the microbridge. The comparison of the maximum deflections is shown in Fig. 6. 23, experimental results closely spread on the two sides of the theoretical results. The boundary status also matched well from the results shown in the Fig. 6. 24(a) ~ (g). After compared some static deflections of Fig. 6. 24, experimental results and theoretical prediction under different applied voltages are lively shown in Fig. 6. 25.

Table 6. 4. Comparison of the maximum deflection between prediction and experiments when same voltage is applied at three electrodes at the same time

The maximum deflection (μm), with $K_r^* = 15$							
Applied Voltage (V)	220 V	200 V	180 V	160 V	140 V	120 V	100 V
Proposed method	3.621	2.778	2.114	1.584	1.160	0.821	0.553
Experiment	3.713	2.753	2.256	1.542	1.233	0.914	0.614
Error (%)	2.55	0.90	6.76	2.63	6.30	11.28	11.01

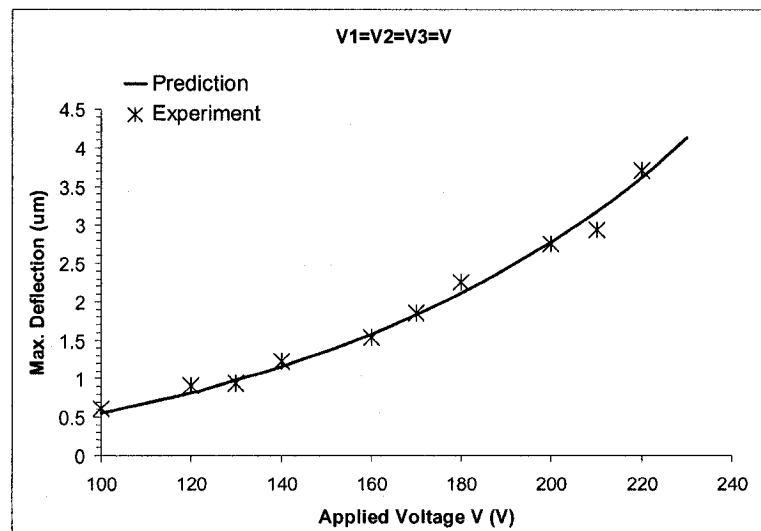
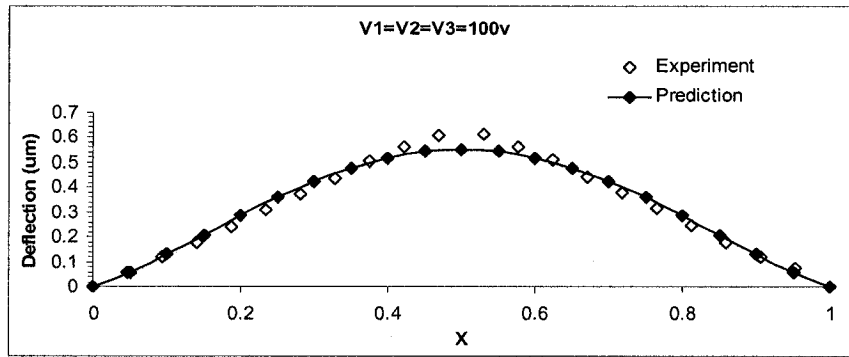
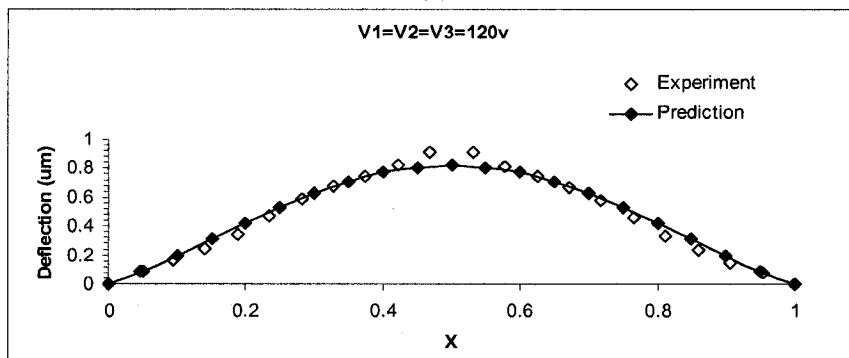


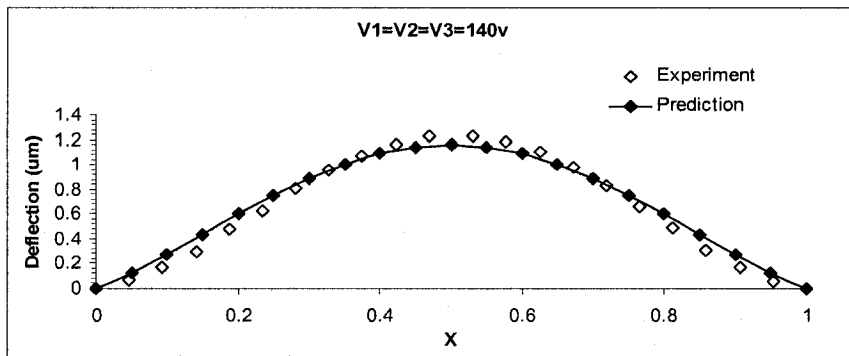
Fig. 6. 23. Comparison between the experimental and theoretical results when same voltage is applied at three bottom electrodes together



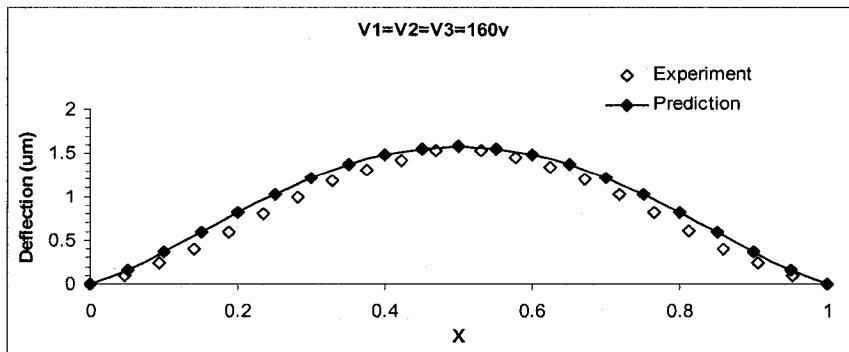
(a)



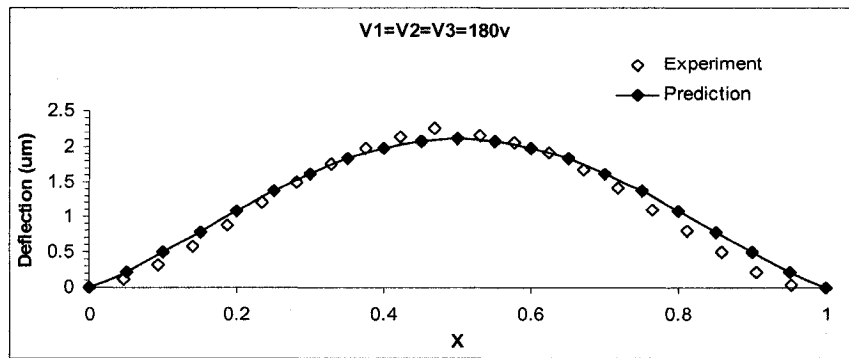
(b)



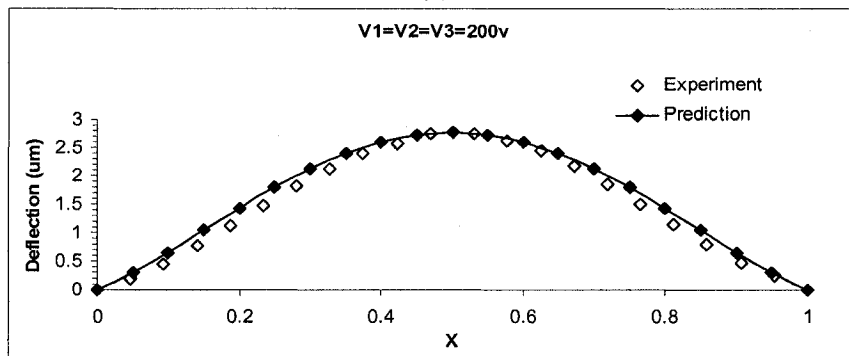
(c)



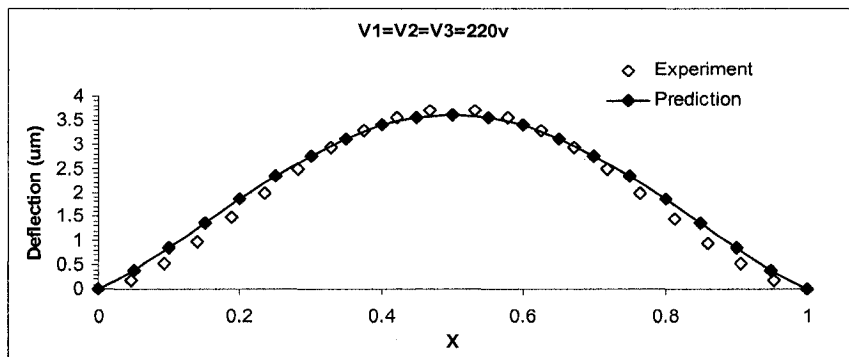
(d)



(e)



(f)



(g)

Fig. 6. 24. The comparison of prediction and experimental results, different voltages applied at three electrodes together

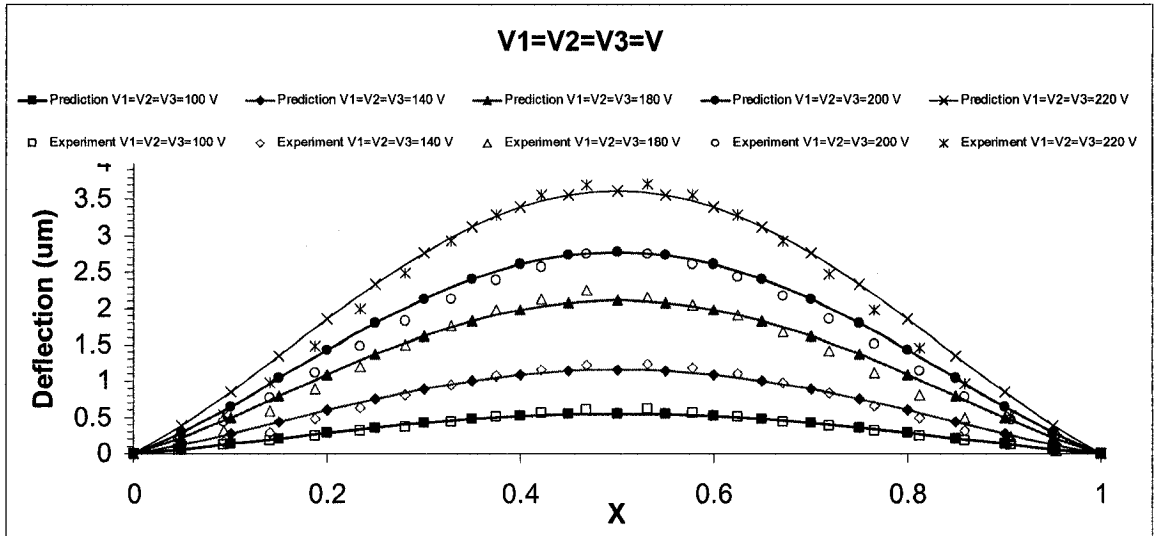


Fig. 6. 25. The static deflections of experimental results and prediction under different voltages applied at all electrodes

6.5 Summary

In this chapter, microscopic interferometry has been used for the static deflection measurement of the microbridge. This method has some advantages. First of all, it is a non-contact method which avoids damaging the microstructures. Secondly, Mirau objective obviates the need for precision alignment, which is difficult and tedious in experiments. User defined band-pass filter in FT method would help greatly reducing noise and background variation. This technique needs only one interferogram and offers great abilities for eliminating undesirable disturbances especially in noisy interference pattern evaluation. However, phase ambiguity and common accuracy compared with phase shifting method are limitations for FT method.

According to some of the experimental results, the rotational stiffness K_r can be quickly estimated. The comparison of maximum static deflection against the applied voltage

between the experimental results and the theoretical predictions validate the present method with close agreement. The percentage of accuracy of the prediction for these three selected cases was also presented. It is found out that the theoretical predictions are in close agreement with the experimental results for all the cases. Thus, the proposed method is validated for microstructures with multiple electrostatic actuators through experiment. This validation provides enormous confidence for further design and applications.

Chapter 7

7 CONCLUSIONS AND RECOMMENDS FOR FUTURE WORK

7.1 Conclusions

Micro beams and plates are typical elements of MEMS devices which can find various applications, such as sensors, actuators, wave guides and switches. In this thesis, a simplified method was proposed to model MEMS microbridges and microplates which are actuated with multiple electrodes. The influence of electrostatic actuators' locations and boundary conditions of the suspended microstructures on the static deflection and the frequency responses has been investigated. The applied voltage for electrodes was optimized through influence functions in order to achieve the desired deflections. Reduced Order Modeling (ROM) method was chosen for preliminary comparison with the theoretical model. Experimental technique based on Microscopic interferometry was designed, developed and installed in order to further verify the proposed theory.

Normally, the electrostatic actuator was modeled as a pair of parallel plates in previous investigations. For a multiple-electrode device, linear combination the effect of each of electrostatic actuators was used to model the whole microstructure. Non-classical boundary conditions of the microstructure resulted from various microfabrication processes were modeled by translational and rotational artificial spring stiffnesses. Boundary characteristic orthogonal polynomials were used in the proposed method to approximately predict the static and dynamic behaviors of the microstructures based on a given set of system parameters. The effects of location of the electrostatic actuators, applied voltage and various boundary conditions were considered in this thesis. The

advantage of the microdevice with multiple electrostatic actuators was very obvious. Not only could the irregular deflections be achieved, the natural frequencies could also be steered in certain region.

Influence functions for each of the electrostatic actuators were built up by the energy method. By this, any desired deflection was represented by simple linear combination of influence functions, which could be obtained individually. The residual errors were minimized by Least-Square Fitting method. The optimized applied voltage for each electrostatic actuator could also be obtained for desired shaped required.

Coupled-field FEA analysis was carried out in ANSYS simulation. The background simulation theory, Reduced Order Modeling (ROM) method was briefly introduced. This simplified method greatly reduced the size and complexity of the 2D and 3D models. It did help greatly reduce computational time. However, fine mesh was highly recommended to enhance accuracy and only the first few dominant response frequencies could achieved in simulation. A non-contact method, based on Microscopic interferometry was developed to further verify the prediction models. Mirau objective greatly benefited the user in obviating the need for tedious alignment of optical devices. What's more, Fourier Transformation (FT) method offered a convenient way to handle the experimental data.

The main purpose of this thesis was to develop simplified methods to analyze the electromechanically coupled problem in MEMS devices and to verify them through experimentation. There is no doubt that these simple methods do offer an elegant way for

these problems but the limitations are also coexistent. Based on the work done in this thesis, the following conclusions have been drawn.

- The electrostatic forces always pull down the suspending microstructures towards the fixed electrodes. Therefore, it is possible to determine the locations of the electrostatic actuators and optimize the applied voltage for each of them that can make deflect the microstructure to the required shape.
- The dynamic characteristics of a microstructure will be altered by the electrostatic forces. The microstructure will become unstable when the applied voltage over a certain value, called pull-in voltage. Besides the gap between electrodes, geometry of the microstructure, material properties and boundary conditions influence the performance of the electrostatic actuators. Thus, the dynamic responses of a microdevice can be freely controlled in a certain region by combining the influence of the electrodes.
- The proposed method was developed based on small deflection assumption. For the case of a deformable microstructure working under multiple electrostatic actuators, energy based method offers a very simple, efficient and accurate way of calculating deflection shapes, generating influence functions to optimize the applied voltage and predict dynamic response. This method can be efficiently used up to $2/3$ of the pull-in condition.
- Least-Square Fitting method was used to minimize the residual error between desired deflection and optimized deflection. This method allows the freedom to choose the desired deflection, either as a function or a set of sample points. The exact deflection of the whole structure need not to be known previously.

- ROM method is another simple and efficient way to solve mechanical and electrostatic coupling problems. However, it is difficult to produce sophisticated deflection shapes, generate high order natural frequencies and nonhomogeneous boundary conditions compared with the proposed method.
- Mirau microscopic interferometry is such a versatile measurement tool that can be used to measure surface height, deformation, static and dynamic characteristics of microdevices. The experimental setup is relatively easy to be built and accurate results can be achieved with this method.
- After many comparisons among prediction method, ANSYS simulation and experimentation, it is safe to draw a conclusion that the combining orthogonal polynomials into the proposed method can efficiently predict the static deflections and dynamic responses of any problems with nonhomogeneous boundary conditions and multiple electrostatic actuators.

7.2 Recommendation for Future Work

The field of MEMS has been extensively studied over the last decade and electrostatic actuation already became a major branch in MEMS industry in recent years. The discoveries of novel materials, manufacturing processes, physical phenomena in micro- or nano-scale and theoretical techniques always provide new opportunities for MEMS developments.

The irregular deflection shapes of the microstructures will lead to many new potential applications for these microstructures with multiple electrostatic actuators, such as AO deformable mirror, waveguides, OXC etc. The present modeling can also be modified

and used for RF filter, capacitive pressure sensors, optical/electrical switch and others. Although some experiments are included, most of the effort was concentrated on modeling analysis in the present work. The following points are proposed to be considered for further study and developments in the future.

- The approximated technique in modeling causes discrepancies in pull-in prediction. Nonlinear methods are suggested for improving accuracy in that unstable condition.
- The boundary condition stiffness, K_r value should be accurately measured by dynamic behavior testing. The dynamic responses of the microstructures under different electrostatic actuators can also be studied.
- Regular/ Irregular geometry shapes and boundaries of the microstructures and the shape of the bottom electrodes and their locations can all be modeled by extending the current method.
- Other external effects, such as squeeze film damping and thermo-mechanical properties can also be further considered in the model.

REFERENCE

1. [Attia P et al., 1998] Attia P, Bontry M, Bossehoeuf A, Hesto P (1998) Fabrication and characterization of electrostatically driven silicon microbeams. *Microelectronics* 29: 641-644.
2. [Babcock H W, 1953] Babcock H W (1953) The possibility of compensating astronomical seeing. *Publ. Astron. Soc. Pac.* 65: 229.
3. [Bardeen J and Brattain W H, 1948] Bardeen J and Brattain W H (1948) The transistors, a semiconductor triode. *Phys. Rev.* 74: 230.
4. [Bauer P and Van Duijsen P J, 2005] Bauer P and Van Duijsen P J (2005) Challenges and Advances in Simulation. *IEEE 36th Conference on Power Electronics Specialists*: 1030-1036.
5. [Bazley N W et al., 1965] Bazley N W, Fox D W and Stadter J T (1965) Upper and lower bounds for frequencies of rectangular cantilever plates. *Tech. Memo. TG-705, Appl. Phys. Lab., Johns Hopkins University.*
6. [Bhat R B, 1985] Bhat R B (1985) Natural frequencies of rectangular plates using characteristic orthogonal polynomials in Rayleigh-Ritz method. *Sound and Vibration* 102(4): 493-499.
7. [Bhushan B et al., 1985] Bhushan B, Wyant J C and Koliopoulos C (1985) Measurement of surface topography of magnetic tapes by Mirau interferometry. *Optical Society of America* 24(10): 1489-1497.
8. [Bifano T et al., 2002] Bifano T, Perreault J, Bierden P, Dimas C (2002) Micromachined deformable mirrors for adaptive optics. *Proc. of SPIE* 4285: 10-13.
9. [Bradley J K et al., 2005] Bradley J K, Walied A M, David M C (2005) Finite element modeling of capacitive micromachined ultrasonic transducers. *Ansys Solutions*: 16-19.
10. [Chatzandroulis S et al., 2006] Chatzandroulis S, Koliopoulou S, Goustouridis D, Tsoukalas D (2006) Capacitive pressure sensors and switches fabricated using strain compensated SiGeB. *Microelectronic Engineering*, 83(4-9) *SPEC. ISS.*: 1209-1211.

11. [Choi B and Lovell E G, 1997] Choi B and Lovell E G (1997) Improved analysis of microbeams under mechanical electrostatic loads. *Micromechanics and Microengineering* 7: 24-29.
12. [Chu P B et al., 1996] Chu P B, Nelson P R, Tachiki M L, Pister K S (1996) Dynamics of polysilicon parallel-plate electrostatic actuators. *Sensors and Actuators A*, 52:216-220.
13. [Chui et al., 1998] Chui B, Kenny T, Mamin H, Terris B and Rugar D (1998) Independent detection of vertical and lateral forces with a sidewall-implanted dual-axis piezoresistive cantilever. *Appl. Phys. Lett.* 72(11):1388-1390.
14. [Chu P B et al., 2004] Chu P B, Brener I, Chuan P u, Lee S S, Dadap J I, Sangtae P, Bergman K, Bonadeo N H, Chau T, Chou M, Doran R A, Gibson R, Harel R, Johnson J J, Lee C D, Peale D R, Tang B, Tong D T K, Tsai M J, Wu Q, Zhong W, Goldstein E L, Lin L Y, Walker J A (2004) Design and nonlinear servo control of MEMS mirrors and their performance in a large port-count optical switch. *Microelectromechanical Systems* 14(2): 261-273.
15. [CIR, 2003] Communications Industry Researchers, Inc. (CIR) *Emerging Opportunities in Optical MEMS: 2003-2007.*
16. [Claassen R W and Thorne C J, 1960] Claassen R W and Thorne C J (1960) Transverse vibrations of thin rectangular isotropic plates. *Notes Tech. Pub. 2379, Navweps Rept. 7016 U.S. Naval Ordnance Test Sta., China Lake, Calif.*, (Errata available from CFSTI as AD 245 000.)
17. [Claassen R W and Thorne C J, 1962] Claassen R W and Thorne C J (1962) Vibrations of a rectangular cantilever plate. *Tech. Pept. PMR-TR-61-1, Pacific Missile Range.*
18. [Claassen R W and Thorne C J, 1962] Claassen R W and Thorne C J (1962) Vibrations of a rectangular cantilever plate. *Aerospace Sci.* 29 (11): 1300-1305.
19. [Claflin E S and Bareket N, 1986] Claflin E S and Bareket N (1986) Configuring an electrostatic membrane mirror by least squares fitting with analytically derived influence functions. *Optical Society of America* 3(11): 1833-1839.
20. [CMC/SCM, 2005] Introduction to Micragem: A silicon-on-insulator based micromachining process report ICI-138 V4.0 Micralyne.

21. [Dickinson S M and Li E K H, 1982] Dickinson S M and Li E K H (1982) On the use of simply-supported plate functions in the Rayleigh-Rize method applied to the flexural vibration of rectangular plates. *Sound and Vibration* 80: 292-297.
22. [Doble N and Williams D R, 2004] Doble N and Williams D R (2004) The application of MEMS technology for adaptive optics in vision science. *Selected Topics in Quantum Electronics*, IEEE 10(3): 629-635.
23. [Douglass M R, 2003] Douglass M R (2003) DMD reliability: a MEMS success story. *SPIE Proceeding 4980, Testing, and Characterization of MEMS/MOEMS II*: 1-11.
24. [Dwight E G] Dwight E G (1982) *American Institute of Physics Handbook 3rd Ed.* McGraw-Hill: New York.
25. [Fletcher H J et al., 1956] Fletcher H J, Woodfield N and Larsen K (1956) Natural frequencies of plates with opposite edges supported. Contract DA-04-495-ORD-560, (CFSTI No. AD 107 224), Brigham Young University.
26. [Gabbay L D et al., 2000] Gabbay L D, Mehner J E, Senturia S D (2000) Computer-aided generation of nonlinear reduced-order dynamic macromodels I: non-stress-stiffened case. *Microelectromechanical Systems* 9(2):262-269.
27. [Gabbay L D et al., 2000] Gabbay L D, Mehner J E, Senturia S D (2000) Computer-aided generation of nonlinear reduced-order dynamic macromodels II: stress-stiffened case. *Microelectromechanical Systems* 9(2):270-278.
28. [Giles C R et al., 1999] Giles C R, Aksyuk V, Barber B, Ruel R, Stulz L, Bishop D (1999) Silicon MEMS optical switch attenuator and its use in lightwave subsystems. *IEEE Journal on Selected Topics in Quantum Electronics* 5(1): 18-25.
29. [Gleb V and Lina S, 1994] Gleb V and Lina S (1994) Flexible reflecting membranes micromachined in silicon. *Semiconductor Science and Technology* 9(8): 570-1572.
30. [Goldsmith C et al., 1996] Goldsmith C, Randall J, Eshelman S, Lin T H, Denniston D, Chen S, Norvell B (1996) Characteristics of micromachined switches at microwave frequencies. *IEEE MTT-S Digest*: 1141-1144.

31. [Gorecki C, 1992] Gorecki C (1992) Interferogram analysis using a Fourier transform method for automatic 3D surface measurement. *Pure Appl. Opt.* 1: 103-110.
32. [Grosso R P and Yellin M, 1967] Grosso R P and Yellin M (1967) The membrane mirror as an adaptive optical element. *Opt. Soc. Am.* 67: 399-406.
33. [Hansen S I, 1999] Hansen S I (1999) The industrial microsystem foundry-the pathway to commercialisation of MEMS. *Proceedings '99. 17th NORCHIP Conference, Oslo, Norway*: 365-70.
34. [Hariharan P, 1985] Hariharan P (1985) *Optical interferometry*. Sydney: Academic
35. [Helvajian H, 1999] *Microengineering aerospace systems*. Henry Helvajian, editor, Aerospace Press ISBN 1-884989-03-9
36. [Hornbeck L J, 1995] Hornbeck L J (1995) *Digital light processing and MEMS: Timely convergence for a bright future*. Texas Instruments Inc., Dallas, Texas.
37. [Hsu T R, 2002] Hsu T R (2002) *MEMS & Microsystem Design and Manufacture* McGraw Hill, Boston ISBN: 0072393912
38. [Hu Y C et al., 2004] Hu Y C, Chang C M, Huang S C (2004) Some design considerations on the electrostatically actuated microstructures. *Sensors and Actuators A112*: 155-161.
39. [Huang J M et al., 2003] Huang J M, Liu A, Lu C, Ahn J (2003) Mechanical characterization of micromachined capacitive switches: design consideration and experimental verification. *Sensors and Actuators A*.
40. [Ijntema D J and Tilmans H A C, 1992] Ijntema D J and Tilmans H A C (1992) Static and dynamic aspects of an air-gap capacitor. *Sensors and Actuators A: Physical*.
41. [In-Stat research, 2003] In-Stat research (2003) *Optical MEMS finding greater opportunities in non-telecom products*. *Optical MEMS: Light Speed Ahead*, IN030882EA.
42. [Jankovic V, 1964] Jankovic V (1964) The solution of the frequency equation of plates using digital computers. *Stavebnicky Casopies (In Czech)* 12 (6): 360-365.

43. [Jensen B D et al., 1999] Jensen B D, Bitsie F and de Boer M 1999 Interferometric measurement for improved understanding of boundary effects in micromachined beams. *Proceedings of the SPIE* 3875 pp. 61-72.
44. [Jensen B D et al., 1999] Jensen B D, de Boer M and Miller S L 1999 Interferometric for material property measurement in MEMS. 1999 International Conference on Modeling and Simulation of Microsystems, San Juan, Puerto Rico pp. 206-209.
45. [Juneau T N, 1997] Juneau T N (1997). *Micromachined Dual Input Axis Rate Gyroscope*. PhD thesis, U.C. Berkeley.
46. [Kamisuki S et al., 2000] Kamisuki S, Fujii M, Takekoshi T, Tezuka C, Atobe M (2000) A high resolution, electrostatically-driven commercial inkjet head. *Proceedings IEEE Thirteenth Annual International Conference on Micro Electro Mechanical Systems 2000*: 793-8.
47. [Kim S et al., 2004] Kim S, Barbastathis G, Tuller H L (2004) MEMS for optical functionality. *Electroceramics* 12: 133-144.
48. [Kovacs G, 1998] Kovacs G (1998) *Micromachined transducers sourcebook*. McGraw-Hill ISBN 0-07-290722-3.
49. [Kreis T, 1986] Kreis T (1986) Digital holographic interference-phase measurement using the Fourier-transform method. *J. Opt. Soc. Am.* A3:847-55.
50. [Kreis T and Juptner W P O, 1989] Kreis T and Juptner W P O (1989) Fourier-transform evaluation of interference pattern: the role of filtering in the spatial frequency domain. *Proc. SPIE*(1162): 116-25
51. [Kuehnel W, 1995] Kuehnel W (1995) Modelling of the mechanical behaviour of a differential capacitor acceleration sensor. *Sensors and Actuators A: Physical*.
52. [Kurczynski P et al., 2004] Kurczynski P, Dyson M H, Sadoulet B, Bower J E, Lai W Y C, Mansfield W M, Taylor J A (2004) Fabrication and measurement of low-stress membrane mirrors for adaptive optics. *Applied Optics* 43(18): 3573-3580.
53. [Laura P A A et al., 1977] Laura P A A, Luisoni L E, Filipich C (1977) A note on the determination of the fundamental frequency of vibration of thin, rectangular plates with edges possessing different rotational flexibility coefficients. *Sound and Vibration* 55: 327-333.

54. [Laura P A A and Gutierrez R H, 1981] Laura P A A and Gutierrez R H (1981) A note on transverse vibration of stiffened rectangular plates with edges elastically restrained against rotation. *Journal of Sound and Vibration* 78: 139-144.
55. [Lee W S et al., 2001] Lee W S, Kwon K C, Kim B K, Cho J H, Youn S K (2001) Frequency-shifting analysis of electrostatically tunable micro-mechanical actuator. *Modeling and Simulation of Microsystems* 2(1): 83-88.
56. [Leissa W, 1969] Leissa W (1969) *Vibration of plates*. NASA SP-160, National Aeronautics and Space Administration, Washington D.C.
57. [Leissa A W, 1973] Leissa A W (1973) The free vibration of rectangular plates. *Sound and Vibration* 31: 257-293.
58. [Li Y Q et al., 2006] Li YQ, Muthukumaran P, Bhat R B 2006 Shape optimization and dynamic characterization of multiple-electrostatically deformable microbridges. *J. Microsystem Technologies* (Published online).
59. [Lin LY et al., 1999] Lin L Y and Goldstein E L (1999) Lightwave micromachines for optical cross connects. 25th Eur. Conf. Optical Communication (ECOC), Nice, France, vol. I: 114–117.
60. [Mali R K, 1999] Mali R K (1999) MEMS deformable mirrors for adaptive optics. PhD thesis, Boston University.
61. [Mansell J D et al., 2000] Mansell J D, Catrysse P B, Gustafson E K, Byer R L (2000) Silicon deformable mirrors and CMOS-based wavefront sensors. *Proc. of SPIE* 4124: 15-25.
62. [Mansell J D et al., 2002] Mansell J D, Sinha S, Byer R L (2002) Deformable mirror development at Stanford University. *Proc. of SPIE* 4493: 1-12.
63. [Marques A F et al., 2005] Marques A F, Castello R C, Shkel A M (2005) Modelling the electrostatic actuation of MEMS: state of the art 2005. Reports IOC, IOC-DT-P-2005-18.
64. [MUMPs Process, 2003] Keoster D, Cowen A, Mahadevan R, Stonefield M and Hardy B. *PolyMUMPs design handbook*. Revision 1.0 MEMSCAP.
65. [Menikoff A, 1991] Menikoff A (1991) Actuator influence functions of active mirrors. *Applied Optics* 30(7): 833-838.

66. [Miller L M et al., 1993] Miller L M, Argonin M L, Bartman R K, Kaiser W J, Kenny T W, Norton R L, Vote E C (1993) Fabrication and characterization of a micromachined deformable mirror. Proc. SPIE 1945: 421–430.
67. [Muthukumaran P et al., 1999] Muthukumaran P, Stiharu I, Bhat R B (1999) Boundary conditioning technique for structural tuning. Sound and Vibration 220(5): 847-859.
68. [Muthukumaran P, 2000] Muthukumaran P (2000) Boundary conditioning concept applied to the synthesis of Microsystems using fuzzy logic. PhD thesis, Concordia University.
69. [Muthukumaran P et al., 2002] Muthukumaran P, Stiharu I, Bhat R B (2002) Boundary conditioning of capacitive MEMS devices through fabrication methods and operating environments. Proceedings of ISSS-SPIE, International Conference on Smart Materials Structures and Systems, Indian Institute of Science, Bangalore, India.
70. [Neilson D T et al., 2000] Neilson D T, Aksyuk V A, Arney S, Basavanhally N R, Bhalla K S, Bishop D J, Boie B A, Bolle C A, Gates J V, Gottlieb A M, Hickey J P, Jackman N A, Kolodner P R, Korotky S K, Mikkelsen B, Pardo F, Raybon G, Ruel R, Scotti R E, van Blarcum T W, Zhang L, Giles C R (2000) Fully provisioned 112×112 micro-mechanical opticalcrossconnect with 35.8 Tb/s demonstrated capacity. Optical Fiber Communication Conference 2000, Baltimore, MD, USA, 4: 202-204.
71. [Nishiyama H and Nakamura M, 1990] Nishiyama H and Nakamura M (1990) Capacitance of a strip capacitor. IEEE Transactions on Components, Hybrids and Manufacturing Technology 13(2): 417-423.
72. [Nishiyama H and Nakamura M, 1993] Nishiyama H and Nakamura M (1993) Capacitance of disk capacitors. IEEE Transactions on Components, Hybrids and Manufacturing Technology 16(3): 360-366.
73. [Nishiyama H and Nakamura M, 1994] Nishiyama H and Nakamura M (1994) Form and capacitance of parallel-plate capacitors. IEEE Transactions on Components, Hybrids and Manufacturing Technology A17 (3): 477-484.

74. [Pamidighantam S et al. 2002] Pamidighantam S, Puers R, Baert K and Tilmans H A C (2002) Pull-in voltage analysis of electrostatically actuated beam structures with fixed-fixed and fixed-free end conditions. *Micromechanics and Microengineering* 12: 458-464.
75. [Quan C et al., 2003] Quan c, Wang S H, Tay C J, Liu A Q and Shang H M (2003) Deformation evaluation of a micro-RF capacitive switch membrane using laser interferometry. *Opt. Eng.* 42: 92–97.
76. [Restaino S R et al., 2005] Restaino S R, Gilbreath, G C, Payne D M, Andrews J R (2005) Experimental results of a MEMS-based adaptive optics system. *Journal of Microlithography, Microfabrication and Microsystems* 4(4): 041504.
77. [Rinaldi G et al., 2004] Rinaldi G, Muthukumaran P, Stiharu I (2004) Electrostatic boundary conditioning of MEMS devices. 8th Cairo University International Conference on Mechanical Design and Production, Cairo- Egypt.
78. [Rochus V et al., 2006] Rochus V, Rixen D J, Golinval J C (2006) Monolithic modelling of electro-mechanical coupling in micro-structures. *Numerical Methods in Engineering* 65: 461-493.
79. [Satoshi I et al., 2003] Satoshi I, Kazuyuki M, Tamotsu A, Yoshio S, Tetsuji Y, Yuji I, Osamu T, Masaaki K (2003) High-speed 80×80 MEMS optical switch module with VOA. Invited Paper for ECOC-IOOC 2003, Rimini, Italy.
80. [Senturia S D, 2000] Senturia S D (2000) *Microsystem Design*. Boston, Kulwer Academic Publishers: ISBN: 0-7923-7246-8.
81. [Shockley W et al., 1948] Shockley W, Bardeen J, Brattain W H (1948) Electronic theory of the transistor. *Science* 108, 678–679.
82. [Sigi Lito V G, 1965] Sigi Lito V G (1965) Improved upper bounds for frequencies of rectangular free and cantilever plates. *Eng. Memo. EM-705*, Appl. Phys. Lab., Johns Hopkins University.
83. [Takeda M et al., 1982] Takeda M, Ina H and Kobayashi S (1982) Fourier-transform method of fringe-pattern analysis for computer-based topography and interferometry. *J. Opt. Soc. Am.* 72: 156-160.
84. [Teymoori and Abbaspour-Sani, 2002] Teymoori, M. and Abbaspour-Sani, E. (2002). A novel electrostatic micromachined pump for drug delivery systems. In

- Semiconductor Electronics, 2002. Proceedings. ICSE 2002. IEEE International Conference on.
85. [Thomsen J J, 2003] Thomsen J J (2003) Vibrations and stability, advanced theory, analysis, and tools. 2nd Edition, Springer, ISBN 3-540-40140-7.
 86. [Thomson W T and Dahleh M D, 2003] Thomson W T and Dahleh M D (2003) Theory of vibration with applications. 5th Edition, Pearson Education, ISBN 81-297-0209-6.
 87. [Thompson Charles A et al., 2003] Thompson Charles A, Wilks Scott C, Brase James M, Young Richard A, Johnson Gary W, Ruggiero Anthony J (2002) Horizontal path laser communications employing MEMS adaptive optics correction. Proceedings of SPIE - The International Society for Optical Engineering 4494: 89-95.
 88. [Tilmans H A C and Legtenberg R, 1994] Tilmans H A C and Legtenberg R (1994) Electrostatically driven vacuum-encapsulated polysilicon resonators: part II. theory and performance. Sensor and actuators A: Physical 45: 67-84.
 89. [Timoshenko S P and Krieger W, 1959] Timoshenko S P and Krieger W (1959) Theory of plates and shells. 2nd Edition, Engineering Societies Monographs.
 90. [Ting-Kuang C et al., 1996] Ting-Kuang C, Nobuyuki K, Michel E M, Leonid G K (1996) Cross-phase modulation in fiber links with multiple optical amplifiers and dispersion compensators. Journal of Lightwave Technology 14(3): 249-260.
 91. [Tolansky S, 1996] Tolansky S (1996) An Introduction to Interferometry. William Clowes and Sons Ltd., London.
 92. [Tortonese M et al., 1993] Tortonese M, Barrett R, and Quate C (1993) Atomic resolution with an atomic force microscope using piezoresistive detection. Appl. Phys. Lett. 62:8340-8363.
 93. [Tyson R K, 1998] Tyson R K (1998) Principles of adaptive optics. 2nd Edition, Academic Press, ISBN 0-12-705902-4.
 94. [Vdovin G and Sarro P M, 1995] Vdovin G and Sarro P M (1995) Flexible mirror micromachined in silicon. Applied Optics 34(16): 2968-2972.

95. [Vdovin G et al., 1997] Vdovin G, Middelhoek S, Sarro P M (1997) Technology and applications of micromachined silicon adaptive mirrors. *Optical Engineering* 36:1382-1390.
96. [Walker J A, 2001] Walker J A (2001) MEMS Technology in optical layer networks. Invited Paper for 51st ECTC, Orlando, Florida.
97. [Wang J Y and Silva D E, 1980] Wang J Y and Silva D E (1980) Wave-front correction and production of Zernike. *Applied Optics* 19(9): 1510-1518.
98. [Wang P K C and Hadaegh F Y, 1996] Wang P K C and Hadaegh F Y (1996) Computation of static shapes and voltages for micromachined deformable mirrors with nonlinear electrostatic actuators. *IEEE, Microelectromechanical Systems* 5(3): 205-220.
99. [Wang S H et al., 2000] Wang S H, Tay C J, Quan C and Shang H M (2000) Evaluation of micro-beam deflection using interferometry. *Proc. SPIE* 4317: 262–267.
100. [Wang S H and Tay C J, 2006] Wang S H and Tay C J (2006) Application of an optical interferometer for measuring the surface contour of micro-components. *Meas. Sci. Technol* 17: 617-625.
101. [Wong A C et al., 1998] Wong A C, Ding H, Nguyen C T C (1998) Micromechanical mixer+filters. *Technical Digest, IEEE International Electron Devices Meeting, San Francisco, California*: 471-474.
102. [Wyant J C et al., 1984] Wyant J C, Koliopoulos C L, Bhushan B, and George O E (1984) An optical profilometer for surface characterization of magnetic media. *ASLE Trans.* 27, 101.
103. [Wu M C, 1995] Wu M C; Lin L Y, Lee S S, Pister K S J (1995) Micromachined free-space integrated micro-optics. *Sensors and Actuators, A: Physical* 50(1-2): 127-134.
104. [Yang W et al., 1996] Yang W, Jia Y, Jing T, Shi W, Hou S, Wang C, Xiang Y, Fan J, Lu P, Ma S, Xu C (1996) The research on the waveguide lens and grating integrated optical wavelength-division-multiplexing device. *Proceedings of the SPIE, International Society for Optical Engineering* 2891: 229-233.

- 105.[Yuhua Z et al., 2006] Yuhua Z, Siddharth P and Austin R (2006) Adaptive optics scanning laser ophthalmoscope using a microelectro- mechanical (MEMS) deformable mirror. Progress in Biomedical Optics and Imaging - Proceedings of SPIE 6138, Ophthalmic Technologies XVI: 61380Z.
- 106.[Zhou T and Robinson A M, 2002] Zhou T and Robinson A M (2002) Tunable CMOS MEMS electromechanical bandpass filters. Canadian Journal of Electrical and Computer Engineering 27(1): 17-21.
- 107.[Zhu L J et al., 1999] Zhu L J, Sun P C, Bartsch D U, Freeman W R, Fainman Y (1999) Adaptive control of a micromachined continuous-membrane deformable mirror for aberration compensation. Applied Optics 38(1): 168-176.
- 108.[Zhu L J et al., 1999] Zhu L J, Sun P C, Fainman Y (1999) Aberration-free dynamic focusing with a multichannel micromachined membrane deformable mirror. Applied Optics 38(25): 5350-5354.